

The University of Nottingham

UNITED KINGDOM · CHINA · MALAYSIA

Irradiation induced reactions in carbon nanomaterials in transmission electron microscopy

Stephen T. Skowron, MSci

Thesis submitted to the University of Nottingham
for the degree of Doctor of Philosophy

March 2016

Abstract

Aberration corrected transmission electron microscopy is a powerful tool for the structural characterisation of materials at the atomic scale, but the passage of high velocity electrons through the material can often induce structural changes *via* the transfer of large amounts of energy from the beam. The work in this thesis theoretically considers the nature of this transfer of energy and its impact upon the material being studied.

The computational modelling of molecular species encapsulated inside carbon nanotubes and their response to electron irradiation is compared to results from TEM experiments, and used to explain the experimental observations. The high rate of destruction of C-H bonds under the beam is quantified, and its implications for TEM studies of organic materials considered. An effective solution for mitigating this rate of destruction is found, applied to a model system, and then confirmed experimentally. Using the considerations of stability under the beam, two experimentally witnessed reactions are investigated in detail, and careful comparison to intermediate structures observed in TEM allows full reaction mechanisms to be proposed.

The dynamic motion of atomic defects in irradiated graphene is considered with the aid of a large library of experimental TEM images. A novel defect structure is observed, and is seen to undergo structural rearrangements on a quicker time-scale than accessible to TEM imaging. This species enables the very quick migration of defect structures across the graphene lattice, and is attributed to a trivacancy structure.

The rates of beam induced reactions are considered in the framework of chemical kinetics, and a method for extracting kinetic parameters of a reaction from the statistics of a large number of TEM observations of it occurring is developed. This is used to obtain the first cross-sections for the formation and healing of the irradiation induced Stone-Wales bond rotation, and the first experimental activation energy for its healing. The latter agrees well with a theoretically predicted mechanism of catalysis, while the former demonstrates that the widely assumed process of direct knock-on damage cannot be responsible for the beam induced reaction. An alternative mechanism is proposed, resulting from the electronic excitation of the defect.

List of publications

The following papers have been published in peer reviewed journals (or submitted for publication) in the course of the work detailed in this thesis:

- Approaches to modelling irradiation-induced processes in transmission electron microscopy. S. T. Skowron, I. Lebedeva, A. Popov and E. Bichoutskaia, *Nanoscale*, 2013, **5**, 6677-6692.

- Formation of nickel-carbon heterofullerenes under electron irradiation. A. Sinitsa, I. Lebedeva, A. Knizhnik, A. Popov, S. T. Skowron and E. Bichoutskaia, *Dalton Transactions*, 2014, **43**, 7499-7513.

- Isotope substitution extends the lifetime of organic molecules in transmission electron microscopy. T. Chamberlain, J. Biskupek, S. T. Skowron, P. Bayliss, E. Bichoutskaia, U. Kaiser and A. N. Khlobystov, *Small*, 2015, **11**, 622629.

- Energetics of atomic scale structure changes in graphene. S. T. Skowron, I. Lebedeva, A. Popov and E. Bichoutskaia, *Chemical Society Reviews*, 2015, **44**, 3143-3176.

- Reaction kinetics of bond rotations in graphene. S. T. Skowron, V. O. Koroteev, M. Baldoni, S. Lopatin, A. Zurutuza, A. Chuvilin and E. Besley, *Carbon*, 2016, **105**, 176-182.

- Filming chemical transformations at the single-molecule level by transmission electron microscopy leads to the discovery of new reactions. T. W. Chamberlain, J. Biskupek, S. T. Skowron, A. V. Markevich, S. Kurasch, O. Reimer, K. Walker, G. A. Rance, X. Feng, K. Müllen, A. Turchanin, M. A. Lebedeva, A. G. Majouga, V.G. Nenajdenko, U. Kaiser, E. Besley and A. N. Khlobystov, *Submitted*, 2016.

- Growth of single-layer boron nitride dome-shaped nanostructures catalysed by iron clusters. A. L. Torre, E. H. Åhlgren, M. W. Fay, F. B. Romdhane, S. T. Skowron, C. Parmenter, A. J. Davies, J. Jouhannaud, G. Pourroy, P. D. Brown, E. Besley, and F. Banhart, *Submitted*, 2016.

Acknowledgements

I'd like to thank the many people who have helped, guided and assisted me in the last three years. First and foremost, I am extremely grateful to my PhD supervisor Elena Besley, for her vital guidance in this work, many interesting and entertaining discussions, and perhaps above all for providing the academic freedom that made this time so enjoyable. I look forward to our further collaborations!

I must also thank everyone else in the University of Nottingham computational and theoretical chemistry groups for making it such a pleasant working environment, most notably Matteo Baldoni and Harriet Åhlgren, who performed the simulations described in Chapter 4. A special thanks also to Alexander Markevich and Jack Wadey for their collaboration in all things carbon nanoscience, as well as to the rest of the computational nanoscience group, which has grown so large over the past few years I must thank here as a group rather than individually! I am very grateful to Nick Besley, for both his supervision during my undergraduate studies and for his continued assistance. Further afield, many thanks to Andrey Popov and Irina Lebedeva for their collaborations on theoretical work.

Experimental results feature heavily in this theoretical work, and the close collaboration with microscopists is a large part of what made this work so engaging and exciting. In Nottingham, I have to thank Tom Chamberlain and Andrei Khlobystov for their experimental efforts, useful conversations, and for being willing to listen to and indulge a theoretician who knows little of the practical aspects of actually operating an electron microscope. In San Sebastian, my warmest thanks go to Andrey Chuvilin for his superb hospitality, discussions, experimental TEM images and Rioja, in equal measure. I am grateful to everyone at CIC NanoGUNE for making me feel very welcome during my visit, and to Victor Koroteev for our collaboration there (and his patience). In Ulm, Johannes Biskupek and Ute Kaiser have my gratitude; their excellent TEM images are included on many of the pages in this thesis and were key to much of the work in Chapter 3.

Finally, and most importantly, thanks to everyone on the non-academic side of life: my friends[i] and family. I am incredibly grateful for the love and support of my parents and brothers over the years, without which none of the work in this thesis would have been possible.

[i]And because I promised to, a special thanks to Robert 'Papa Rob' Kropholler for providing many years of sustenance.

For Dad. We miss you.

Contents

1 Introduction **1**
- 1.1 Effects of the electron beam . . . 4
- 1.2 Materials studied . . . 5
  - 1.2.1 Graphene . . . 6
  - 1.2.2 Carbon nanotubes and encapsulated molecules . . . 8

2 Computational and theoretical techniques **10**
- 2.1 Theory of elastic electron collisions . . . 11
  - 2.1.1 The McKinley-Feshbach approximation . . . 11
  - 2.1.2 Transferred energy . . . 14
  - 2.1.3 Isotropic approximation of the threshold energy . . . 16
  - 2.1.4 Contribution of atomic thermal motion . . . 18
  - 2.1.5 Regime of validity . . . 20
- 2.2 Computational details . . . 21
  - 2.2.1 Wavefunction-based approaches . . . 21
  - 2.2.2 Density functional theory . . . 24
- 2.3 Multislice image simulations . . . 28
  - 2.3.1 Formation of nickel-carbon heterofullerenes . . . 29
  - 2.3.2 h-BN domes . . . 29

3 Reactions of nanotube-encapsulated molecules in TEM **32**
- 3.1 Nanotube exclusion in E_d simulations . . . 33
- 3.2 Sulphur-terminated graphene nanoribbons . . . 34
  - 3.2.1 Simulations . . . 34
  - 3.2.2 Discussion . . . 36
- 3.3 Deuteration of organic species in TEM . . . 38
  - 3.3.1 Coronene . . . 39
- 3.4 Perchlorocoronene to nanoribbon transformation . . . 42
  - 3.4.1 Chlorine emission . . . 46
  - 3.4.2 C-C bond-breaking . . . 49
- 3.5 Sulflower to nanoribbon transformation . . . 51
  - 3.5.1 Initial atom emission and reaction . . . 51
  - 3.5.2 Subsequent emission and conformational changes . . . 53
  - 3.5.3 Further molecular additions . . . 55

4 Graphene defect dynamics in TEM **58**
4.1 Graphene under electron irradiation 58
4.1.1 Atom emission and recombination 59
4.1.2 Bond rotations 61
4.1.3 Fast migration 62
4.1.4 Larger vacancy structures 64
4.2 Dynamic behaviour of trivacancies in graphene 68
4.2.1 Structure 69
4.2.2 Migration 73
4.3 Reaction kinetics of Stone-Wales rearrangements 73
4.3.1 Literature review 73
4.3.2 Kinetics of reversible beam induced processes 78
4.3.3 Experimental results 81
4.3.4 Direct knock-on and thermal spikes 87
4.3.5 Inelastic collisions 92
4.3.6 Atom emission at 80 kV 92

5 Conclusions **96**

Chapter 1

Introduction

> With magic, you can turn a frog into a prince. With science, you can turn a frog into a PhD and you still have the frog you started with.
>
> *The Science of Discworld*
> *Terry Pratchett*

Over the last decade, it has been somewhat difficult to avoid hearing about graphene. The two dimensional hexagonal lattice of carbon, first isolated in 2004,[1] has so many superlative qualities it has been termed 'a solution looking for a problem': unprecedented high carrier mobility, high thermal conductivity, high mechanical strength and elasticity, and of course an extreme surface to volume ratio, thinness and low weight. Its unique properties have attracted wide research interest, notably with the 'Graphene Flagship' being awarded one billion euros of funding as one of the EU's horizon 2020 projects, and possible applications are emerging in areas such as water desalination,[2] computing[3] and medicine.[4] It has also entered the public consciousness, being widely reported in the popular press, especially in the years since its discovery won the Nobel prize for physics in 2010.

However, graphene is only the latest (and most fashionable) of a series of new low-dimensional allotropes of carbon discovered in the last 30 years. The discovery of fullerenes[5] in 1985 followed by carbon nanotubes[6] in 1991 demonstrated that carbon could form a wide array of interesting nanomaterials with novel properties. Graphene, too, was only the first in a series of 2D materials, and has since been followed by many others such as hexagonal boron nitride, transition metal dichalcogenides, and silicene, as developments in techniques for producing monolayers of layered materials have quickly progressed.[7]

Beyond the headlines and touted applications, a huge amount of work remains in order to understand the behaviour of these materials to the degree that specific properties can be targeted *via* intentional modifications.[8] The introduction of atomic-scale defects such as those studied in Chapter 4 are one promising method by which material properties can be altered. Hand-in-hand with this, however, is the requirement that we are actually able to create the desired modifications

in a controlled manner. For both of these considerations, transmission electron microscopy (TEM) is an incredibly useful tool.

Transmission electron microscopy

TEM is in many ways a natural tool for the study of low dimensional nanomaterials. The technique, which involves firing a beam of highly accelerated electrons through a material and constructing an image from the scattering of those electrons by atoms in the sample, conventionally requires very thin slices of the material being studied, which is well suited to materials in which potentially only one possible 'slice' exists! Traditionally, the interpretation of TEM images can often be difficult, as they are the result of electrons undergoing multiple scattering events as they travel through the material. In the materials examined in this work, there are typically only one to ten atoms overlapping along the axis of the electron beam, and image contrast can therefore be directly interpreted as electron density, greatly simplifying image interpretation. Recent reviews detailing the use of TEM to study graphene in particular can be found in references 9 and 10.

Classical optical microscopes have a fundamental limit to the resolution they can achieve, related to the wavelength of visible light (450 - 600 nm). While this is also the case for electron microscopy, the much smaller wavelength of electrons (0.155 Å for electrons accelerated though 80 kV) eliminate this as a concern, as the limit is smaller than a single atom. Practically speaking, the resolution limit of modern TEM is imposed by aberrations due to the electromagnetic lenses. These are analogous to those in optical lenses: spherical aberration, where electrons near the edge of the lens are focussed more tightly than those in the centre, and chromatic aberrations, where electrons with different energies are focussed onto different points (the energy spread of electrons in the beam is under 1 eV with the use of a monochromator, compared to a beam energy of tens to hundreds of keV). In the last two decades modern developments in aberration correction,[11,12] where additional lenses are added to counteract these effects, have led to huge improvements in the practical resolution limit obtainable. Atomic resolution imaging in real time and space is now available, and with the directly interpretable nature of the images produced with these materials the end result is something akin to watching a 'movie' of the dynamics of individual atoms in the material being studied.

Aberration corrected, high resolution TEM (AC-HRTEM, henceforth simply TEM) is an incredibly useful analytical tool, but passing large numbers of relativistic electrons through a material can have significant effects on it. In addition to the spatial resolution, another limit of the technique is introduced by causing damage to the sample, inducing structural rearrangements or even completely destroying it. This damage, although a nuisance when using TEM simply as a tool for material characterisation, is not inherently a limitation or something to be avoided. Given a complete enough understanding of the underlying mechanisms, it can be exploited as a strength. The particular ways in which energy is transferred from the beam to the sample can in principle be harnessed as a tool for controlled energy input, initiating reactions that would otherwise be very diffi-

cult or impossible to accomplish with traditional chemical means. Such a method would of course also provide high resolution images of the process being triggered, allowing for the *in situ* characterisation of reactants, products, and potentially intermediate structures.

Understanding the response of materials to electron irradiation is key for this technique to be viable, and the unique manner of energy transfer into the system by the beam, although a strength, means that traditional thermodynamical considerations of systems in equilibrium are of limited use. The effect of the electron beam has been likened to simulating conditions similar to a 'virtual temperature' of 3000 K in graphene.[13] This is useful in giving an idea of the amount of energy that can be deposited into the system and the kinds of processes that are possible under the beam, but does not tell the whole story.[14] This virtual temperature is very different to a normal equilibrium high temperature, exemplified by the fact that the rise in equilibrium temperature in the same conditions remains below 1 K; short spikes of huge local energy increases are followed by long periods of low temperature thermal equilibrium. In addition, the atomic-scale mechanisms of processes caused by the beam are usually very different to those made possible by heating, even in cases where the resulting overall transformation is the same.

To properly understand the energetics of irradiation induced mechanisms, even in a qualitative manner, an understanding of the dynamics of the system is typically needed, while static energetics are of limited use and can be misleading. A low formation energy, for example, does not necessarily mean that a structure will be the most commonly formed or observed,[14] or that it will even be able to form at all. The presence of possible routes induced by the beam towards a structure and the subsequent stability of that structure against the electron irradiation are instead important.[15] On a narrower level, when it comes to the irradiation stability of specific structures these often show little or no correlation with thermodynamic stability, but depend on the atomistic dynamics of the structure following a collision with an incident electron. For example, an increase in the flexibility of the impacted structure can confer substantial protection from irradiation.[16] As shown in Chapter 2.1, the threshold energy of a process (the minimum energy required to induce it) is the most important parameter when quantifying the type of irradiation damage studied in this work. Computational studies of such processes must therefore be fully dynamical (as opposed to a simple series of static energy calculations along reaction coordinates) in order to correctly predict threshold energies accounting for this kind of radiation stability.[17] This is discussed further in Chapter 2.2.

More subtly, even when considering the dynamic case, there is an important distinction between the threshold energy and the more familiar activation energy of a thermally induced process. For an atomic process that can occur *via* either thermally or irradiation induced mechanisms, the threshold energy is always larger than the activation energy, and usually considerably so (typically 10 eV larger in the reactions considered here). There are two reasons for this: the electron beam transfers energy in a specific direction, which may lead to a suboptimal reaction pathway, especially considering the collective motion of multiple atoms. More importantly, the activation energy is simply the height of the potential barrier

separating the reactant from the product. The threshold energy can be considered as the initial 'push' (supplied by the beam) required for the reactant to overcome this barrier, and so is more akin to an integration of the potential barrier over the reaction coordinate. This is important in Section 4.3, in which the contributions of simultaneous thermally and irradiation induced mechanisms of the same process (the Stone-Wales transformation in graphene) are separated by a statistical analysis of TEM images.

The remainder of this section is composed of a general consideration of the types of irradiation-induced damage caused by the electron beam (section 1.1), followed by a discussion of how the different materials studied here are affected (section 1.2). Following this is a chapter providing an overview of the computational and theoretical techniques used. The rest of the thesis is split into two chapters: one discussing work on the reactions of molecules encapsulated inside carbon nanotubes, and the other on the dynamics of defect structures in graphene. Finally, some general conclusions, comments, and overarching themes between the two areas of work are presented.

1.1 Effects of the electron beam

It is first essential to unambiguously define the terms elastic and inelastic when referring to a collision between an incident electron and an atom in the sample. Throughout this thesis the term elastic will refer to collisions in which the total kinetic energy of the incident electron and atom is conserved, and any transfer of energy from the electron occurs *via* interaction with the atomic nucleus. In contrast, an inelastic collision refers to the transfer of kinetic energy from the incident electron to internal degrees of freedom of the sample atoms: electronic excitation mediated by electron-electron interactions.[i] Figure 1.1 shows a schematic of elastic and inelastic collisions.

These two types of collision have very different effects on materials studied in TEM. If an elastic collision transfers enough kinetic energy to the nucleus that it results in structural changes to the sample it is usually termed 'direct knock-on damage'; atom emission from the material or sputtering from surfaces is most commonly considered in this case, especially in the low dimensional systems studied here. This can also lead to bond rotations, the formation of interstitials, and in principle the initiation of other more complex reactions. In extreme cases, knock-on damage results in the complete destruction of molecules into atomic fragments,

[i]While these are commonly used definitions, 'elastic scattering' is also often used interchangeably with 'elastic collision', which is technically incorrect. This is the subset of elastic collisions for which the kinetic energy of the incident electron is also conserved, i.e. the electron passes through the sample without any transfer of energy but with modification of the direction of momentum. On the other hand, 'inelastic scattering' refers simply to any collision in which energy is transferred, but is often incorrectly used to refer specifically to inelastic collisions. Finally, 'elastic collision' is sometimes even conflated with 'elastic scattering', and assumed to involve no transfer of energy. Scientists coming from different fields (chemistry, physics, materials science, microscopy) typically use a different and occasionally mutually incompatible mix of the above, which can easily lead to confusion and miscommunication in a field as multidisciplinary as nanoscience!

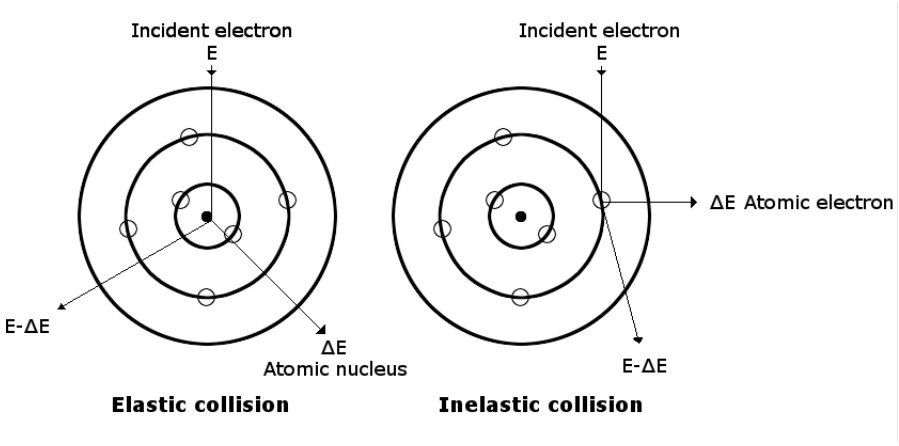


Figure 1.1: Left: an elastic collision, in which energy is transferred from the incident electron to the atomic nucleus. Right: an inelastic collision, in which energy is transferred from the incident electron to an atomic electron.

or the amorphisation of originally crystalline structures. The direct excitation of phonons or vibrational modes can lead to significant temperature increases in the area subjected to electron bombardment, while subsequent collisions between the primary knock on atom (PKA) and other atoms in the sample can lead to collision cascades of secondary or even higher order damage.

Inelastic collisions also provide several routes towards structure change. Ionisation of the sample can lead to radiolysis - the breaking of chemical bonds - which can cause similar effects to knock-on damage. The emission of secondary electrons as a result of ionisation, either directly or due to processes such as the Auger effect, can also cause substantial damage, and considering the lower kinetic energy of the emitted electrons this can even be the main source of damage. These electrons, or similar photon emission, can again lead to collision cascades, where a single original electron impact is the cause of substantial damage to the sample. If electrons are excited to below the ionisation continuum, chemical bonds can be weakened through the population of antibonding orbitals, and the relaxation of energy from excited electronic states into vibrational modes can lead to extreme heating of the sample.

While the effects of elastic collisions become more pronounced with increasing beam energy, the opposite is true for inelastic collisions. For general considerations of the different mechanisms of radiation damage in TEM, see references 18–20.

1.2 Materials studied

The nature of the material studied in TEM determines the primary damage mechanism it is susceptible to. In particular, whether the material is an electronic insulator or conductor is generally the most important consideration, as each of these is more readily affected by either elastic or inelastic collisions. The low dimensional materials studied in this work essentially eliminate the effects of the

secondary damage mechanisms mentioned in the previous section; they are typically at most only a few atoms thick in the plane of the electron beam, and so secondary electrons or atoms will be entirely emitted from the sample before causing additional damage. General reviews of the effects of irradiation on this kind of nanomaterial can be found in references 21 and 22.

In highly conductive materials such as metals, inelastic collisions have very little effect on atomic structure due to the availability of conduction electrons. Following ionisation, electron-hole recombination will occur as a sub-femtosecond process.[20] As this is much quicker than atomic motion, the nuclei essentially have no time to move under the effect of ionisation before it is quenched. As a result, knock-on damage caused by elastic collisions governs the damage mechanisms in these materials. In contrast, there is no such protection for insulating materials, and the effects of these processes can be severe: the deposition of electrons into the sample can lead to electrostatic charging, ionisation can lead to radiolysis, and electronic excitations can weaken bonds and drive local temperature increases under the beam by up to several hundred degrees for organic samples.[18] These processes typically dwarf the effects of knock-on damage, which are often considered negligible.

Although inelastic damage is not considered to be important in conducting materials insofar as its effect on atomic structure is concerned, these processes (ionisation, bond excitation, etc) will still occur. The conductivity of the sample material merely prevents them from having any structural effects such as radiolysis. In a similar fashion, energy from the beam will still be deposited to the material *via* electronic excitation and subsequent relaxation into vibrational or phonon modes; in thermally insulating materials this can lead to significant heating effects, while in thermally conductive materials the effect is usually negligible. On the other hand, in electronically insulating materials the knock-on damage discussed for conductive materials will still occur, but the rates of such processes are typically several orders of magnitude slower than the rates of inelastically induced processes. This is due to the incident electron having to pass very close to the atomic nucleus to induce knock-on damage, making the cross-sections of these processes incredibly small relative to those of inelastic ones.

The work in this thesis is predominantly split between two different materials: graphene, and organic molecules encapsulated inside single walled carbon nanotubes. This theoretical work would not be possible without close collaboration with several microscopists, who have kindly provided the included experimental TEM images. The experimental images of graphene were provided by Professor Andrey Chuvilin of CIC nanoGUNE, while the imaging of nanotube-encapsulated species was provided by Dr. Tom Chamberlain and Professor Andrei Khlobystov of the University of Nottingham, with aberration corrected images by Dr. Johannes Biskupek and Professor Ute Kaiser of Ulm University.

1.2.1 Graphene

The exceptional conductivity of graphene is considered to provide excellent protection against damage caused by inelastic collisions, in line with the general

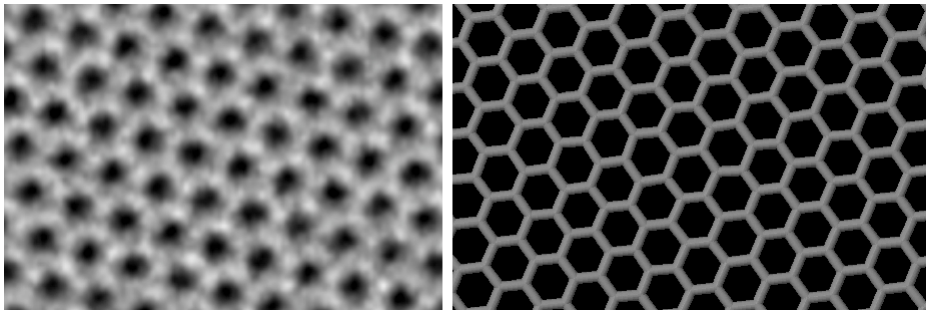


Figure 1.2: An example TEM image of graphene imaged at 80 kV (left, courtesy of Prof. Andrey Chuvilin, CIC NanoGUNE), with the atomic model structure shown to the right.

considerations in the previous section. These processes are not believed to have any effect on the atomic structure of graphene, although the electron beam will still affect the electronic structure on short timescales, for example through plasmon excitation.[21] The vibrational energy deposited into the sample *via* either the relaxation of electronic excitations or directly through elastic collisions dissipates quickly due to graphene's high thermal conductivity, typically limiting the increase in equilibrium temperature in the irradiated area to below 1 K for normal imaging conditions.[18,23]

As graphene is only one atom thick (thus only contributing a small contrast to TEM images), and has a highly ordered structure (its contribution to the TEM image can easily be removed *via* Fourier filtering), it has been considered to be 'the ultimate microscope slide'.[10] Coupling this with its high resistance to inelastic damage, graphene has even been used as a coating to remove or reduce this type of damage in other, non-conducting materials, for example by sandwiching a layer of molybdenum disulfide (MoS_2) between two graphene layers.[24] Graphene layers provide an 'electron sink' in good contact with the sample, and therefore remove the effects of ionisation or other electronic excitations in the same way as in graphene itself. In the example referenced, this removed 99.8% of the total damage observed under the beam; as the exit surface of the MoS_2 was also coated with a layer of graphene, the effects of the elastic knock-on damage were also removed.

Upon electron irradiation at beam energies over approximately 80 keV, the perfect graphene lattice becomes susceptible to irreversible direct knock-on damage in the form of carbon atom emission, while defective graphene (for example graphene edges or undercoordinated carbon atoms in defect sites) can be vulnerable at lower energies. Review articles concerning the response of graphene to electron irradiation and the defect structures commonly seen in such TEM studies can be found in references 9, 25, and 26, and this area will be discussed in much more detail in Chapter 4, which examines the dynamics of these defects under irradiation. Figure 1.2 shows an example experimental TEM image of graphene at the atomic resolution achievable with modern aberration correction.

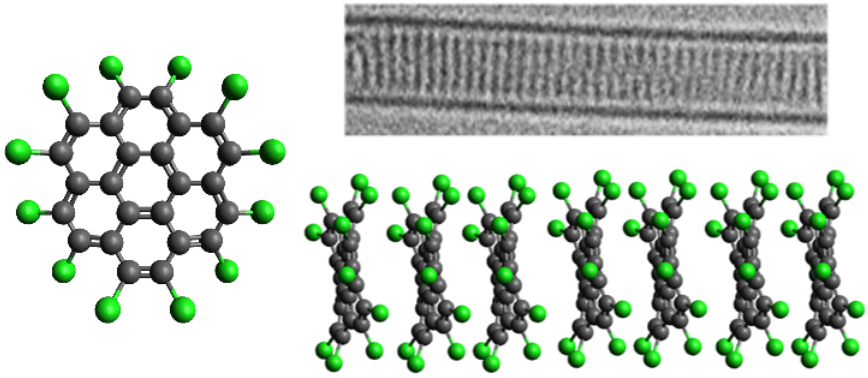


Figure 1.3: An example TEM image of perchlorocorone (PCC) molecules forming molecular stacks when encapsulated inside a single-walled carbon nanotube, imaged at 80 kV (top right, courtesy of Prof. Andrei Khlobystov, University of Nottingham). Models of a single PCC molecule and the molecular stack are shown to the left and bottom right, respectively.

1.2.2 Carbon nanotubes and encapsulated molecules

The effects of electron irradiation on carbon nanotubes are unsurprisingly very similar to those on graphene. Inelastic collisions can mostly be ignored due to the high conductivity of the nanotube, while direct knock-on processes are generally similar to those in graphene but with additional complexity due to the curvature of the tube.[27] Although all atoms in the nanotube are chemically identical, this curvature introduces different atom environments with respect to the beam, which respond to electron irradiation in different ways.[28] As the nanotube diameter decreases, the increasing strain makes atom emission more prevalent, with wide nanotubes tending towards graphene,[29] and even the nanotube chirality affects the susceptibility to irradiation damage.[30]

At 80 kV, as for graphene, all but the most narrow carbon nanotubes become impervious to knock-on damage from the beam, while nanotubes can act as inert containers for small species such as fullerenes and organic molecules.[31–33] If graphene can be considered as the 'ultimate microscope slide', above, then carbon nanotubes can perhaps be thought of as the 'ultimate test tubes', enabling the study of reactions of individual encapsulated molecules. Nanotube encapsulation provides many benefits, such as slowing down the molecular motion to the second timescale accessible to TEM, essentially fixing molecules in position, and reducing the dimensionality of the system. Small, planar molecules such as coronene are the prototypical organic species encapsulated in nanotubes, forming molecular stacks lined up along the tube length, as shown in Figure 1.3. Although these are typically stable once formed (assuming a good size match between the nanotube and molecule[32]), the molecules inside the tubes are vulnerable to damage from the electron beam.

Small organic molecules are especially prone to inelastic damage from the beam, as they are unable to efficiently dissipate any increase in temperature.

In organic crystals, ionisation can lead to reactions between molecules, and elastic collisions can form radical species, or cause collision cascades. The reduction of the number of nearest neighbours when moving from a crystalline structure to the gas phase or low dimensional nanostructure greatly reduces damage by both removing this type of cascading secondary damage, and decreasing the likelihood that an activated molecule (e.g. *via* ionisation) will react.[33,34] In addition to this benefit, encapsulation is believed to provide significant direct protection against inelastic collisions in the same manner as the graphene coating mentioned in the previous section, although this has been shown to depend on the quality of the contact between the molecules and the nanotube walls.[35] Although the contact between molecules and the nanotube has a lower surface area than in the case of sandwiching a two dimensional structure between two graphene sheets, and therefore the reduction in the damage due to inelastic collisions may potentially be less than graphene's essentially perfect protection, the contact is typically very good; most molecular stacks seen are tilted due to the sterical effect imposed by the nanotube walls.[36] This is reflected in the increased radiation resistance of encapsulated species: in the experimental results discussed in Section 3.3 the average number of electrons per square nanometre required for the decomposition of coronene molecules is increased from approximately 1×10^4 to 5×10^6 upon encapsulation.[37] Specific reactions of nanotube-encapsulated molecular species under electron irradiation will be discussed in more detail in Chapter 3.

Chapter 2

Computational and theoretical techniques

By far the most important and useful piece of information about an irradiation induced reaction is its cross-section. This is the area through which an electron must pass in order to transfer enough energy that the reaction is induced, whether *via* interactions with the atomic electrons or the nucleus, as discussed earlier. Reaction cross-sections are normally measured in barn (1 b = 10^{-28} m^2), which demonstrates the tiny areas involved; reaction-inducing collisions are rare occurrences! Cross-sections can be taken as shorthand for the probability of reactions occurring, and if they are known then the rate of the reaction can be calculated from the flux of the beam. Alternatively, cross-sections can be measured from experimental reaction rates, meaning that a powerful comparison between theory and experiment can be made: given a theoretically derived cross-section based on a particular hypothesised process, the calculation of an equivalent value from experiment can be used to confirm or to refute the assumed mechanism, or provide insight into it.

Of course, this requires a method for theoretically deriving accurate cross-sections for the processes you are interested in, as well as the ability to accomplish the same from experimental observations. In this chapter, elastic electron collisions will be considered with a view to a practical method for obtaining accurate cross-sections for the reactions studied in Chapters 3 and 4. Section 2.1 details the theory of a relativistic electron colliding with an atomic nucleus and the transfer of energy involved, resulting in an expression that can be used to calculate theoretical reaction cross-sections. Consideration is given to the situations in which this expression is valid, and its expected accuracy. Section 2.2 then details the general theory behind a common computational modelling method, used to calculate a key system-dependent parameter (the threshold energy) required for such cross-section calculations. Finally, and unrelated to the calculation of reaction cross-sections, Section 2.3 briefly introduces the multislice approach to TEM image simulation, another useful tool for comparisons between theory and experiment, and presents two examples of its use.

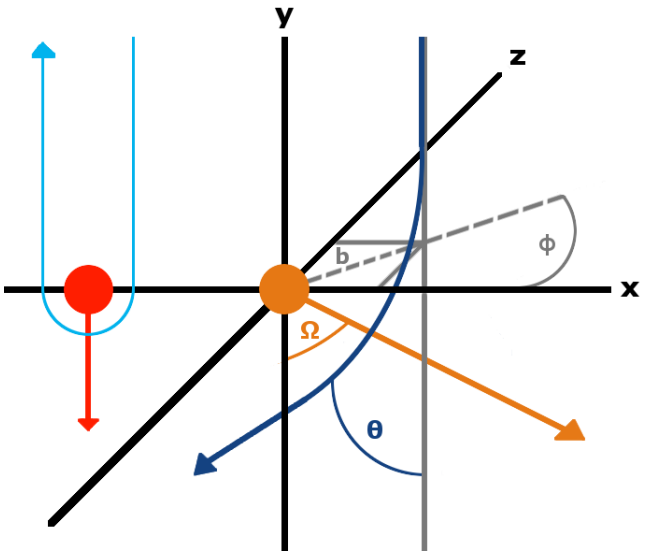


Figure 2.1: Representation of the three-dimensional scattering geometry of an elastic electron (dark blue) collision with a nucleus (orange), showing the electron scattering angle θ, the atom scattering angle Ω, the azimuthal angle ϕ, and the impact parameter b. The electron beam is oriented in the y-axis. The case in which $\theta = \pi$, $\Omega = 0$, and $T = T_{max}$ is shown on the left in light blue and red.

2.1 Theory of elastic electron collisions

2.1.1 The McKinley-Feshbach approximation

The elastic collision of an incident electron with a positively charged atomic nucleus is governed by the Coulomb potential

$$V(r) = -\frac{Ze^2}{4\pi\epsilon_0 r} \tag{2.1}$$

in which Z is the nuclear charge, e is the elementary charge, ϵ_0 is the permittivity of free space, and r is distance. When considering the nucleus and electron as point particles with no spin (and ignoring relativistic and recoil effects) the cross-section of this scattering is given by the Rutherford cross-section

$$\sigma_R = \left(\frac{Ze^2}{4\pi\epsilon_0 2m_e c^2}\right)\frac{1-\beta^2}{\beta^4}\csc^4\left(\frac{\theta}{2}\right) \tag{2.2}$$

where m_e is the mass of the electron, $\beta = v_e/c$ is the ratio of electron velocity v_e to the speed of light c, and θ is the electron scattering angle (shown in Figure 2.1).

In TEM studies of carbon nanomaterials, incident electron energies of 20 - 200 keV are currently used; the most commonly used accelerating voltage is 80 kV, as this is typically the maximum achievable without introducing beam induced defects into the samples. As an 80 keV electron is travelling at 50% of the speed of light, the Lorentz factor is 1.16 and relativistic effects will be significant, rendering the Rutherford cross-section unsuitable. The effects of electron spin and relativity

can be accounted for by finding a solution to the Dirac wave equation. For the case of the Coulombic interaction between an incident electron and atomic nucleus, and taking the unit of length to be $h/2\pi p$ (where p is momentum), this is[38]

$$\left[\nabla^2 + 1 + \frac{2Z\alpha}{\beta r} + \frac{(Z\alpha)^2}{r^2} - i\frac{Z\alpha}{r^3}\rho_1(\sigma r)\right]\Psi = 0 \tag{2.3}$$

where ∇^2 is the Laplacian operator, $\alpha = 2\pi e^2/hc \approx 1/137$ is the fine structure constant,[i] and ρ and σ are the Dirac matrices. Here, the third term represents the Rutherford-like electron scattering, with relativistic and spin effects contained in the fourth and fifth term respectively. As the velocity of the incident electron increases, β increases, and the latter two terms become significant, while the Z^2 dependency in the fourth term ensures that relativistic effects remain relatively low for lighter elements.

Mott derived an exact solution to Equation 2.3 in the form of a pair of infinite series representing the incident and scattered waves. However, this solution is only convergent when the potential $V(r)$ tends to zero faster than $1/r^2$, meaning that it is not practical for the Coulomb potential 2.1. As a result, many approximate analytical solutions based on Mott's work were developed,[39–42] valid for different regimes.[ii] For the purposes of the work contained in this thesis, which examines electron scattering by light elements such as carbon, by far the most appropriate and useful is the McKinley-Feshbach approximation.[45] By expanding the coefficients in the Mott solution in a power series in $Z\alpha$ and $Z\alpha/\beta$, up to and including the term in $Z\alpha^4$, they derived an accurate approximate solution as an adjustment to the Rutherford cross-section:

$$\sigma(\theta) = \sigma_R\left[1 - \beta^2\sin^2\frac{\theta}{2} + \pi\frac{Ze^2}{\hbar c}\beta\sin\frac{\theta}{2}\left(1 - \sin\frac{\theta}{2}\right)\right] \tag{2.4}$$

Although the expansion used in the McKinley-Feshbach approximation is only valid for relativistic electrons ($\beta \approx 1$), the final form of Equation 2.4 means that as β tends to 0, the cross-section correctly tends to the non-relativistic Rutherford cross-section. This can therefore be used at all beam energies below approximately 100 MeV, at which point the wavelength of the incident electron becomes small enough that the nucleus can no longer be considered as a point object. The neglect of terms in $Z\alpha^5$ and above results in an accurate solution for $Z\alpha \leq 0.2$; practically speaking this corresponds to all elements lighter than nickel ($Z = 28$). Figure 2.2 compares the Rutherford, Mott, and McKinley-Feshbach cross-sections for carbon and gold, and shows that while the McKinley-Feshbach approximation perfectly reproduces the exact solution for carbon, it performs much worse than even the Rutherford cross-section for gold.

As the Coloumb potential diminishes asymptotically with distance, total (integrated) Rutherford and McKinley-Feshbach cross-sections have infinite area. In order to calculate integrated cross-sections for real systems, a screening term must

[i] More commonly and henceforth $\alpha = e^2/4\pi\epsilon_0\hbar c$, in SI units.

[ii] In fact, most of the derivations referenced here, including Mott's own work, contain errors and are incorrect.[43] For a interesting and thorough history of this period, see Chapter 2.5 of reference 44.

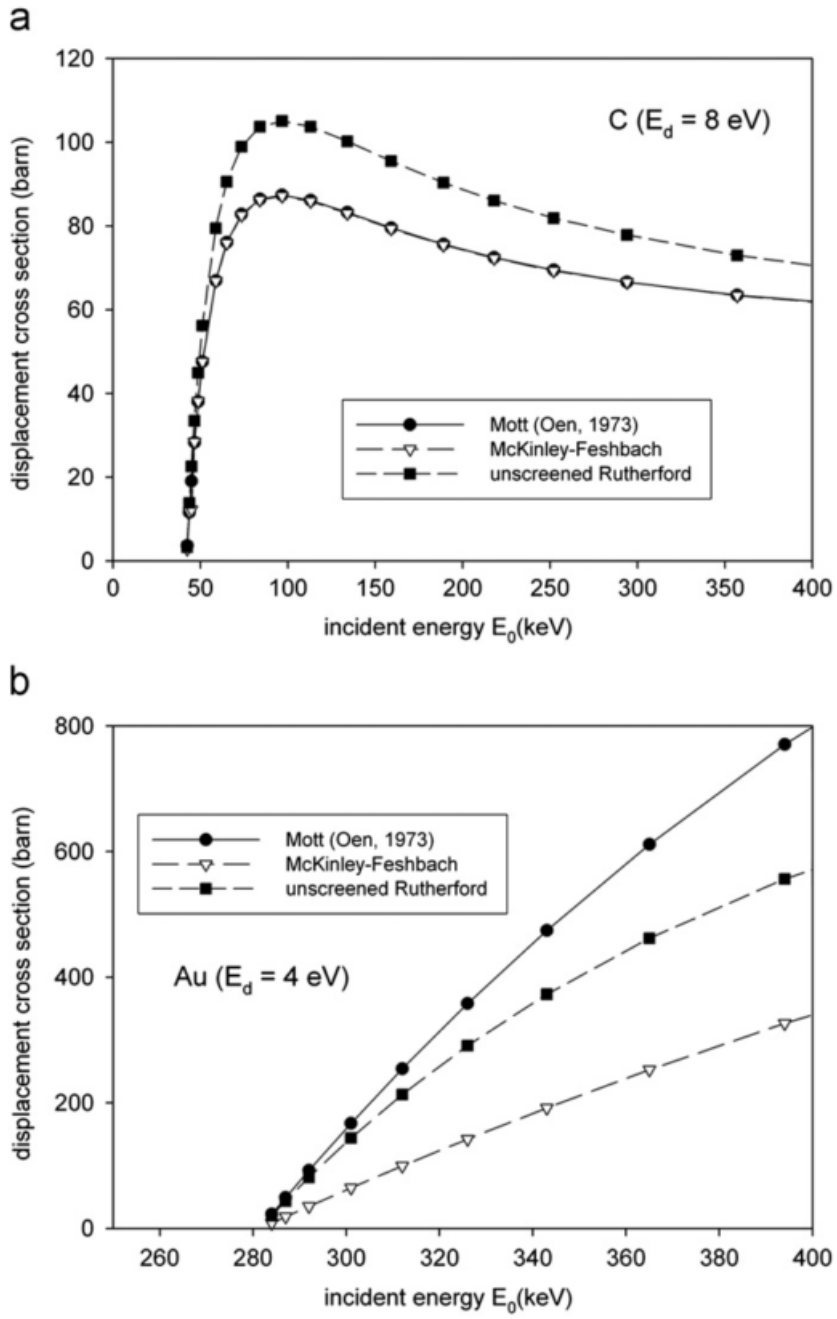


Figure 2.2: A comparison of the Rutherford, Mott, and McKinley-Feshbach cross-sections as a function of beam energy, for (a) carbon ($Z = 12$) and (b) gold ($Z = 79$). Reprinted with permission from reference 19.

be introduced; for example, a cut-off distance beyond which the scattering angle θ is considered negligible and the potential is set to zero. In a physical system, the atomic electrons provide this shielding for neutral atoms and the radius of the inner electrons can therefore be used for this distance. As shown below, the practical use of the McKinley-Feshbach cross-section to calculate integrated cross-sections of reactions introduces a natural cut-off (the threshold energy of the reaction E_d), and so this screening term can be neglected. In order to displace atoms by a sufficiently large distance that chemical reactions are initiated, the transmitted energy must be considerable and the incident electron must pass very close to the target nucleus, such that the effect of shielding by atomic electrons is negligible.[46]

It is worth mentioning recent developments following a different approach to that of the analytical approximations to Mott's exact solution. In 2013, Boschini *et al.*[47] numerically calculated the ratio of the Mott cross-section to the Rutherford cross-section for a range of nuclear charges, scattering angles, and electron energies. By interpolating these results, they tabulated 30 coefficients per element (for all elements $1 \leq Z \leq 118$) for use with a straightforward analytical expression. This generally only differs from the exact Mott solution by an order of 10^{-3} to 10^{-2}. Although in principle this opens up the entire periodic table to accurate cross-section calculations, in practice it is of minimal use at the low beam energies discussed in the following work; for the atomic masses at which the McKinley-Feshbach approximation is no longer accurate, the amount of energy transferred to these elements is so low that in general no reactions will be induced by direct knock-on damage.

2.1.2 Transferred energy

The above discussion of cross-sections has been in terms of the scattering angle θ. When considering reactions induced by the beam, the amount of energy that can be transferred to an atom is generally a more useful parameter than the scattering angle; after all, following the collision we are more interested in what happens to the atom than what happens to the scattered electron! The energy T transferred to a stationary nucleus *via* an elastic collision, as a function of the scattering angle, is

$$T(\theta) = \frac{2m_n E(E + 2m_e c^2)}{(m_n + m_e)^2 c^2 + 2m_n E} \sin^2\left(\frac{\theta}{2}\right) = T_{max} \sin^2\left(\frac{\theta}{2}\right) \tag{2.5}$$

where m_n is the mass of the nucleus and E is the kinetic energy of the incident electron. The maximum energy that can be transferred from a single electron to an atomic nucleus, T_{max}, occurs when $\theta = \pi$. The scattering geometry of an elastic collision is shown in Figure 2.1, and T_{max} is shown as a function of beam energy for the elements that are relevant in this thesis in Figure 2.3.

Considering this relationship, substituting

$$sin\left(\frac{\theta}{2}\right) = \sqrt{\frac{T}{T_{max}}} \tag{2.6}$$

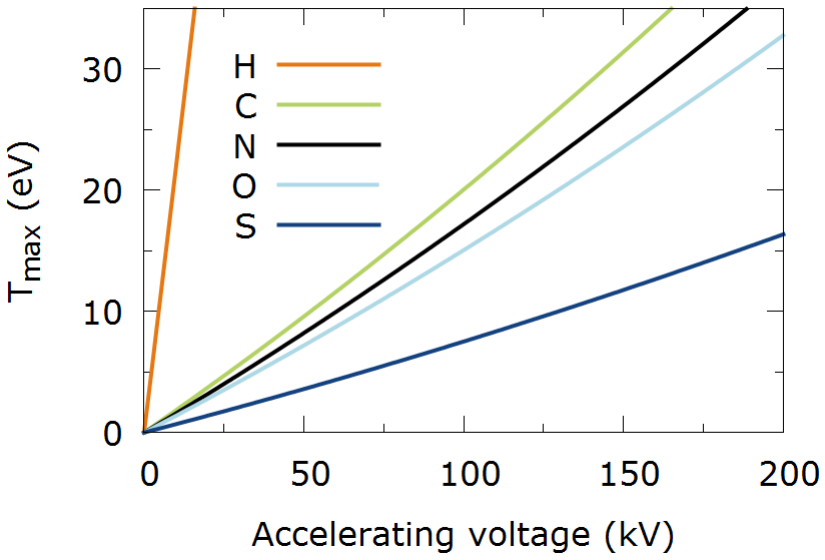


Figure 2.3: The maximum energy that can be transmitted to a stationary atom of a variety of elements, as a function of the accelerating voltage of the beam. Calculated using Equation 2.5.

into Equation 2.4 results in a cross-section as a function of the transmitted energy T:[28]

$$\sigma(T) = \left(\frac{Ze^2}{4\pi\epsilon_0 2m_e c^2}\frac{T_{max}}{T}\right)^2 \frac{1-\beta^2}{\beta^4}\left[1-\beta^2\frac{T}{T_{max}} + \pi\frac{Ze^2}{\hbar c}\beta\left(\sqrt{\frac{T}{T_{max}}} - \frac{T}{T_{max}}\right)\right] \tag{2.7}$$

Any given beam-induced reaction will only occur when when the energy transferred from the beam is above a critical threshold energy, i.e. the minimum energy required to initiate the reaction such that it does not immediately reverse. This threshold energy $E_d(\Omega, \phi)$ will depend on the angle at which the energy is transferred to the atom Ω and the azimuthal angle ϕ (see Figure 2.1), where

$$\Omega = \frac{\pi - \theta}{2} \tag{2.8}$$

In order to find the total cross-section of the reaction, Equation 2.7 must be integrated in the energy domain where the transferred energy is greater than the threshold energy for the associated scattering angles:

$$\sigma_d = \int_{T>E_d(\Omega,\phi)} \sigma_d(T)\frac{4\pi}{T_{max}}dT \tag{2.9}$$

2.1.3 Isotropic approximation of the threshold energy

Although for real systems the threshold energy will be a function of the scattering angles, a simpler case can be considered in which the reaction proceeds as long as the **minimum** threshold energy E_d is transferred to the atom, in any direction.[iii] In this isotropic approximation of the threshold energy the previous integral takes the much simpler form

$$\sigma_d = \int_{E_d}^{T_{max}} \sigma_d(T) \frac{4\pi}{T_{max}} dT \tag{2.10}$$

Inserting Equation 2.7 into 2.10, integrating and rearranging algebraically gives[48]

$$\sigma_d = 4\pi \left(\frac{Ze^2}{4\pi\epsilon_0 2m_e c^2} \right)^2 \frac{1-\beta^2}{\beta^4} \left\{ \frac{T_{max}}{E_d} - 1 - \beta^2 \ln\left(\frac{T_{max}}{E_d} \right) + \pi \frac{Ze^2}{\hbar c} \beta \left[2 \left(\frac{T_{max}}{E_d} \right)^{1/2} - \ln\left(\frac{T_{max}}{E_d} \right) - 2 \right] \right\} \tag{2.11}$$

It is worth commenting in detail about the validity of the isotropic approximation of the threshold energy, as it is normally only reasonable in very specific circumstances. As θ decreases from π, under the isotropic approximation the threshold energy is fixed, while T decreases from T_{max} to the point at which $T < E_d$, and the addition to the total cross-section is zero. In a real system, where E_d is anisotropic and may decrease with decreasing θ (for example, the emission of an atom from a graphene edge with the beam orthogonal to the graphene plane) this is generally a poor approximation, as the interplay between the energy that is transferred at a given scattering angle ($T(\theta, \phi)$) and the associated threshold energy at that scattering angle ($E_d(\theta, \phi)$) determines the contribution to the cross-section. However, consider the case in which the beam direction is aligned with the angle Ω with the minimum value for E_d, as in the most common experimental TEM setup for studying graphene. Under the isotropic approximation we have the same behaviour as described above, while in this real system as θ decreases, E_d increases and T decreases, and so $T < E_d$ is quickly reached. Hence the same qualitative behaviour is exhibited in both the real and isotropic systems, and so the isotropic approximation is a suitable one. It will result in slightly overestimated reaction cross-sections, as the electron scattering angle at which T becomes less than E_d will be overestimated.

The error introduced by this approximation is excellently demonstrated by the work of Zobelli *et al.*[28,49] Density functional tight-binding (DFTB) calculations were used to calculate E_d for the emission of an atom from graphene at various emission angles Ω and ϕ. An anisotropic map of the threshold energy was produced by interpolating these values, and then used to calculate the emission cross-section as a function of beam energy using Equation 2.9. The minimum threshold energy found in these calculations was 23 eV, for emission normal to the graphene plane.

[iii] Unless otherwise stated, 'threshold energy' and E_d will from now on refer to this minimum threshold energy, i.e. the lowest threshold energy E_d of the set $E_d(\Omega, \phi)$.

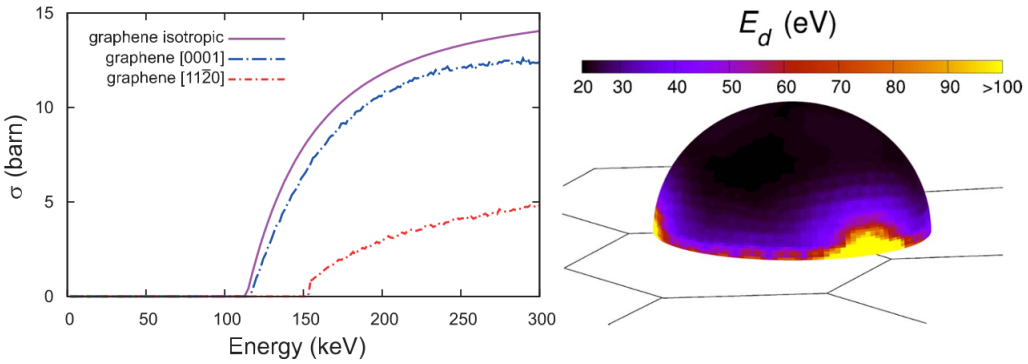


Figure 2.4: Left: a demonstration of the suitability of the isotropic approximation of the threshold energy (purple line), for the emission of a carbon atom from perfect graphene. The approximation works very well when the beam direction corresponds to the direction with the minimum threshold energy (blue line), but can only provide an upper limit when this is not the case (red line). Right: a map of the anisotropy of the threshold energy, calculated with DFTB-MD simulations. Adapted with permission from references 28 and 49.

Using this value in Equation 2.11 provided an equivalent curve for the isotropic approximation of the threshold energy. Figure 2.4 summarises these results, which quantitatively demonstrate the discussion in the previous paragraph: in the case where the beam direction is normal to the graphene plane, overlapping with the direction of the minimum threshold energy, there is very close agreement between the isotropic and anisotropic cases, especially around the the onset of damage at the important beam energy where $T_{max} = E_d$. On the other hand, when the beam direction is parallel to the graphene plane, the true cross-section is very poorly estimated and the isotropic approximation is unsuitable.

Taking a 150 keV electron beam as an example, the map shown in Figure 2.4 demonstrates how the isotropic approximation provides an accurate description in the former case: for increasingly large electron scattering angles, T increases towards 31 eV (T_{max}) and E_d decreases towards 23 eV, resulting in emission. Reducing the electron scattering angle to 120 degrees, the transferred energy falls below 23 eV, while the threshold energy remains approximately constant. At even smaller values of θ, T continues to fall while E_d increases sharply to very high energies. Thus, in the small region of angle space in which atom emission is possible, the threshold energy behaves isotropically, and the heavily anisotropic regions outside of this play no role: they do not contribute to the emission cross-section and so their poor description does not introduce inaccuracy. It should be noted that even when this is not the case, the isotropic approximation with the minimum value of E_d can still be used to find an upper limit of the total cross-section, regardless of the direction of the beam.

The computational expense of fully mapping the anisotropy of the threshold energy is considerable, making the isotropic approximation an incredibly useful one when it is applicable. For the example discussed above and shown in Figure 2.4,

a total of approximately 2 nanoseconds of molecular dynamics time was required for a system of 200 atoms.[49] If the isotropic approximation can be used, the computational expense is typically three orders of magnitude smaller, enabling either an increase in the accuracy of the calculated energies, the use of a higher level of computational theory, or larger or more complex systems to be studied (such as those in which there are multiple atom environments and therefore multiple cross-sections).

2.1.4 Contribution of atomic thermal motion

It was observed that that there was an apparent mismatch between computationally calculated values of E_d and experimental observations. Although the McKinley-Feshbach approximation is known to be very accurate compared to the exact solution (see Figure 2.2), the onset of knock-on damage was observed to generally occur at lower beam energies than predicted theoretically. This inaccuracy was originally ascribed to various inadequacies in the calculations of E_d, for example due to the omission of excited-state dynamics.[28] Although it was later shown that the explicit inclusion of electron dynamics only has a minor effect on the results of such simulations,[50] in principle the beam could be responsible for the weakening of bonds *via* electronic excitations, thus reducing the threshold energy.[51] An alternative proposal was that the systematic overestimation of dissociation energies in density functional theory (DFT) and DFTB was the source of the error.[49]

However, in 2012 Meyer *et al.*[52,53] demonstrated that this was actually due to an approximation made in the kinematics determining the transfer of energy; the original thermal motion of impacted atoms must be taken into account rather than considering the atoms to be at rest. Although this is somewhat surprising considering that the thermal motion of atoms in the sample is very small compared to the energy of the beam, its inclusion makes a large difference to the transfer of energy between the incident electron and sample atom. An adjustment must be made when calculating the maximum transmitted energy T_{max} - when the atom is travelling parallel to the incident electron due to thermal lattice vibrations in the sample, this can be larger than the value calculated using Equation 2.5.

Considering the collision between an incident electron with kinetic energy E and a **moving** atom with kinetic energy E_n, when $m_n \gg m_e$ and $c^2 m_n \gg E$,[52]

$$T_{max} = \frac{1}{2m_n}\left[r\left(r + \frac{2t}{c}\right) + \left(\frac{t}{c}\right)^2\right] \tag{2.12}$$

$$r = \frac{1}{c}\sqrt{E(E + 2m_e c^2)} + m_n V_n \tag{2.13}$$

$$t = \sqrt{(E + E_n)(E + 2m_e c^2 + E_n)} \tag{2.14}$$

where V_n is the initial velocity of the atom parallel to the electron beam. For the initial velocity V_n of the atom, the Gaussian probability distribution holds

$$P(V_n, T)dV_n = \frac{1}{\sqrt{2\pi \left\langle v_T^2 \right\rangle}} exp\left(-\frac{V_n^2}{2\left\langle v_T^2 \right\rangle}\right) dV_n \tag{2.15}$$

The mean square velocity $\left\langle v_T^2 \right\rangle$ of the atom at temperature T can be calculated according to the Debye model if the Debye temperature of the material θ_D (the temperature of the material's highest normal mode of vibration) is known

$$\left\langle v_T^2 \right\rangle = \frac{9k_B}{8m_n}\theta_D + \frac{9k_BT}{m_n}\left(\frac{T}{\theta_D}\right)^3 \int_0^{\theta_D/T} \frac{x^3}{exp(x)-1} dx \tag{2.16}$$

where k_B is the Boltzmann constant. Alternatively, if the Debye temperature is unknown, the probability of the atomic velocities can simply be obtained directly from the Maxwell-Boltzmann velocity distribution

$$P(V_n, T)dV_n = \sqrt{\frac{m_n}{2\pi k_B T}} exp\left(-\frac{m_n V_n^2}{2k_B T}\right) dV_n \tag{2.17}$$

By numerically integrating the cross-section (Equation 2.11) over all possible atomic velocities in T_{max} (Equation 2.12), weighted by their probabilities (Equation 2.15 or 2.17), the total reaction cross-section can be calculated accounting for the thermal vibrations of the sample. In practice, a function must be included in the integration to replace unphysical negative cross-sections, obtained when $T_{max} < E_d$, with zero. The inclusion of the thermal vibrations introduces a smooth onset of knock-on damage at low beam energies, rather than a sudden appearance at the characteristic beam energy where $T_{max} = E_d$. The non-zero cross-sections below this energy correspond to reactions that only take place when the thermal motion of the atom increases the transferred energy above the threshold energy for that reaction. Using this method, the theoretically calculated threshold energies more accurately reproduce the energies at which knock-on damage is witnessed experimentally, while at higher beam energies this effect is negligible. This is shown in Figure 2.5.

Just as T_{max} is replaced by the expression given in Equation 2.12, the dependence of the transmitted energy on θ given in Equation 2.5 is no longer correct, unless the electron velocity is much higher than the atom velocity, and

$$1 - \frac{4r\frac{t}{c}}{(r+\frac{t}{c})^2} \ll 1 \tag{2.18}$$

When this is not the case (at approximately 10 kV or below), the atomic motion significantly affects the electron scattering angle and this approximation is no longer valid. A subsequent study[54] compared the expression 2.12 given by Meyer *et al.* above to an exact numerical expression for the energy transfer, and found that while there was an excellent agreement at 300 K, at high temperatures (3500 K) differences emerged between the two methods. However, this difference remained very small compared to results using a static lattice, even at such highly elevated temperatures. This paper also stated that a limitation of the method is the use of the Debye model, which is no longer valid at low temperatures (<150 K).[54] In graphene this is likely only to have a limited effect, as most of the contribution

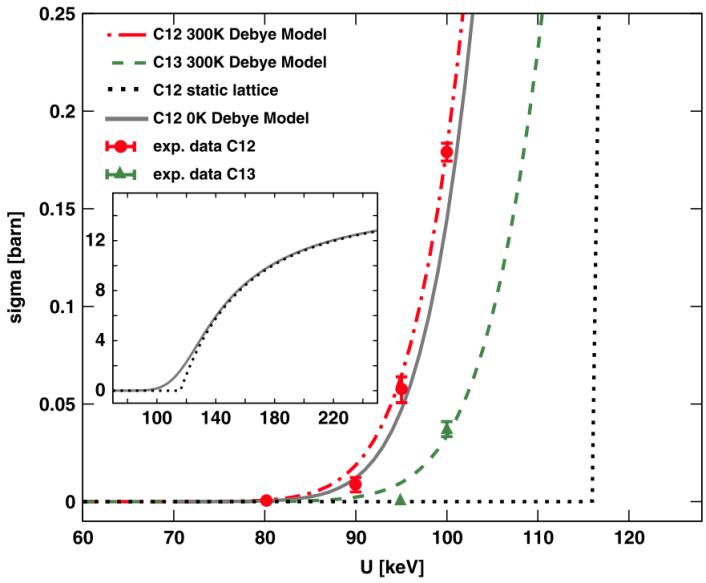


Figure 2.5: The experimentally measured cross-sections for emission of an atom from graphene, and the calculated cross-sections both including and excluding thermal lattice contributions to the transmitted energy. The effect of increasing the atomic mass is also demonstrated with ^{13}C, discussed in more detail in Section 3.3. Reprinted with permission from reference 53.

of the thermal lattice is provided by the zero-point energy, and so there is only a very small (essentially negligible) dependence on the temperature, as shown in Figure 2.5.

2.1.5 Regime of validity

The cross-sections calculated in the subsequent work are done so using the above framework, using the Debye model when studying graphene and a Maxwell-Boltzmann distribution when considering molecular species. In graphene, the use of the Maxwell-Boltzmann distribution at 298 K produces a thermal contribution to the cross-section at low electron energies that lies exactly between that produced when using the Debye model and the static lattice. As the isotropic approximation of the threshold energy is used, the only unknown parameter in Equation 2.11 required to calculate the cross-section of a reaction (and therefore its rate in any given experimental conditions) is the minimum threshold energy E_d. This must be calculated computationally, as detailed in the next section. Table 2.1 summarises the conditions for which various approximations made in this theoretical framework are valid.

Table 2.1: A summary of the limits for the theoretical framework used to calculate elastic cross-sections of beam-induced reactions, as discussed in this section.

Parameter	**Limit**	**Reason**
Nuclear charge (Z)	<27	The McKinley-Feshbach approximation.
Beam energy (E)	<100 MeV	The electron begins to probe nuclear structure.
	>10 keV	Thermal atomic motion affects θ.
Temperature (T)	< 3000 K	Approximations in the thermal contribution to T.
	>150 K	Invalidity of the Debye model.

2.2 Computational details

As shown in the previous section, given a threshold energy E_d of a reaction, the cross-section of that reaction can be calculated for any beam energy. In practice, threshold energies can be calculated computationally using a range of different methods and levels of theory; for the subsequent work density functional theory (DFT) is used. In this section a general overview of the theory behind DFT is given. This begins with an introduction to more traditional wavefunction-based methods of computational chemistry, as elements of this are used explicitly in the DFT calculations. More specific considerations of how to best model the systems being studied are included in the relevant section, 3.1.

2.2.1 Wavefunction-based approaches

The Schrödinger equation

The total energy E of a system of interacting electrons N and nuclei M (and therefore any derivatives of the energy) can be calculated by solving the Schrödinger equation

$$\hat{H}\Psi(N,M) = E\Psi(N,M) \tag{2.19}$$

in which $\hat{H}$ is the Hamiltonian operator, consisting of terms accounting for the kinetic energy of the electrons $\hat{T}_e$, the kinetic energy of the nuclei $\hat{T}_n$, the electrostatic attraction between the electrons and nuclei $\hat{V}_{ne}$, the electrostatic interaction between the electrons $\hat{V}_{ee}$, and the electrostatic interaction between the nuclei $\hat{V}_{nn}$, respectively:

$$\hat{H} = \hat{T}_e + \hat{T}_n + \hat{V}_{ne} + \hat{V}_{ee} + \hat{V}_{nn} \tag{2.20}$$

$$\hat{H} = \sum_i^N \frac{-\hbar^2}{2m_e}\nabla_i^2 + \sum_A^M \frac{-\hbar^2}{2m_A}\nabla_A^2 + \sum_i^N \sum_A^M \frac{-e^2 Z_A}{r_{iA}} + \sum_{i>j}^N \frac{e^2}{r_{ij}} + \sum_{A>B}^M \frac{e^2 Z_A Z_B}{r_{AB}} \tag{2.21}$$

Here, i and j denote the N electrons, A and B denote the M nuclei, and r_{ij} is the distance between the particles i and j.

The Born-Oppenheimer approximation

As the mass of an electron is far smaller than that of even the smallest nuclei, the nuclei move much slower than the surrounding electrons, which react to changes in the environment before the nuclei can appreciably move. The Born-Oppenheimer approximation simplifies the wavefunction of the system by assuming that the electrons move around fixed nuclei, separating it into electronic and nuclear components

$$\Psi(N, M) = \psi_M(N)\psi(M) \tag{2.22}$$

where the electronic wavefunction $\psi_M(N)$ depends on the nuclear coordinates. The energy determined from the electronic Hamiltonian $\hat{H}_{el} = \hat{T}_e + \hat{V}_{ne} + \hat{V}_{ee}$ is added to the nuclear repulsion term $\hat{V}_{nn}$ in order to obtain the total energy of the system; as the nuclei move with the coordinate system the term $\hat{T}_n$ is equal to zero.

The Hartree-Fock approximation

The Hartree-Fock (HF) approximation reduces the many body problem of Equation 2.22 into a set of solvable one-particle problems by approximating the N-electron wavefunction by the product of N one-electron wavefunctions, spin orbitals $\chi_i(\mathbf{x}_i)$ consisting of a spatial orbital $\Phi_i(\mathbf{r})$ and one of the spin functions $\alpha(s)$ or $\beta(s)$. This represents N non-interacting electrons moving in a field of effective potential V_{eff}; each electron only interacts with the average distribution of all other electrons in the system.

$$\Psi(\mathbf{x}_1, \mathbf{x}_2, \mathbf{x}_3, ...) = \chi_1(\mathbf{x}_1)\chi_2(\mathbf{x}_2)\chi_3(\mathbf{x}_3) \tag{2.23}$$

$$\chi_i(\mathbf{x}_i) = \Phi_i(\mathbf{r})\sigma(s) \tag{2.24}$$

The Pauli principle states that the wavefunction for two identical fermions (such as electrons) must be antisymmetric, i.e. the wave function must change sign when the fermions are exchanged. In order to satisfy this the product of these wavefunctions must be antisymmetrised, which ensures that the wavefunction is zero when two or more spin orbitals are identical (this is the Pauli exclusion principle: no two electrons of identical spin can occupy the same spatial orbital). This is accomplished by writing the wavefunction as the Slater determinant, Φ_{SD}, rather than as the simple Hartree product in Equation 2.23.

$$\Psi = \Phi_{SD} = \frac{1}{\sqrt{N!}} \begin{vmatrix} \chi_1(\mathbf{x}_1) & \chi_2(\mathbf{x}_1) & \cdots & \chi_N(\mathbf{x}_1) \\ \chi_1(\mathbf{x}_2) & \chi_2(\mathbf{x}_2) & \cdots & \chi_N(\mathbf{x}_2) \\ \vdots & \vdots & \ddots & \vdots \\ \chi_1(\mathbf{x}_N) & \chi_2(\mathbf{x}_N) & \cdots & \chi_N(\mathbf{x}_N) \end{vmatrix} \tag{2.25}$$

Reformulating the electronic Hamiltonian in terms of one electron i rather than two gives the Fock equation

$$\hat{f}\chi_i = \epsilon_i \chi_i \tag{2.26}$$

where ϵ_i is the orbital energy and $\hat{f}$ is the Fock operator, consisting of kinetic energy and electron-nuclear attraction terms, plus the Hartree-Fock potential V_{HF} which accounts for the average repulsive potential caused by all the other electrons in the system:

$$\hat{f}_i = -\frac{1}{2}\nabla_i^2 - \sum_A^M \frac{Z_A}{r_{iA}} + V_{HF}(i) \tag{2.27}$$

$$V_{HF}(\mathbf{x}_1) = \sum_j^N [\hat{J}_j(\mathbf{x}_1) - \hat{K}_j(\mathbf{x}_1)] \tag{2.28}$$

This potential is composed of the Coulomb operator $\hat{J}$, which accounts for the potential felt by an electron at $\mathbf{x}_1$ due to the charge of an electron in spin orbital χ_j

$$\hat{J}_j(\mathbf{x}_1) = \int |\chi_j(\mathbf{x}_2)|^2 \frac{1}{r_{12}} d\mathbf{x}_2 \tag{2.29}$$

It also contains the exchange operator $\hat{K}$, in which the variables in two spin orbitals are exchanged. This is caused by the antisymmetry of the Slater determinant and acts on electrons of like spin

$$\hat{K}_j(\mathbf{x}_1)\chi_i(\mathbf{x}_1) = \int \chi_j^*(\mathbf{x}_2) \frac{1}{r_{12}} \chi_i(\mathbf{x}_2) d\mathbf{x}_2 \chi_j(\mathbf{x}_1) \tag{2.30}$$

The electron labels i and j can correspond to the same electron. In the Coulomb operator in Equation 2.29 this produces a false self-interaction energy, which is exactly cancelled out by the exchange term when $i = j$. Although this is therefore not an issue in HF calculations, in density functional theory this is not automatically accounted for and needs to be explicitly considered.

Basis functions

Following an initial guess of the spin orbitals, they can be iteratively optimised to minimise the energy until it is considered to be converged. The initial guess of the spatial part of the spin orbitals in this self-consistent field (SCF) calculation can be calculated by building a linear combination of a set of L basis functions η_μ

$$\phi_i = \sum_{\mu=1}^{L} c_{\mu i} \eta_\mu \tag{2.31}$$

in which $c_{\mu i}$ is the expansion coefficient, determining the weight of the contribution of the basis functions (the atomic orbitals) to the molecular orbital. Inserting this equation for the orbitals into the Fock equation 2.26, multiplying by an arbitrary basis function η_ν, and integrating over space results in

$$\sum_{\mu=1}^{L} c_{\mu i} \int \eta_\mu(\mathbf{r}) \hat{f}(\mathbf{r}) \eta_\nu(\mathbf{r}) d\mathbf{r} = \epsilon_i \sum_{\mu=1}^{L} c_{\mu i} \int \eta_\mu(\mathbf{r}) \eta_\nu(\mathbf{r}) d\mathbf{r} \tag{2.32}$$

This can be rewritten as the Roothaan-Hall equation

$$\mathbf{FC} = \epsilon \mathbf{SC} \tag{2.33}$$

where the Fock matrix $\mathbf{F}$ is the integral on the left of Equation 2.32, $\mathbf{S}$ is the integral on the right of Equation 2.32 (the overlap matrix of the basis functions), ϵ is a matrix containing the orbital energies in the diagonal terms and $\mathbf{C}$ is the matrix containing the $L \times L$ expansion coefficients.

Physically correct basis functions in the form of Slater-type orbitals (with an e^{-r} dependence) can be approximated by linear combinations of multiple Gaussian functions (with an e^{-r^2} dependence). The basis sets used in the subsequent work are exclusively of the split valence form following the Pople notation X-YZg, where X is the number of Gaussians used for the 1s orbital, Y for the inner 2s and 2p orbitals and Z for the outer 2s and 2p orbitals. Additional polarisation functions that allow for higher angular flexibility are denoted with *, while extra diffuse functions which contain very small orbital exponents are denoted with + symbols. For example, the basis set 6-31+G* contains 6 Gaussians for 1s, 3 Gaussians for the inner 2s and 2p, 1 Gaussian for the outer 2s and 2p orbitals, d functions on heavy atoms and a set of diffuse s and p functions on heavy atoms.

2.2.2 Density functional theory

The Hohenberg-Kohn and Kohn-Sham equations

The primary limitation of the wavefunction based approaches to computational chemistry, discussed above, is the huge increase in computational expense with the size of the system being studied. The wave function is a function in $3N$ dimensions for N electrons (with an additional variable of spin for each electron), and so the computational requirements for accurate calculations involving systems with applicability to nanoscience soon become infeasible. Density functional theory (DFT) is based on the principle that the electron density can uniquely determine the total energy of the system and so can reduce this $3N$ dimensional problem to one simply involving the three dimensions of electron density, regardless of the system size. This was proven to be the case in 1964 with the first Hohenberg-Kohn theorem,[55] while the second Hohenberg-Kohn theorem demonstrated that the functional that gives the ground state energy only produces the lowest energy when the density is the true ground state density. This means that DFT is variational; the electron density that minimises the energy of the system is the most accurate one.

The Kohn-Sham (KS) approach[56] is essentially the DFT equivalent of the HF approximation; the real system of N interacting particles is replaced with a system of N non-interacting particles moving in an effective potential $V_s(r)$. This potential must be chosen such that the electron density ρ constructed from the

KS orbitals exactly equals the real density of the interacting system. The total electronic energy contains contributions from the electron-electron interactions, the nucleus-electron interactions and the electron kinetic energy, as before:

$$E[\rho] = E_{ee}[\rho] + E_{ne}[\rho] + T_e[\rho] \tag{2.34}$$

The electron kinetic energy T_e of the non-interacting system can be calculated exactly (T_S), and differs from the kinetic energy of the true interacting system by T_C, while the electron-electron term can be split into contributions from the known classical Coulomb part J and the non-classical contributions of exchange and correlation E_{ncl}. The electron correlation is the error introduced by the HF approximation - as each electron in HF theory only interacts with the average potential of all the other electrons, the electrons tend to get too close to one another. The total energy is then given by

$$E[\rho] = J[\rho]+E_{ne}[\rho]+T_S[\rho]+T_C[\rho]+E_{ncl}[\rho] = J[\rho]+E_{ne}[\rho]+T_S[\rho]+E_{XC}[\rho] \tag{2.35}$$

with the unknown terms grouped into the exchange-correlation functional E_{XC}.

Exchange-correlation functionals

If all the terms in Equation 2.35 were known exactly, the energy calculated would be the exact ground state energy. However, as the exact form of the exchange-correlation functional is unknown, an approximation must always be made. The first approximation to the form of the functional is the local density approximation (LDA). In the LDA the value of the exchange-correlation functional is simply the exchange-correlation energy E_{xc} of a homogeneous electron gas with the same total electron density $\rho(\mathbf{r})$.

$$E_{XC}^{LDA}[\rho(\mathbf{r})] = \int \rho(\mathbf{r})\epsilon_{XC}(\rho(\mathbf{r}))d\mathbf{r} \tag{2.36}$$

The exchange-correlation energy of a particle in this uniform electron gas, ϵ_{XC}, can be split into exchange and correlation contributions. The exchange part E_X is known to be the Slater exchange

$$E_X = \frac{3}{4}\sqrt[3]{\frac{3\rho(\mathbf{r})}{\pi}} \tag{2.37}$$

The exact form of the correlation energy E_C is unknown and was initially found using quantum Monte Carlo calculations,[57] followed by the development of several analytical methods derived from these results. The most widely used of these include the 1980 Vosko-Wilk-Nusair functional (VWN)[58] and the 1992 Perdew-Wang functional (PW92).[59]

The generalised gradient approximation (GGA) is the first logical improvement to the LDA. In addition to using the electron density $\rho(\mathbf{r})$, information about the gradient of electron density $\nabla\rho(\mathbf{r})$ is used to account for the non-uniformity of real systems.

$$E_{XC}^{GGA}[\rho(\mathbf{r})] = \int \rho(\mathbf{r})\epsilon_{XC}(\rho(\mathbf{r})), \nabla\rho) d\mathbf{r} \tag{2.38}$$

The exchange part of this can be written as

$$E_X^{GGA} = E_X^{LDA} - \sum_\sigma \int F(s_\sigma)\rho_\sigma^{\frac{4}{3}}(\mathbf{r}) d\mathbf{r} \tag{2.39}$$

in which s_σ is the reduced density gradient of spin σ

$$s_\sigma(\mathbf{r}) = \frac{|\nabla\rho_\sigma(\mathbf{r})|}{\rho_\sigma^{\frac{4}{3}}(\mathbf{r})} \tag{2.40}$$

F is a function of s_σ that depends on the exchange functional used. By far the most commonly used exchange functional of this type is Becke (B) exchange,[60] where

$$F = \frac{\beta s_\sigma^2}{1 + 6\beta s_\sigma \sinh^{-1} s_\sigma} \tag{2.41}$$

β has been empirically determined to be 0.0042. Common correlation functionals include the Lee-Yang-Parr (LYP),[61] the 1991 Perdew-Wang (PW91)[62] and 1986 Perdew (P86)[63] functionals.

While the LDA and GGA are reasonable for periodic solids, and are commonly used for computational studies of graphene, they perform poorly for molecular species such as the ones examined in Chapter 3, giving at best only qualitative trends. In the HF method the exchange energy can be calculated exactly, and including a degree of this in E_{XC} can greatly improve the accuracy of calculations in these systems. The energy of the HF exchange functional E_X^{HF} is calculated from the KS orbitals and then combined linearly with density functionals for the exchange and correlation. The most commonly used hybrid functional, B3LYP, uses the Becke 3-parameter (B3) exchange[64] with the LYP correlation functional

$$E_{XC}^{B3LYP} = (1 - a_0)E_X^{LDA} + a_0 E_X^{HF} + a_X E_X^{B88} + a_C E_C^{LYP} + (1 - a_C)E_C^{VWN} \tag{2.42}$$

The empirical parameters a_0, a_X and a_C were fitted to experimental data and determined to be 0.20, 0.72 and 0.81 respectively.

DFT molecular dynamics

The forces acting upon the nuclei can be calculated by computing the gradient of the energy. By inserting these forces into the classical Newtonian equations of motion, the trajectories of the atoms through space can be propagated through time. Discretising time into a series of short time-steps allows for a full electronic relaxation and recalculation of the forces after each short propagation of the nuclei, corresponding to molecular dynamics on the Born-Oppenheimer potential energy surface (when the length of the time-step is sufficiently short).

The positions of the nuclei only change by a small amount in each time-step, and therefore the ground electronic state is typically also very similar in any two consecutive time-steps. This fact can be taken advantage of in order to accelerate DFT-MD calculations, by using information about the electronic configuration of the previous step to inform the initial guess of the current one; the converged Fock matrix **F** (in Equation 2.33) of the previous step can be used rather than constructing a new one. As the nuclear motion and therefore electronic change is gradual over several steps, the change in the Fock matrix over multiple previous time-steps can be extrapolated to construct a better initial guess for the current step.[65] This can drastically speed up calculation time (typically by a factor of two) by both eliminating the costly initial Fock matrix construction and by reducing the required number of SCF cycles. The latter allows very tight SCF convergence criteria to be set, eliminating the accumulation of systematic error which can cause a drift in the system energy over time.

In practice, for the DFT-MD calculations discussed, the Q-Chem electronic structure package[66] was used, with a Fock matrix extrapolation procedure fitting the preceding 12 Fock matrices to a 6^{th}-order polynomial, a tight SCF convergence criterion of 10^{-6} E_h, and a threshold for the neglect of two electron integrals of 10^{-9}. A time-step of 1 femtosecond was used, apart from in Section 3.3 in which the transfer of large kinetic energies to low-mass atoms (hydrogen and deuterium) rendered this unsuitable for obtaining quantitatively correct threshold energies. In this case, a timestep of 0.5 fs was used, which is sufficiently short as to replicate results obtained using a 0.1 fs timestep. Unless otherwise stated, the B3LYP/6-31G level of theory was used (with results checked against B3LYP/6-31G*), although in sections 3.4 and 3.5 the 6-31G* basis set was used, as discussed in the relevant sections.

Threshold energy calculations

As discussed in Section 2.1, the threshold energy of an irradiation-induced process is the minimum energy that must be transferred from an incident electron to an atom in order for the process to take place without immediate reversal. Although this can in principle be determined by experiment due to the development of atomic resolution microscopy, currently there are few examples of experimentally determined thresholds.[52] The threshold energy of a process of interest is therefore usually obtained computationally, *via* a series of MD simulations. At the beginning of each simulation, a kinetic energy corresponding to the energy transferred from the incident electron is assigned to the PKA. The structural evolution of the entire system over time is then computed using MD in order to determine whether or not the process occurs. This is repeated over a range of initial kinetic energies in order to determine the threshold energy, until it is known to lie between two energies within the desired accuracy, typically $\pm$ 0.1 eV for the following work. The binary search algorithm has previously been used[23] to choose the value of kinetic energy to apply in order to determine the threshold energy. However, if the computational cost of an individual MD simulation is high while the number of threshold energies to be determined is low (for example when calculating a single

threshold energy at a very high level of theory), manual inspection of the MD trajectories and estimation of a suitable kinetic energy based on the results can be more efficient, and has been used in the work discussed in this thesis.

In practice, the geometry of each system discussed was optimised, followed by a DFT-MD run with the initial atomic trajectories sampled from a 298 K Maxwell-Boltzmann distribution. As the interaction time of a relativistic electron with a nucleus is much shorter than the time-step used, the velocity of the PKA was simply edited to correspond to the considered energy transfer under the beam. The system was evolved through time until the process of interest either occurred or the transferred energy had been distributed through the molecule to the degree that the impact would clearly not lead to a reaction. Most reactions occurred in significantly under 100 fs and almost all in under 200 fs, with the time required increasing with proximity to the threshold energy.

2.3 Multislice image simulations

The atomic coordinates that result from computational studies of a material, for example *via* geometry optimisations or by molecular dynamics simulations, can be compared to experimental results by using them to simulate TEM images. This is an extremely powerful method that allows direct and quantitative comparisons, although it could be argued that it is more important for three dimensional systems in which incident electrons will be scattered multiple times, resulting in images that can not be directly compared to the atomic structure.

As the vast majority of electrons passing through the sample will only be scattered through a very small angle, any transfer of momentum can be neglected and the effect of the sample on the incident electron beam can be considered to be limited to the elastic scattering caused by a static Coulombic crystal potential. In order to determine the effect of the crystal potential on the incident electron beam, the Schrödinger equation for the electron must be solved[iv]. This is most commonly achieved with the multislice approach, in which the wavefunction of the incident electron is represented by a modulated plane wave normal to the crystal surface, scattered by the 3D crystal potential. This results in a first order differential equation in terms of the thickness of the sample, which can be numerically integrated by approximating the 3D crystal potential with a large number of 2D potentials;[68] the sample is effectively 'sliced' parallel to its surface (perpendicular to the beam). The 3D potential over the thickness of each slice is projected onto a 2D surface for that slice. The scattering of the incident wave is transmitted through a single 2D potential, being kinematically scattered by it, and is then propagated through vacuum for the width of the slice. Repeating over all slices, the result is the wavefunction of the electron at the crystal exit surface, and increasing the number of slices tends to the exact solution.

In order to produce an image from the exit face wavefunction it is convo-

[iv] Although the Schrödinger equation is not relativistic, and to correctly include relativistic effects the Dirac equation should be used, at the energies typically used in TEM it is sufficient to use the Schrödinger equation with relativistic masses and wavelengths for the electron.[67]

luted with the microscope transfer function (CTF), which contains the aberration effects of the lenses. The effects of chromatic aberration can be calculated by repeating the image formation over a Gaussian spread of incident beam energies and averaging the results, or in practice for TEM by introducing an analytical damping factor to the CTF (which also includes the effects of partial spatial coherence).[69] The thermal vibrations of the atoms can be taken into account using the frozen phonon approach,[70] in which the incident electron sees a single snapshot of the molecular vibrations. The calculation is therefore iterated over a set of such snapshots (20 in the image simulations described here), where each has different small atomic displacements. This is considered important in order to accurately reproduce areas such as the the loosely-bound fragments observed during the structural evolution of heterofullerenes in Section 2.3.1, for which weakly connected fragments that can undergo quick conformational changes and anisotropic vibrations exist.[71] After averaging these images, the noise introduced by using a finite electron dose can be applied. The intensity of each pixel in the final image is a Poisson-distributed random deviation of the uniform electron dose per pixel, weighted by the pixel intensity resulting from the multislice simulation. Finally, the experimentally measured modulation transfer function (MTF) of a CCD camera[72] at the accelerating voltage used is applied in order to obtain an accurate signal to noise ratio.

The multislice implementation in the QSTEM software suite[69] is used in Section 4.2 in order to help explain the appearance in TEM of a dynamic vacancy defect in graphene, and two brief examples of this kind of image simulation in other materials are given in the following two sections.

2.3.1 Formation of nickel-carbon heterofullerenes

The computational modelling of the effects of electron irradiation on graphene flakes with small nickel clusters using the CompuTEM method[71,73] demonstrated the formation of nickel-carbon heterofullerenes.[74] Snapshots of the molecular structures taken from the MD simulations were used to produce TEM image simulations, shown in Figure 2.6. The electron dose per image used was 4.1×10^6 $e^-/nm^2/s$, corresponding to the dose rate used for the CompuTEM simulations, while the the spherical aberration was 20 μm and the defocus set to 5 nm, with a focus spread of 1.9 nm.

2.3.2 h-BN domes

Experimentally observed features grown in hexagonal boron nitride (h-BN) were attributed to large dome-like structures,[v] viewed at different angles due to their positions on step edges of the h-BN. Multislice image simulations were performed for this structure, shown in Figure 2.7, at a variety of angles (0, 30, 50 and 70°) relative to the plane of the beam. The simulation parameters were chosen to match the experimental settings used: accelerating voltage = 200 kV, C_s = 0.1 mm, defocus = -65 nm, resolution = 1 Å/pixel, dose = 10^4 e^-/nm^2.

[v]Paper submitted for publication.

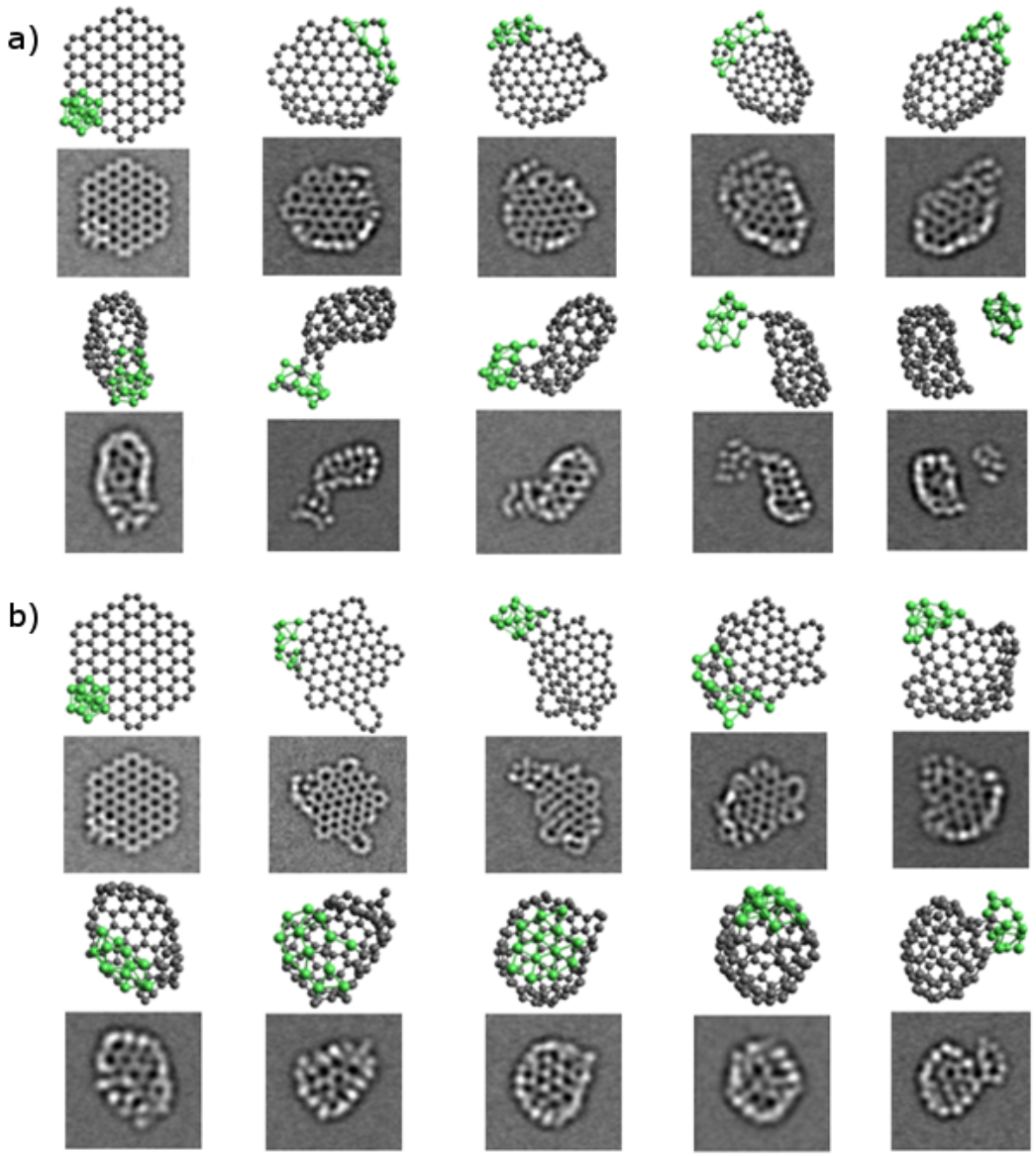


Figure 2.6: The molecular structures taken from two MD simulations (a and b) of the transformation of graphene flakes to heterofullerenes, and the corresponding multislice image simulations. In (a), the nickel cluster is bound to the edge of the flake, a fullerene quickly forms, and the cluster detaches. In (b), the nickel cluster is incorporated into the structure of the forming fullerene, and therefore remains attached for a much longer time.

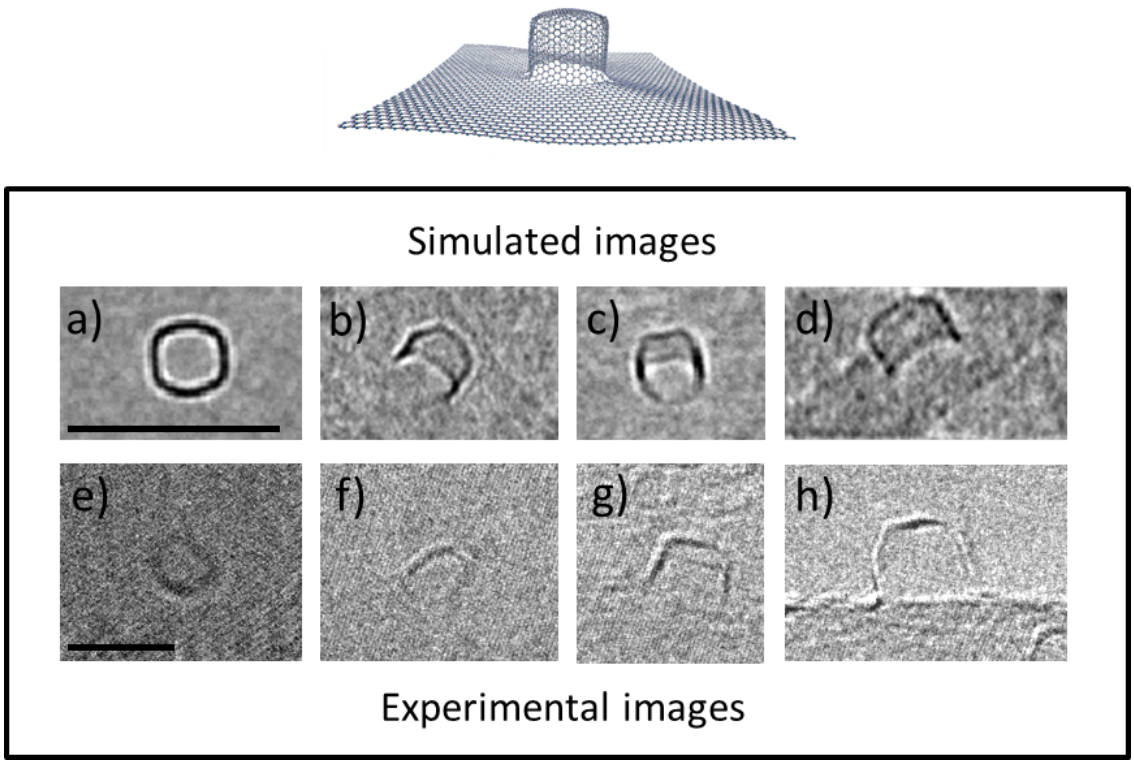


Figure 2.7: Simulated TEM images (a-d) of the h-BN dome-like nanostructure shown above, corresponding to incident beam directions of (a) 0, (b-c) 30 and (d) 50 with respect to the h-BN plane. Experimentally observed features (e-h) for comparison with the simulations. Scale bars are 10 nm, and are the same for all images in each row.

Chapter 3

Reactions of nanotube-encapsulated molecules in TEM

As discussed in Section 1.2.2, the encapsulation of molecules inside SWNTs generally provides protection from the effects of e-beam damage, resulting in lifetimes that are typically two orders of magnitude larger than in crystal structures. A wide variety of e-beam induced reactions of these molecules are possible, ranging from simple destruction into atomic fragments and subsequent reformation into larger structures, to the direct polymerisation of the precursor molecules into graphene ribbons.

In general, the presence and nature of any heteroatoms in the encapsulated molecules' structure determines the nature of their reactions under the electron beam. Simple carbon containing molecules such as fullerenes are broken up into atomic (C_2) fragments, which can then reform to create an inner guest nanotube - the thermodynamically most stable structure.[75] The introduction of heteroatoms provides a way for edges of the forming graphene nanoribbons to be terminated, saturating the undercoordinated dangling bonds and increasing the thermodynamic stability of a guest nanoribbon over that of a guest nanotube. The resulting products do not depend on the exact structure or composition of the precursor molecules, but on the width of the host nanotube, demonstrating that the pathway is likely disintegration followed by reformation. In these cases, the electron beam simply provides energy to the system, enabling the destruction of the precursor molecules. Further evidence of this lies in the fact that both of these general trends can also be seen under very high heating conditions (1000 °C), where the reactions are thermally driven rather than initiated by an electron beam. This is in contrast to reactions of similar organic molecules under more moderate heating (400-500 °C), where polymerisation of the precursor molecules forms nanoribbons.[76] These nanoribbons, rather than being 'perfect' ribbons of uniform width, display features of their precursor molecules; their exact structure is dependent on the nature of the polymerisation reaction.

If the encapsulated molecules are chosen with the electron beam in mind, species can be designed that are stable with respect to total disintegration into

atomic fragments. Again, heteroatoms provide an efficient method for accomplishing this - elements with higher masses are less easily ejected from the molecule by the electron beam, and so can in principle be used for protection against the beam. Beam induced polymerisation reactions can then be used to create nanoribbons, in a similar manner to the thermally induced reactions mentioned above but with two key advantages: 1) a direct knock-on collision from an incident electron is a rare event, and dependence on them greatly slows the rate of the reaction, allowing it to be followed on TEM-accessible timescales; and 2) the unique nature of the transfer of energy from the electron beam can be taken advantage of in order to drive otherwise infeasible chemical reactions - it is elementally specific, direction specific, and in principle the rate of different competing reactions can be tuned with careful selection of the accelerating voltage, allowing for more precise control than achievable with heating.

In Section 3.2, the effect of the electron beam on the edge termination of growing nanoribbons, and its determination of the product formed when a variety of heteroatoms are available, will be examined. Based on these results, Section 3.3 will investigate how isotopic substitution can be used to increase the stability of organic molecules in TEM. Finally, in sections 3.4 and 3.5 the e-beam induced mechanisms of polymerisation for two organic molecules containing heavy heteroatoms are explored.

3.1 Nanotube exclusion in E_d simulations

In order to perform DFT-MD simulations without incurring considerable computational expense, the calculations used to obtain threshold energies in the following sections have not explicitly included the nanotube in which the molecule is encapsulated, but have been performed for a single molecule in the gas phase. As this is the largest approximation made it will almost certainly be the largest source of any discrepancy between experimental and computational observations, and so it is worth briefly considering the possible consequences this will have on the calculated cross-sections of these processes.

The most obvious and immediate assumption is that the presence of the nanotube wall will have the effect of raising the threshold energy of any processes, protecting the molecules from the effects of knock-on damage in a similar manner to layering multiple 2D materials on top of one another.[24,77] This would inhibit the rate of the reaction by lowering the cross-sections of the process, implying that the computational cross-sections will be overestimated, especially considering the effect of the isotropic approximation of the threshold energy. More subtly, it is possible that the actual threshold energies of processes such as emission remain very similar in the gas phase and in the tube, but that the encapsulation effectively increases the rate of recombination; the nanotube wall will trap emitted atoms and therefore increase their relative local concentration.

On the other hand, the threshold energy could actually decrease due to the nanotube. Catalytic processes involving the nanotube wall could occur, similar to ones shown to exist in bilayer graphene.[78] Additionally, the proximity of the

nanotube wall could actually lower the threshold energy by weakening the bonds between carbon and terminating atoms, by acting as an attractive surface (*via* dispersion effects) for the emitting atom compared to the vacuum.

Although using computationally cheaper methods such as DFTB or classical molecular dynamics would allow the nanotube (and even the molecular stacks) to be included in the simulations, qualitatively incorrect behaviour is predicted in cases where these methods incorrectly describe atom emission.[16,49,51] Although the above considerations are likely to affect the exact value of any thresholds calculated in the present chapter, they are unlikely to significantly affect the general conclusions and behaviour of the species under the beam. It is more important to have a complete and correct description of the chemical bonds being broken, by using explicit all-electron calculations such as DFT, than to sacrifice this accuracy in order to explicitly model the molecule's surrounding environment.

3.2 Sulphur-terminated graphene nanoribbons

In 2011, Chuvilin *et al.*[79] demonstrated the self-assembly of a sulphur-terminated graphene nanoribbon inside a single-walled carbon nanotube. By irradiating heteroatom-containing molecules encapsulated in a SWNT, a mix of small carbon fragments and elemental sulphur, nitrogen, oxygen and hydrogen is formed inside the nanotube. Although hydrogen would perhaps be considered the most likely candidate for termination of the nanoribbon edges, and hydrogen-terminated nanoribbons had previously been synthesised,[76] the exclusive formation of sulphur-terminated nanoribbons was observed.

3.2.1 Simulations

In order to understand the preferential termination of the nanoribbons with sulphur rather than the other readily available heteroatoms, the threshold energies have been calculated for the emission of sulphur, hydrogen and carbon atoms terminating the nanoribbon edge, as detailed in Section 2.2. The short nanoribbon structure shown in Figure 3.1 was used, with the central circled atoms chosen as the representative PKA for each element. The same nanoribbon structure (including the terminating hydrogen atoms) was used for the simulations of the carbon atom emission, as it has been shown that the presence of terminating hydrogen atoms has a negligible effect on the threshold energy for emission of edge carbon atoms in nanoribbons.[16] During the hydrogen displacement simulations the disruption to the structure of the nanoribbon was localised to a small area. However, during the sulphur and carbon atom displacement simulations the structure disruption extended to the ends of the short nanoribbon model. To more closely resemble the infinite nanoribbon without incurring unreasonably high computational expense, the carbon atoms at the two ends of the nanoribbon were fixed in place by assigning them arbitrarily high masses.

Although there is no reason for the nanoribbons to prefer a particular orientation in the tube with respect to the beam, the vast majority of the published

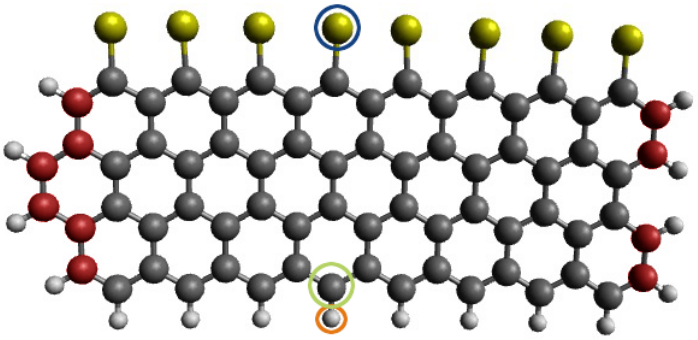


Figure 3.1: The nanoribbon model used, with the PKA for sulphur, carbon and hydrogen circled in blue, green and orange, respectively. The fixed carbon atoms are highlighted in red.

experimental TEM images[79,80] show ribbons that are mostly (if not entirely) oriented face-on to the beam. This can be accounted to a form of publication bias: only the images in which the ribbons are face-on and can therefore be characterised are included in the discussion of the nanoribbon's structure. As mentioned previously (in Section 1.2.2), the orientation of structures with respect to the beam can have a large impact on the damage that they are susceptible to, and so it is not entirely infeasible that the nanoribbon structure, especially the edge termination, could be different in face-on and edge-on cases. Considering this, the threshold energies were calculated for the direction normal to the plane of the ribbon in order to more closely match the reported structures and conditions.

The calculated emission threshold energies are given in Table 3.1, together with the maximum energy transferable to each atom and the resulting emission cross-section at the experimentally used 80 kV accelerating voltage. The emission cross-sections σ_d were calculated using these threshold energies (according to Equation 2.11) as a function of the accelerating voltage, and are shown in Figure 3.2. The contributions of lattice vibrations were calculated using the Maxwell-Boltzmann velocity distribution.

Atom	$\mathbf{E_d}$ **(eV)**	$\mathbf{T_{max}}$ **(eV)**	$\sigma_\mathbf{d}$ **(barn)**
Hydrogen	7.4 ± 0.1	187.8	69.15
Sulphur	11.5 ± 0.1	5.9	0
Carbon	16.5 ± 0.1	15.8	0.53

Table 3.1: The calculated threshold energies for emission of the terminating atoms of the graphene nanoribbon (E_d), the maximum energy that can be transferred to a stationary atom for each element (T_{max}), and the corresponding emission cross-sections (σ_d) at 80 kV. For carbon, although E_d is larger than T_{max}, the contribution of thermal vibrations ensures that σ_d is non-zero.

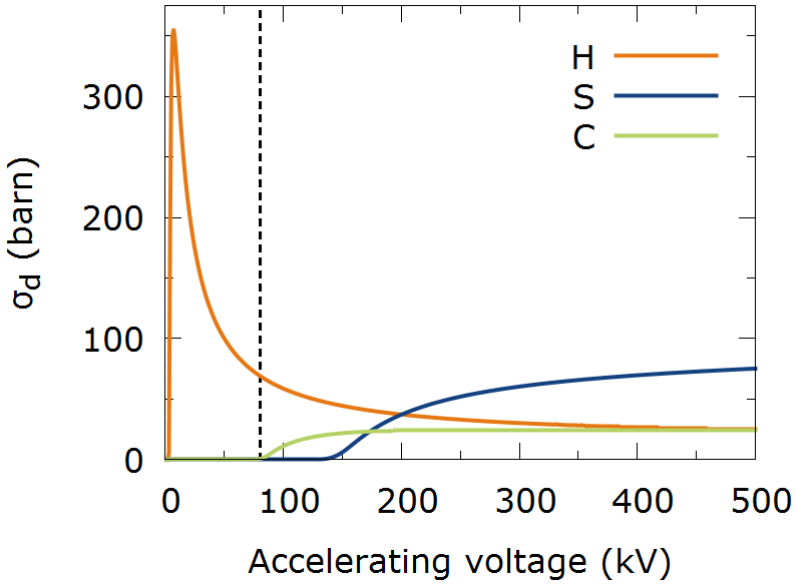


Figure 3.2: Calculated displacement cross-sections σ_d (in barn) as functions of electron kinetic energy E (in kV) for hydrogen (thick red line), carbon (green line), and sulphur (thin blue line) atoms circled in Figure 3.1.

3.2.2 Discussion

Although the emission threshold for carbon (16.5 eV) is in broad agreement with previous calculations for emission from the edges of graphene nanoribbons,[16] it is significantly larger (by approximately 1.5 eV) than the previous result for the equivalent zig-zag (ZZ) edge for a ribbon that is three hexagon rows wide. The most likely reason for this lies in the differences between the DFT used here and the density functional tight-binding (DFTB) method used previously. There was a large discrepancy of approximately 2.5 eV between identical simulations using the two methods when calculating the threshold energy of emission from a ZZ edge, suggesting that DFTB does not adequately treat ZZ edges.[16] DFTB is also known to poorly predict emission thresholds in h-BN,[28] when compared to both DFT and experiment.[51] Another possibility is that the presence of sulphur atoms on the other side of the ribbon have an influence.

At lower energies (<100 kV) the cross-section for hydrogen is extremely large relative to those of carbon and sulphur, rising to a peak of 355 barn at 7 kV. At an accelerating voltage of 80 kV, corresponding to experimental conditions,[79] it can be seen that while sulphur will undergo no emission from the nanoribbon, the displacement cross-section of hydrogen is very large. This difference in the sulphur and hydrogen atom displacement cross-sections explains the preferential sulphur termination of nanoribbons observed at low accelerating voltages. Once a sulphur atom bonds to the edge of the nanoribbon it is effectively 'stuck' in position with no available mechanism for removal, while hydrogen will be easily removed, and so over time the nanoribbon will tend towards the S-terminated structure. The

rate of atom emission under an 80 kV electron beam can be estimated from the cross-section. The expected lifetime of a terminating hydrogen atom once bonded to the edge can be calculated as the inverse of the product of the cross-section and the electron dose rate (or electron flux); for the experimentally used[80] range of 10^6 to 10^7 $e^-/nm^2/s$ this is equal to an approximate lifetime of somewhere between 14 seconds and two minutes, which is reduced to only 3 - 30 seconds at 7 kV.

At higher accelerating voltages, sulphur (at 200 kV) and eventually carbon have larger cross-sections than hydrogen, meaning that hydrogen will counter-intuitively have the lowest probability of the three atoms of displacement from the nanoribbon edge. In 2015, an experimental TEM study on hydrogenated MoS_2[81] used this result in order to slow the rate of hydrogen emission below that of sulphur by imaging with a 200 kV electron beam, enabling the successful structural characterisation of the material. It can be proposed that a hydrogen-terminated graphene nanoribbon can form instead of a sulphur-terminated nanoribbon, using the same precursor material but at a higher accelerating voltage, although under these conditions (>80 kV) there would also be significant damage caused to the forming nanoribbon. The possibility of different chemical reactions occurring under electron irradiation in identical conditions other than the electron kinetic energy suggests that electron irradiation could be used for the selective control of chemical reactions, an idea that will be re-examined in Section 3.4.

The decrease in cross-sections at high accelerating voltages, seen most strikingly in the case of hydrogen atoms, can be understood by considering the length of the interaction time between the electron and the nucleus. As the electron kinetic energy increases, the time spent in close proximity to the atom decreases; β (the electron velocity as a fraction of the speed of light) tends to one. As can be seen by Equation 2.11 or 2.2, this reduces the cross-section, counteracting the increase in cross-section due to a larger transferred energy. At a certain accelerating voltage, the effect of the increase in β outweighs the increase in the transferred energy, reducing the cross-section.

Although the values for E_d differ depending on the precise structure of the molecule, small changes in E_d do not change the general trends shown in Figure 3.2. In addition, the differences in cross-sections between atoms of different elements is generally much larger than the differences between atoms of the same element in different environments. This is because although different environments can alter E_d, atoms of different elements also have large differences in T_{max} - as Z increases, the energy transferred to the atom decreases as shown in Figure 2.3. This means that while different molecules or nanostructures will have slight differences in the dependence of the cross-section on the accelerating voltage, Figure 3.2 can be taken as a rough estimate of the general case.

The overlap of the carbon and hydrogen cross-sections has important implications for organic and biological TEM. In addition to the much higher levels of irradiation damage caused to these molecules by inelastic electron collisions, Figure 3.2 shows that there is no accelerating voltage above approximately 5 kV at which predominantly carbon- and hydrogen-containing molecules will be indefinitely stable under TEM irradiation. Caution must be taken when interpreting the low energy region of these cross-sections (below 10 kV) due to approxima-

tions made in the thermal lattice contribution (see Section 2.1.5). In this case, a comparison of using the Maxwell-Boltzmann distribution and simply considering a static lattice shows very little difference: the transmitted energy to hydrogen increases so quickly with increasing incident electron energy that the thermal lattice plays a very small role in the accelerating voltage dependence of the emission rate, and so these results can be taken as broadly accurate. However, although this suggests that future developments of very low energy TEM might push past the region of high knock-on damage to organics into an energetic region of vastly increased stability, the exceptionally large rise in cross-sections of inelastic processes when moving to these energies[46] means that the effect of these processes on atomic structure would need to be entirely quenched before observing any increase in atomic stability. Although this consideration would seem to be mostly academic, as no current TEM can provide such high resolution at these accelerating voltages,[i] the push towards atomic resolution imaging at lower energies has made fantastic progress in just the last few years; while aberration correction TEM was typically limited to 80 kV and above, comparable resolution can now be achieved as low as 20 kV.

3.3 Deuteration of organic species in TEM

Stacks of organic molecules in nanotubes are typically stable, as discussed, but in general are seen to decompose very quickly in TEM, normally to form inner nanotubes or graphene nanoribbons. Given the high cross-sections of hydrogen emission relative to that of carbon, it is sensible to assume that the destruction or reactions of these molecules are initiated by hydrogen emission, which will create highly reactive species. Slowing this initiating step should reduce the rate of molecular destruction, and allow the encapsulated species to be imaged for longer.

Considering the results in the previous section, from Table 3.1 it is clear that although the emission threshold energy of hydrogen is lower than other elements and plays a large role in the low irradiation stability of C-H bonds,[ii] the main factor is the very large amount of energy that can be transferred to a hydrogen atom from an incident electron (188 eV at 80 kV) due to the low mass of hydrogen. In principle, replacing hydrogen atoms in organic materials with other, heavier elements would limit this damage, but it would also completely change the chemistry of the materials being studied, which makes it a poor general method for increasing stability (and is tantamount to simply saying 'go and study something else'!).

The same kind of increase in stability should be achievable without altering the chemistry by substituting atoms in encapsulated organic molecules with heavier isotopes. Isotopic substitution of ^{12}C with ^{13}C has been demonstrated to reduce

[i] In TEM the contrast increases with decreasing accelerating voltage, but chromatic aberrations make the achievable resolution very poor without aberration correction.

[ii] With an emission threshold energy equal to that of carbon (16.5 eV), the emission cross-section for hydrogen would be limited to under 100 barn at all accelerating voltages.

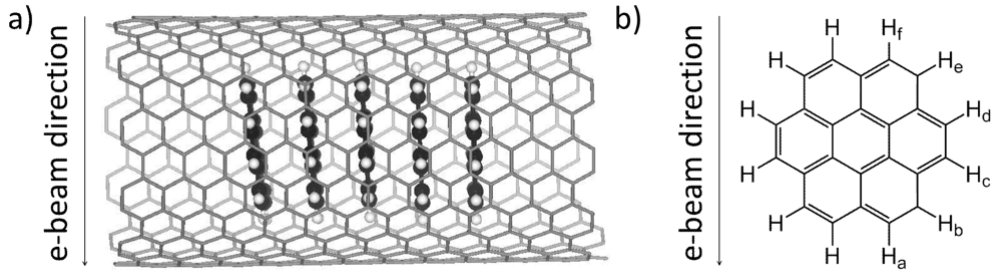


Figure 3.3: Coronene molecules stacked within a SWNT (a), which results in six non-equivalent C-H bonds with respect to the electron beam (b). Adapted from reference 37.

the emission cross-section in graphene both theoretically and experimentally,[52] which can be seen in Figure 2.5 in Section 2.1.4. Although this had a significant impact on the precise energy of the onset of knock-on damage at low accelerating voltages, the effect on the overall cross-section is relatively minor as this only corresponds to an increase in the atomic mass of carbon by 8% (reducing T_{max} from 15.8 eV to 14.6 eV at 80 kV). In contrast, replacing protium (^{1}H) with deuterium (^{2}H or D) doubles the atomic mass. At 80 kV this halves T_{max} from 188 eV to 94 eV, which should result in a considerable increase in the stability of carbon-hydrogen bonds, while leaving molecular structure and chemical properties mostly untouched. Practically speaking, as deuteration simply requires treating most organic molecules with heavy water (D_2O) prior to nanotube encapsulation, isotope exchange should provide a simple and fairly universal method for stabilising them for TEM imaging.

3.3.1 Coronene

Coronene, shown in Figure 3.3, is the ideal molecule to study the effect of deuteration in more detail theoretically and experimentally. The molecule is relatively small, making computational studies remain feasible, and it has been extremely well studied in TEM.[76,82–84] Coronene is readily encapsulated inside carbon nanotubes, but it is observed to decompose almost instantly upon electron irradiation at energies of 80-120 kV.

It would be very computationally demanding to fully characterise the emission cross-sections of all six inequivalent hydrogen atoms in coronene, especially considering that the isotropic approximation would not be valid for most of them. The important comparison to experimental observations is the relative stability increase conferred upon the molecules by deuteration, rather than the absolute rates of destruction of coronene or deuterated coronene (d-coronene). This can be accomplished by comparing emission cross-sections of protium and deuterium from the hydrogen position most susceptible to irradiation induced emission, and approximating that the damage will start with this most accessible emission. Note that this is not the **weakest** bond, as all bonds remain equivalent in terms of bond

strength, but the bond which is in the most favourable orientation for emission relative to the beam direction.

There are two extreme orientations of coronene possible in the nanotube: the configuration shown in Figure 3.3 and this configuration rotated by 60° in the plane of the molecule. The most favourable case for emission is the one shown, where there are bonds parallel to the beam and the lowest emission threshold energy aligns with T_{max}. In this orientation, DFT-MD simulations in which the momentum is transferred at angles corresponding to T_{max} show that bond a has the lowest emission threshold energy, while bonds b to f have higher threshold energies. In the case of a the momentum from the electron beam is transferred directly along the axis of the bond and in the direction of emission, resulting in a lower value of E_d. As the molecules can be seen moving on irradiation timescales, it can be assumed that the molecule will be in this orientation at least some of the time, and that a simulation of atom emission in this orientation will therefore correspond to the most easily broken bond. The isotropic approximation of the cross-section will also be valid for this orientation, allowing emission cross-sections to be easily calculated.

As mentioned briefly in Section 2.2, the low mass of hydrogen atoms combined with the large kinetic energies transferred to them by the beam results in very quick atomic motion. These atomic velocities must be considered when choosing an appropriate timestep of the DFT-MD simulations; the use of an unsuitably long timestep will introduce unphysical artefacts into the dynamics and lead to errors in the threshold energies calculated. The 1 fs timestep, adequate for modelling impacts on heavier atoms, is too long for the simulations involving hydrogen and results in an error of 1 to 2 eV in the calculated value of E_d (and approximately a tenth of this for those involving deuterium). The atomic trajectories using a 0.5 fs timestep however are suitably converged to those observed with a 0.1 fs timestep - the error introduced is smaller than the difference between two MD simulations with different initial atomic velocities sampled from the Maxwell-Boltzmann distribution, even in the case of hydrogen. In order to obtain more accurate threshold energies to quantitatively estimate the effect of deuteration on the irradiation stability of coronene, timesteps of 0.5 fs have been used in DFT-MD simulations to calculate the emission threshold energies as described in Section 2.2.

The threshold energies for hydrogen and deuterium removal from the most easily broken bonds C-H_a and C-D_a are 7.7 eV and 7.9 eV respectively (± 0.1 eV). Figure 3.4 shows the cross-sections as a function of accelerating voltage, with the cross-section for emission of the attached carbon atom (E_d = 21.3 eV) as a point of reference. Halving the transferable energy and slightly increasing the emission threshold energy upon deuteration greatly reduces the cross-section at all accelerating voltages. This increase in stability is substantial: the likelihood of emission of hydrogen is more than four times that of deuterium at the maximum of the cross-section function, and at the commonly used accelerating voltages of 80-100 kV emission from coronene is 2.2 times more likely than from d-coronene. The electron dose or length of time before emission from one of these bonds will therefore also be improved by a factor of 2.2 upon deuteration. Deuterated coronene is predicted to be infinitely stable with respect to knock-on damage at accelerating

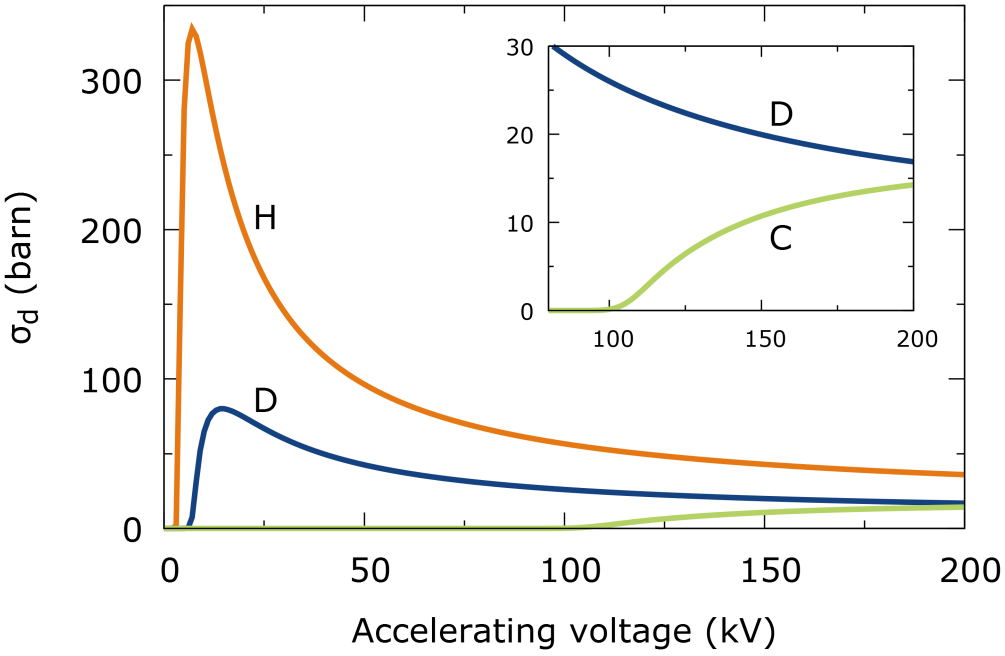


Figure 3.4: The emission cross-sections of of the most easily emitted hydrogen, deuterium and carbon atoms from coronene, as a function of accelerating voltage.

voltages below 6 kV.

It is interesting to consider the origin of the 0.2 eV increase in the emission threshold energy upon deuteration. One possibility is that this increase in bond stability can be attributed to the kinetic isotope effect (KIE). Increasing the mass of hydrogen decreases the zero-point energy of the bond, increasing the energy required to break it and therefore E_d. In principle this is the only change in the nature of the bond following deuteration, as the electronic structure and forces are identical in both cases. However, as the simulations are performed at room temperature (298 K) with the thermal state randomly populated from a Maxwell-Boltzmann distribution, it is not clear that the zero-point bond energy should play any direct role in the value of the threshold energy. Further, the magnitude of the difference would be expected to be lower than the 0.2 eV witnessed. An alternative more likely explanation is one that arises from the dynamical nature of the emission simulation. Upon an increase in mass from H to D, an atom with an identical kinetic energy must have a lower velocity. The emission process of this heavier atom therefore requires more time, and so it experiences the attractive forces of the remaining molecule for a greater length of time, retarding the emission and increasing the energy required for it to take place. This is another example highlighting the fundamentally dynamic nature of threshold energies E_d in contrast to simple static quantities such as thermal activation energies E_a, as discussed in the introduction.

Experimental TEM analysis of encapsulated coronene and d-coronene subsequently confirmed the general predictions made above.[37] While coronene was

observed to decompose almost immediately at 80 kV, d-coronene was much more stable, typically surviving for approximately twice the electron dose, as shown in Figure 3.5. The average dose required to destroy a molecular stack of coronene was 4.1×10^6 e^-/nm^2, compared to 7.4×10^6 e^-/nm^2 after deuteration. Because of this, d-coronene was able to be used to obtain more accurate measurements of the inter-molecular spacing within the stacks (0.39 ± 0.03 nm) and orientations of the molecules (79.8 ± 4.6°) than was possible with short-lived coronene (0.4 ± 0.1 nm and 83 ± 4° respectively).[37] The theoretically estimated increase in stability upon deuteration (2.2x) agrees well with experimental results based on both coronene molecules encapsulated in nanotubes (approximately 1.8x) and in solid crystal structures (2.4x).

3.4 Perchlorocoronene to nanoribbon transformation

As discussed in the previous section, replacing hydrogen in organic molecules with other, heavier elements should in principle protect them from damage from the electron beam. Just as deuteration approximately doubles the lifetime of these species primarily due to the doubling of atomic weight, replacing hydrogen with a heavier element will vastly increase the mass and should display a correspondingly large reduction in the rate of decomposition under irradiation. Although the chemistry of the molecules will be changed, the rate of reactions induced by the beam will be significantly slowed, to the point that they can be followed on TEM time-scales (approximately a second). The decrease in the amount of energy that can be transferred to the molecules also tends to result in stepwise reactions rather than the total destruction of molecules, similar to the difference between reactions observed under moderate and very high heating. This can allow for individual reaction steps to be seen and mechanistic understanding of the process to be gained.

The halogens in general present an obvious choice when replacing hydrogen in organic molecules with a heavier element, as they also have a valency of one. Perchlorocoronene (PCC) in particular is a sensible choice for continuing the series of encapsulated molecules, being essentially a coronene molecule with the hydrogen atoms replaced by chlorine. With an atomic mass of 35 Da (for the most abundant isotope), the energy that can be transferred to a stationary chlorine atom is limited to only 5.3 eV at 80 kV, and PCC has been shown to have one of the highest irradiation stabilities ever reported among organic crystals.[85] In the previous deuteration study[37] coronene crystals were amorphised after an electron dose of approximately 10^4 e^-/nm^2, while nanotube-encapsulated molecules survived a dose of 10^6 e^-/nm^2. PCC crystals have been shown to survive 10^6 e^-/nm^2,[85] while the encapsulated molecular stacks discussed in this section last for up to 10^8 e^-/nm^2.

Under electron irradiation at 80 kV, stacks of PCC can be seen to react, eventually forming a novel chlorine-terminated graphene nanoribbon, shown in Figure 3.6. As this is a relatively slow process, requiring approximately 8×10^8 e^-/nm^2,

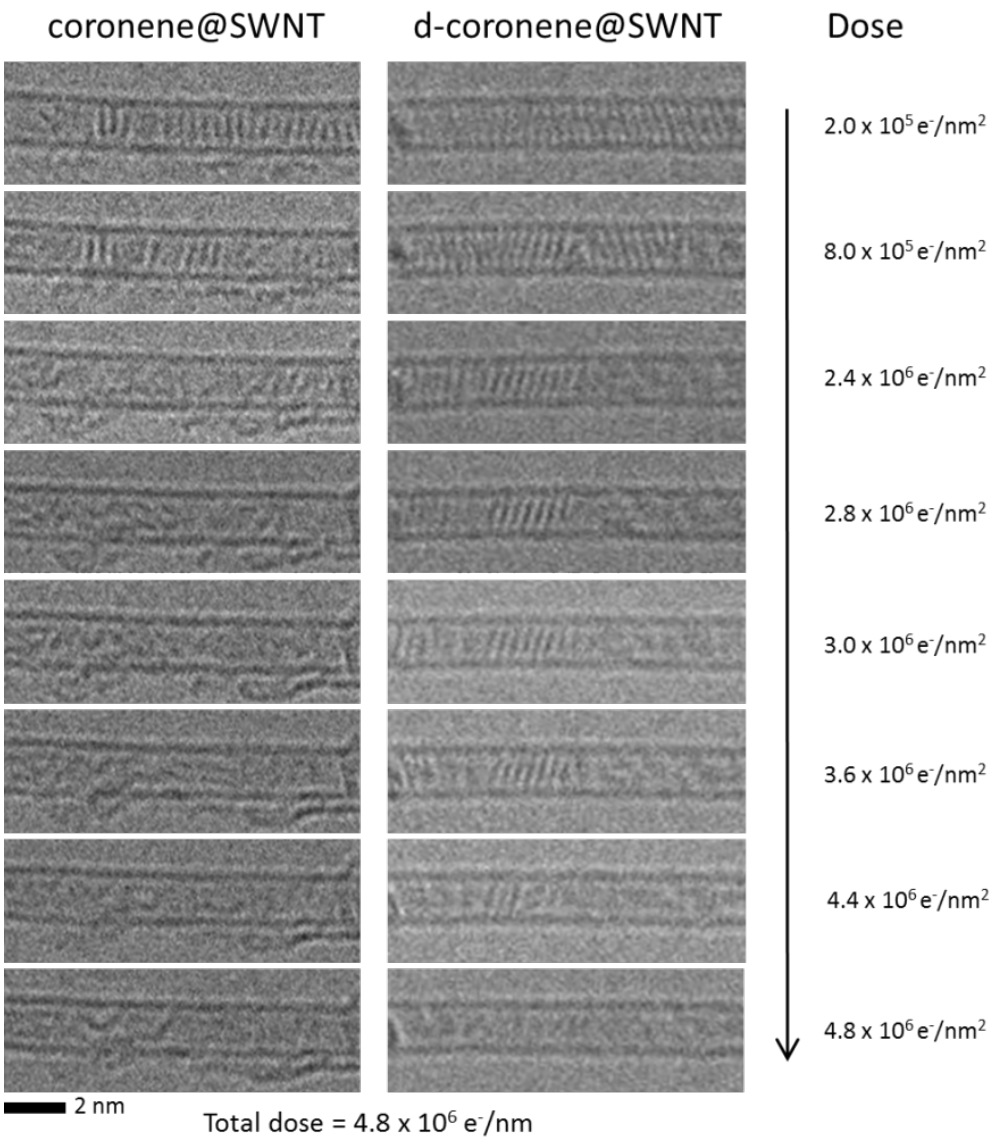


Figure 3.5: A comparison of the rate of destruction of stacks of coronene and deuterated coronene under 80 kV electron irradiation. Deuterated coronene survives considerably longer than coronene, in agreement with theoretical predictions. Reprinted from reference 37.

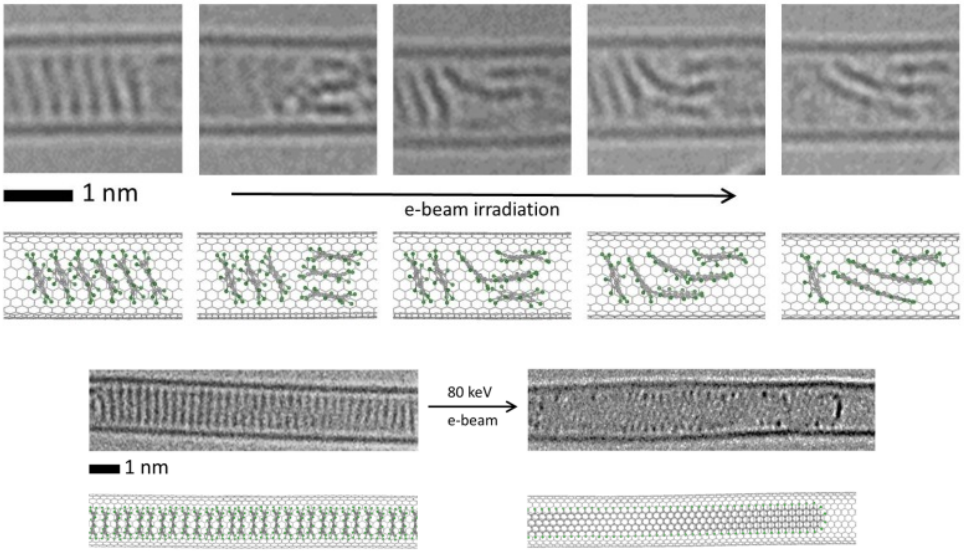


Figure 3.6: Top: the initial stages of nanoribbon formation from stacks of PCC molecules encapsulated in nanotubes in TEM. When in the correct orientation, PCC molecules react to form a stable bent intermediate structure. Under continued irradiation, this species becomes planar, and further additions of PCC can occur. Bottom: the overall reaction from PCC stacks to a chlorine-terminated nanoribbon. Experimental TEM images courtesy of Prof. Andrei Khlobystov, University of Nottingham and Johannes Biskupek, Ulm University.

intermediate structures can be seen forming during the reaction. After being irradiated, two PCC molecules react to form a structure bent at an angle of 90 to 110°. This intermediate species survives for a considerable time before forming a planar structure, implying that it must be a stable structure that requires a second impact from the beam in order to be activated.

A proposed mechanism, shown in Figures 3.7 and 3.8, consists of the electron beam activating a PCC molecule by emitting a chlorine atom, forming an aryne species that can undergo a Diels-Alder cycloaddition with an adjacent PCC molecule to form the intermediate product $C_{48}Cl_{22}$. This structure is stable, and the optimised geometry matches the angular shape seen experimentally due to the presence of two bridging sp^3-C atoms. A second impact from the electron beam breaks open this protruding C-C bond, allowing a radical rearrangement and addition alongside the emission of Cl_2 molecules. Recombination of the radicals restores a fully aromatic sp^2 structure, corresponding to the planar structures seen. As each end of this dimer structure exactly resembles the original PCC molecule, further additions of $C_{24}Cl_6$ units can take place in the same manner to form the graphene nanoribbon.

The formation energies per atom for each species shown in Figures 3.7 and 3.8 are shown in Table 3.2. As the structures have different numbers of atoms and different ratios of C:Cl, formation energies were calculated as for a previous study:[79]

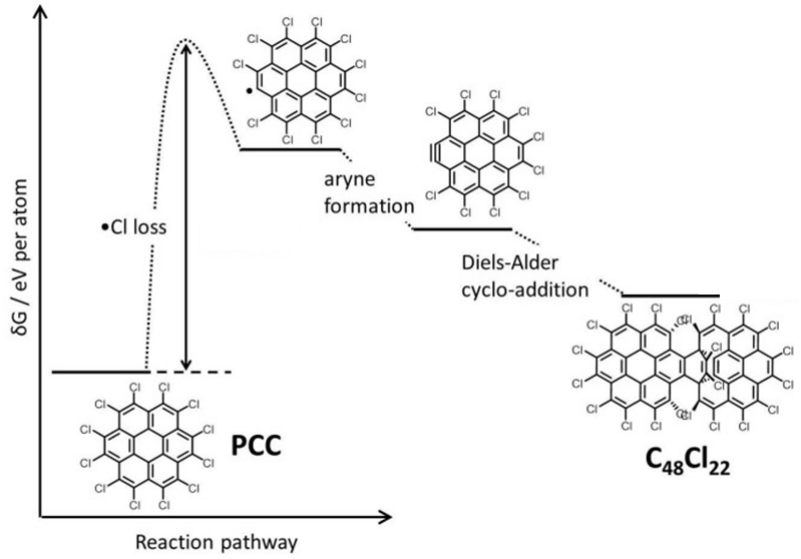


Figure 3.7: Step 1: beam induced emission of Cl, followed by aryne formation and a Diels-Alder reaction with an adjacent PCC molecule to form the Diels-Alder product $C_{48}Cl_{22}$.

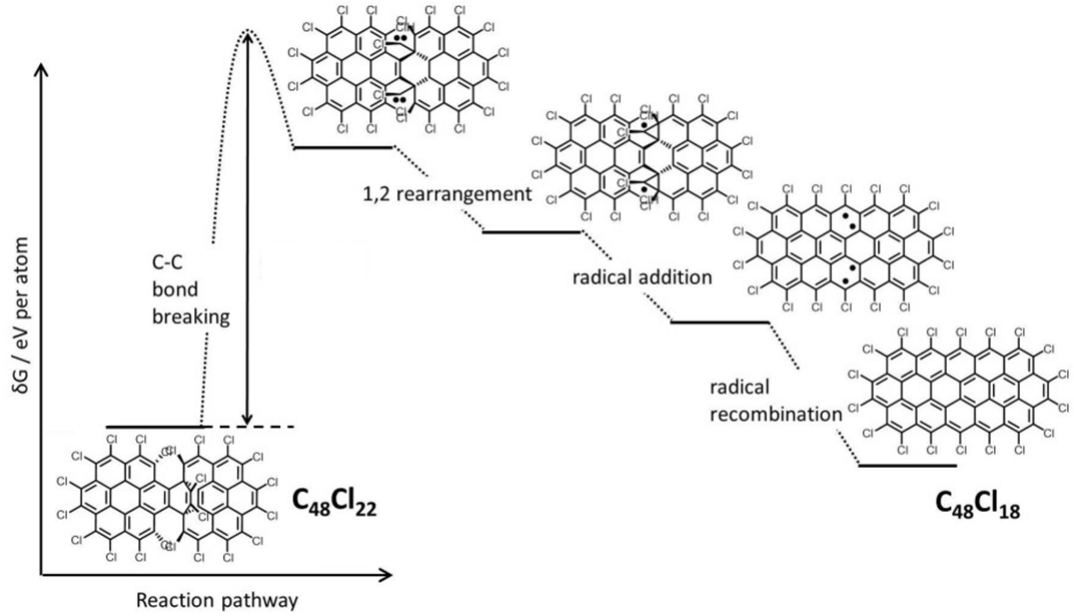


Figure 3.8: Step 2: beam induced breaking of the bridging bond in the Diels-Alder product, followed by Cl_2 emissions and radical rearrangements to form the aromatic planar dimer.

Table 3.2: Cohesive (E) and formation (δG) energies for the species shown in Figures 3.7 and 3.8

Structure	**Total energy (eV)**	**E (eV/atom)**	**δG (eV/atom)**
$C_{24}Cl_{12}$	-175156	-5.31	-0.036
$C_{24}Cl_{10}$	-150108	-5.45	0.072
$C_{48}Cl_{22}$	-325264	-5.37	0.018
$C_{48}Cl_{20}$	-300215	-5.42	0.097
$C_{48}Cl_{18}$	-275178	-5.66	-0.005

$$\delta G = E - x_{Cl}\mu_{Cl} - (1 - x_{Cl})\mu_{Cl} \tag{3.1}$$

where E is the cohesive energy per atom of the total structure, x_{Cl} is the molar fraction of chlorine atoms and μ_a is the chemical potential of a. The cohesive energies were calculated as

$$E = (E^{tot} - N_{Cl}E^{Cl} - N_C E^C)/N_{atoms} \tag{3.2}$$

where E^a is the total energy of a and N_a is the number of atoms a. μ_C was taken as the cohesive energy per atom of graphite (-7.37 eV)[79] and μ_{Cl} was calculated as the binding energy per atom of the Cl_2 molecule $(E^{Cl_2} - 2E^{Cl})/2 = -1.07$ eV. All calculations were performed for the ground state spin multiplicities at the B3LYP/6-31G* level of theory.

In order to investigate whether the two proposed beam induced steps are possible under electron irradiation at 80 kV, and if so to fully characterise them, the next two sections consider the irradiation response of PCC and the Diels-Alder product $C_{48}Cl_{22}$. In contrast to the simulations involving the sulphur-terminated nanoribbon in Section 3.2 and coronene and d-coronene in Section 3.3, quantitative and even qualitative differences occurred between simulations using the 6-31G and 6-31G* basis sets. It is likely that this is due to 6-31G inadequately describing the more diffuse electron density in these systems caused by the highly electronegative chlorine atoms. For all calculations in this section, the 6-31G* basis set was therefore used.

3.4.1 Chlorine emission

Rotation of the PCC molecule in the nanotube results in two orientations relative to the electron beam, shown in Figure 3.9. DFT-MD simulations of the transfer of 15.8 eV of kinetic energy (T_{max} at 80 kV) to each atom in the direction of the beam were performed for all inequivalent atoms in both orientations, in order to screen the molecule for processes accessible to the 80 kV beam. In the zig-zag (ZZ) orientation, impacts on two inequivalent atoms of PCC at 80 kV can lead to atom emission. However, these simply correspond to processes that are also accessible when the molecule is in the armchair (AC) orientation, but with energy transferred in suboptimal and inefficient directions. The preference of the AC orientation of PCC for emission is due to the presence of C-C and C-Cl bonds

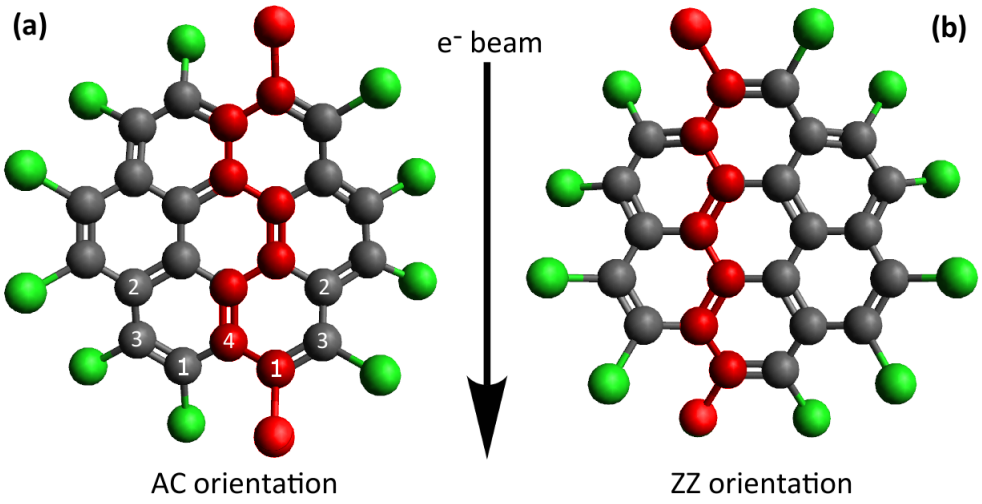


Figure 3.9: The two extreme orientations of PCC@SWNT relative to the e-beam (direction shown by arrow), with (a) armchair (AC) and (b) zigzag (ZZ) configurations along the beam axis, indicated in red. Impacts with the inequivalent atoms labelled in (a) can lead to emission events accessible to the 80 kV electron beam.

parallel to the e-beam. Energy can be transferred more efficiently along these bonds to the terminating chlorine atoms.

There are 4 inequivalent primary knock-on atoms (PKAs) in PCC in the AC orientation for which atom emission is accessible *via* a direct knock-on collision at 80 kV. At this accelerating voltage, the maximum transferable energy to a stationary carbon atom is 15.8 eV, while the maximum energy transferable to chlorine is only 5.3 eV due to its larger mass. Atom emission is therefore only possible *via* an initial energy transfer to carbon atoms, subsequently leading to the emission of chlorine after this energy is redistributed through the molecule.

Impacts on PKAs (1) or (2) can result in the emission of a single chlorine atom, impacts on PKAs (3) can result in the emission of a CCl_2 fragment, and an impact on PKA (4) can result in the emission of two adjacent chlorine atoms. For small ranges of transferred energy, Stone-Wales-type bond rotations were also witnessed. Considering all of these avenues of beam-induced atom emission and the calculated threshold energies for each process, at 80 kV the total damage cross-section is 159 barn per PCC molecule, corresponding to an electron dose of 6.29×10^7 e^-/nm^2 per molecule, and consisting of 90% Cl emission, 8% CCl_2 fragment emission, and a negligible number of bond rotations and Cl_2 emissions. These results are summarised in Table 3.3, and the dependence of the cross-section of each process on the energy of the electron beam is shown in Figure 3.10.

It is difficult to directly compare this predicted rate of damage to PCC to the experimental images. The molecular stacks are stable up to doses of approximately 2×10^8 e^-/nm^2, but their reactivity appears to be highly dependent on the relative orientations of the molecules - intermolecular reactions occur only when the molecular stacks are disrupted and the molecules are sterically less restricted. The

Table 3.3: A summary of the beam induced processes of atom emission for PCC accessible to an 80 kV electron beam, with the calculated threshold energies. Cross-sections and characteristic doses D_c are given per molecule, at the experimentally used accelerating voltage of 80 kV.

PKA	**Result**	$\mathbf{E_d}$ **(eV)**	$\sigma_\mathbf{d}$ **(b)**	$\mathbf{D_c}$ **(e^-/nm^2)**	**% of damage**
(1)	Cl emission	9.1 ± 0.1	127	7.87×10^7	80 %
(2)	Cl emission	14.4 ± 0.1	16	6.25×10^8	10 %
(1)+(2)	**Cl emission**	-	**143**	$\mathbf{6.99\times10^7}$	**90 %**
(3)	CCl_2 emission	14.7 ± 0.1	12	8.33×10^8	8 %
(4)	Cl_2 emission	15.1 ± 0.1	4	2.50×10^9	3 %
All	**Atom emission**	-	**159**	$\mathbf{6.29\times10^7}$	**100 %**

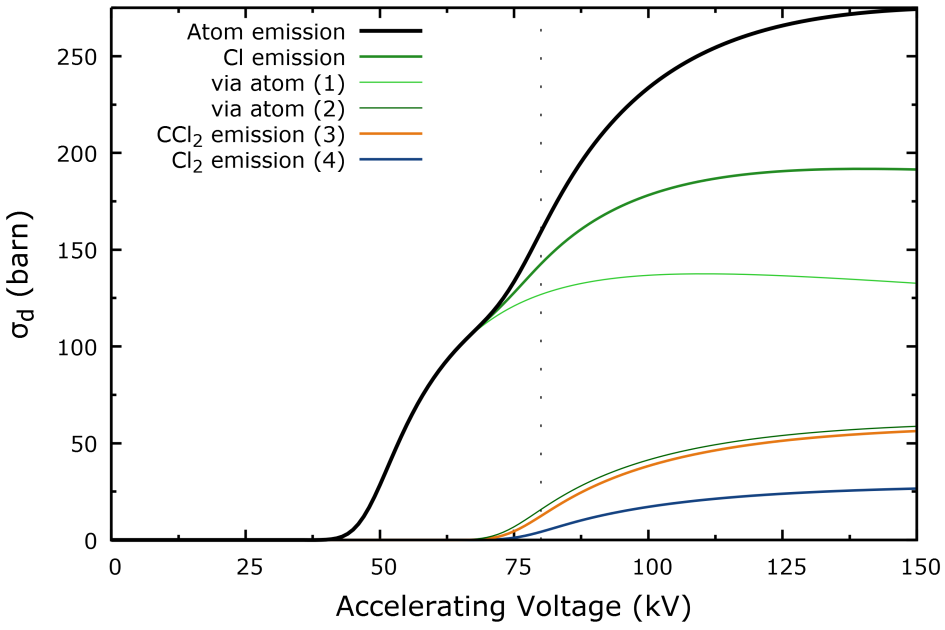


Figure 3.10: The total emission cross-section, per molecule of PCC, as a function of the accelerating voltage. This is broken down into constituent cross-sections for each emitted fragment and for each PKA indicated in Figure 3.9. The experimental accelerating voltage of 80 kV is indicated by the dotted black line.

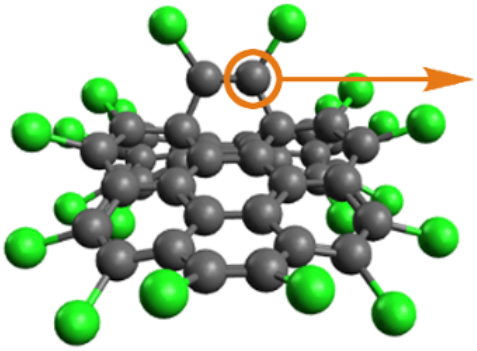


Figure 3.11: The Diels-Alder product, with the impacted atom in the out-of-plane sp^3 carbon bridge and direction of the transferred energy indicated.

Diels-Alder cycloaddition is a particularly sterically demanding process which will only proceed when the molecules are almost perpendicular to one another. Hence although the emission of chlorine may occur continuously under the beam, it is only when this occurs from a molecule at the edge of a stack (or that is otherwise free to adopt the necessary orientation) that it leads to a reaction with an adjacent molecule. Atom emission from molecules in the centres of stacks will be reversed by the recombination with free chlorine atoms before reacting as shown in Figure 3.7.

3.4.2 C-C bond-breaking

As discussed, the initial product formed from the Diels-Alder addition ($C_{48}Cl_{22}$) is stable, but due to collisions with electrons in the beam, the out of plane 'bridging' C-C bond can be broken as shown in Figure 3.11. The threshold energy for breaking this bond is 10.9 ± 0.1 eV, at which energy the impacted carbon atom and the chlorine atom bonded to it are captured by the edge, leading directly to the reaction pathway shown in Figure 3.8. Above 13.6 ± 0.1 eV, enough energy is transferred that a CCl_2 fragment is completely emitted from the structure. The reaction will follow the same pathway, but the resulting structure will have an additional carbon atom missing ($C_{47}Cl_{18}$ rather than $C_{48}Cl_{18}$), corresponding to a pentagon in place of the central edge hexagon.

The calculated cross-sections in previous sections have all been for reactions such as simple emission, for which there is a minimum threshold energy required for the reaction to take place (the atom to be emitted) and any energy transferred that is greater than this can safely be assumed to also cause emission. In this case however, there is a reaction with both a minimum and maximum threshold energy, i.e. the reaction only takes place between these limits, and transferring a greater amount of energy will lead to a different reaction. The cross-section of a process that occurs between two threshold energies can be calculated if these thresholds are known, as

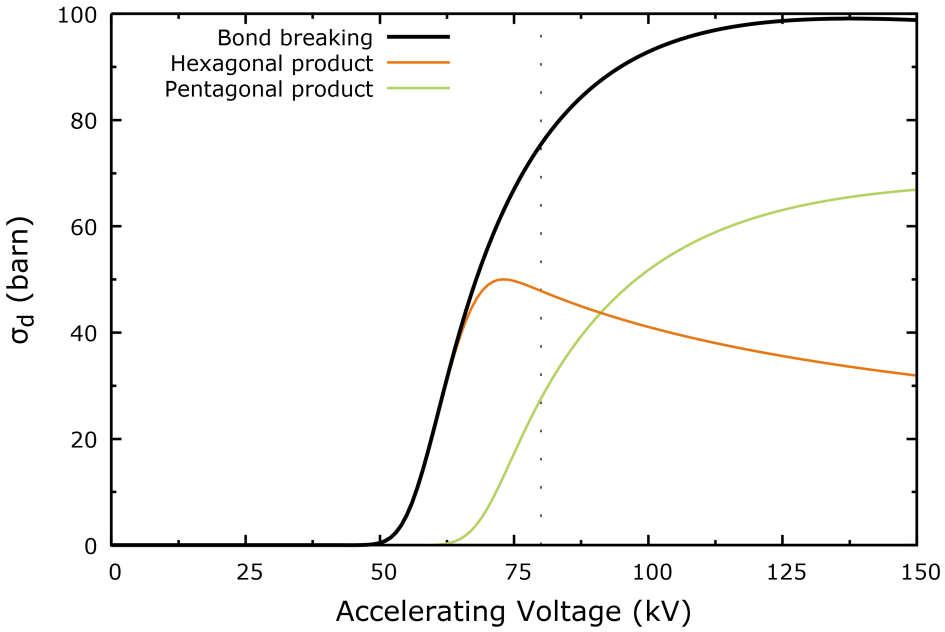


Figure 3.12: The total cross-section for breaking the bridging C-C bond, per molecule of PCC, as a function of the accelerating voltage. Depending on the exact energy transferred, the final structure will either contain a single pentagon or be completely composed of hexagons; the cross-sections for each of these possibilities are also shown. The experimentally used accelerating voltage of 80 kV is indicated by the dotted black line.

$$\sigma_t^E = \sigma_l^E - \sigma_u^E \tag{3.3}$$

where σ_x^E is the cross-section of a process with a threshold energy x at accelerating voltage E, calculated *via* the McKinley-Feshbach approximation (Equation 2.4), and t, l, and u denote the total process, the lower threshold and the upper threshold, respectively.

At 80 kV, the overall cross-section for breaking this bond is 76 barn, and the bond breaking accompanied by atom emission has a cross-section of approximately 28 barn. At 80 kV, the planarisation step will therefore be expected to occur after a characteristic dose of 1.32×10^8 e^-/nm^2, and approximately 27% of planarisation steps will be expected to produce products with a 5-membered ring at this accelerating voltage. This explains the observation that structures of nanoribbons formed from PCC are not perfect, and often include defects. Figure 3.12 shows the dependence of this step on the accelerating voltage, and indicates that the final structure of the nanoribbon can be tuned by the careful choice of experimental accelerating voltage; an accelerating voltage of approximately 65 kV is predicted to maximise the rate of this step while resulting in nanoribbons only consisting of hexagons, while above 90 kV a majority of couplings will result in pentagon formation.

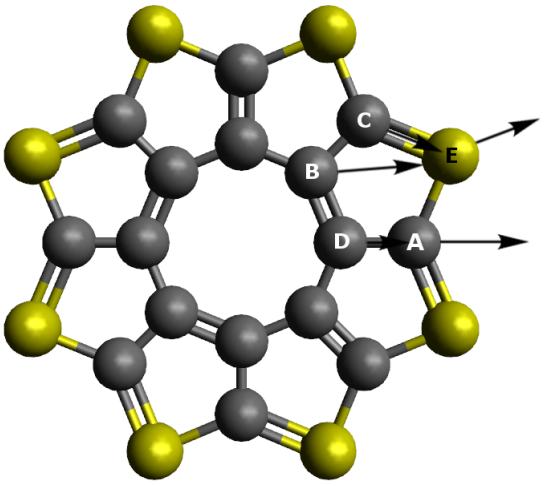


Figure 3.13: The sulflower molecule octathio[8]circulene, with the inequivalent impacts and their directions indicated.

3.5 Sulflower to nanoribbon transformation

By comparing results of the computational modelling of the irradiation induced processes of encapsulated molecules to the experimental TEM image analysis of the reactions of these molecules, the mechanism of the one dimensional polymerisation of PCC could be determined. In principle, this could be used as a more general method for inducing, observing and understanding new chemical reactions in TEM. In order to investigate the generalisability of this approach, a second reaction has been studied. Keeping in mind the general considerations discussed for observing this kind of reaction, the excellently named 'sulflower' molecule[86] (more formally octathio[8]circulene) shown in Figure 3.13, the first fully heterocyclic circulene,[?] seems to be an ideal candidate. The presence of sulphur atoms around the edge, with a similar mass to chlorine at 32 Da, will slow the rate of any reactions and stabilise the molecule (T_{max} is 5.9 eV at 80 kV). The size and shape is roughly comparable to PCC, being the same size as the carbon core of the coronenes, but unlike PCC it is completely planar. Sulflower molecules were able to be encapsulated inside nanotubes in the same manner as PCC, although this appears to be the first time this has been accomplished. The lower number of atoms will reduce the computational cost of DFT-MD simulations, while the very high symmetry will reduce the number of possible processes. Finally, this molecule is relatively new (first isolated in 2006), and therefore still has a largely unexplored chemical reactivity despite having significant potential for electronic applications.[?]

3.5.1 Initial atom emission and reaction

The highly symmetrical structure of sulflower means that there are only three atom environments (sulphur, inner carbon, outer carbon) and only five inequivalent

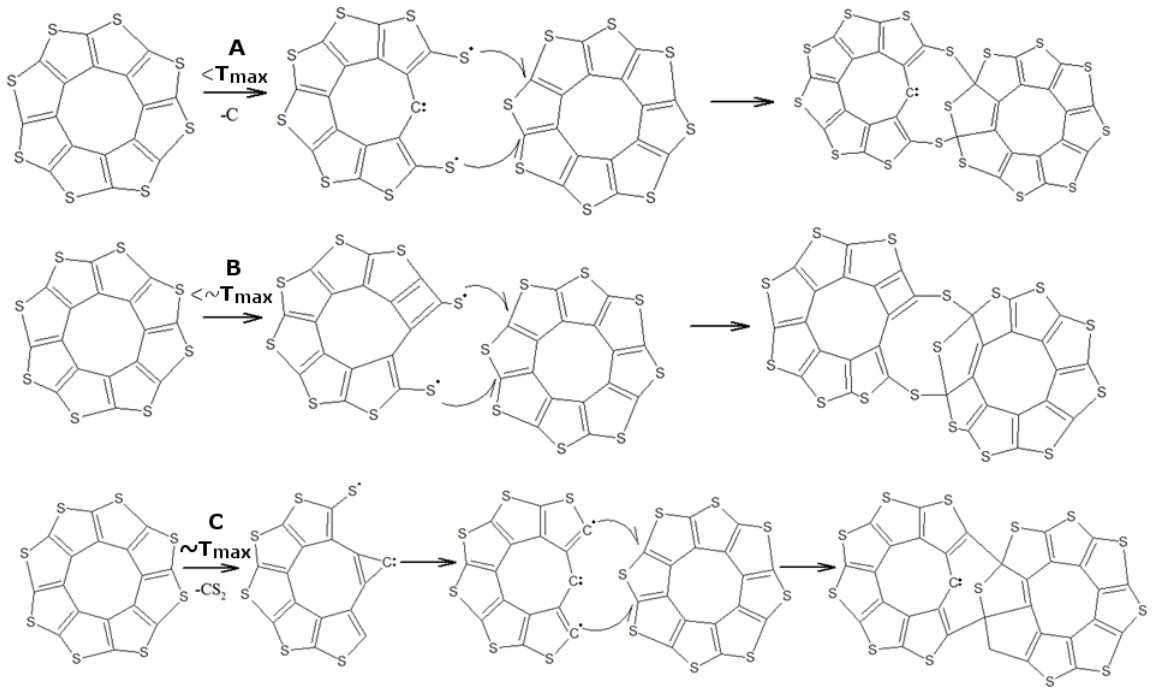


Figure 3.14: The results of the impacts shown in Figure 3.13 after transmission of T_{max}, and subsequent reactions that are possible with adjacent sulflower molecules. No reaction occurred for impacts D and E.

high-symmetry impacts with the possibility of structural modification, shown in Figure 3.13. After the transmission of 15.8 eV to atoms A to D and 5.9 eV to E, reactions were observed to occur for A to C, but not for D and E. Following impact C, a CS_2 fragment was emitted with a very low kinetic energy, indicating that this energy was very close to the threshold for emission. The remainder of the sulflower molecule rearranged to form a biradical species. For impact B, a bond rotation occurred, again forming a biradical species, but without any atom emission. In impact A, a carbon atom was easily ejected and retained a very high kinetic energy following emission, implying that the threshold energy for this process is substantially below T_{max}. A biradical species was again formed. These three activations by the beam and subsequent possible reactions with adjacent molecules in the stack are shown in Figure 3.14. As activation A is readily accessible under the 80 kV beam while the other two reactions will only occur at or around T_{max} (and therefore very rarely), only the consequences of A are considered. The three biradical species that are formed are very similar and would be expected to follow the same general mechanism, but will result in slightly different products being formed.

The radical driven reaction following impact A is not as sterically demanding as the Diels-Alder reaction required for PCC, but should be able to occur in the molecular stacks. In fact, the dimer species formed prefers a U-shaped orientation very similar to that of the parallel stacked molecules, with an angle of 40° between

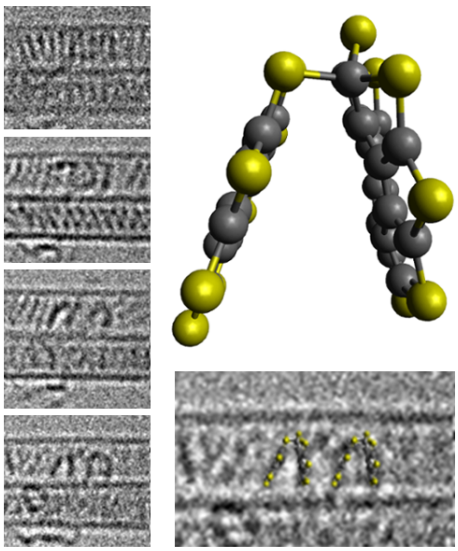


Figure 3.15: The optimised geometry of the product of impact A following the reaction with an adjacent molecule as shown in Figure 3.14, and the formation of similarly shaped species in the TEM images. The bottom experimental image is shown again with the DFT optimised structure overlaid for comparison. Experimental TEM images courtesy of Prof. Andrei Khlobystov, University of Nottingham and Johannes Biskupek, Ulm University.

the planes, caused by the two sp^3-C atoms bonded to the bridging sulphur atoms (shown in Figure 3.15). This matches stable structures seen experimentally during the transformation, also shown in Figure 3.15.

3.5.2 Subsequent emission and conformational changes

Following the formation of this stable species, two atoms are especially vulnerable to emission *via* a collision with an incident electron: the under-coordinated carbon atom and a sulphur atom, as shown in Figure 3.16. The sulphur atom is readily emitted even *via* an energy transfer to the sulphur atom itself, despite the low value of T_{max}, and the carbon atom is also very easily lost with a threshold energy substantially below T_{max} for carbon. These atom emissions would therefore be expected to happen relatively quickly, but in either order.

After sulphur emission (either as the first or the second step), the structure returns to being fully sp^2 and a conformational change of the molecule can occur. The two bridging C-S-C bonds begin in a 'cis' configuration due to the relative orientation of the two precursor molecules, but inversion of one of them leads to a 'trans' configuration that allows some degree of planarisation. If the carbon atom is also emitted, the final 'trans' structure is only slightly non-planar, and is composed of a 7- and 8-membered ring surrounded by thiophene groups, with two bridging sulphur atoms between them. This is shown in Figure 3.16, with the two possible routes and both configurations.

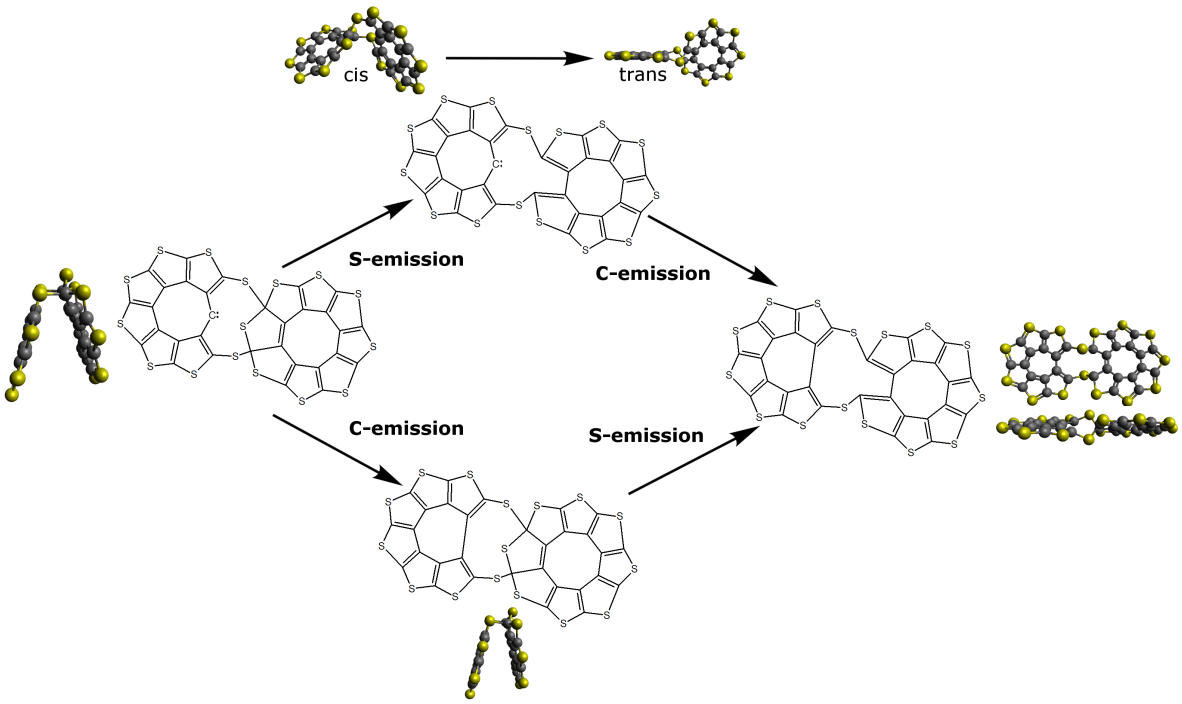


Figure 3.16: The atomic structures and DFT-optimised geometries of the dimer species and C- and S-emissions. In the top route, a sulphur atom is emitted, forming a larger-angled species that can undergo a conformational change (top) and emit a carbon atom. In the bottom route, a carbon and then sulphur atom is emitted, after which the conformational change can occur. In both routes the same final dimer structure is formed.

Although the carbon atom can be emitted, and the sulphur atom emitted so readily that 5.9 eV is substantially more than the threshold energy, at 80 kV an impact at T_{max} on the carbon towards the sulphur does not transfer enough energy to simultaneously emit both. The removal of the two atoms will therefore occur as a result of two separate collisions, leading to a long time (atomically speaking) between emissions, and so the structures will be fully relaxed into their ground states between impacts. At a higher accelerating voltage, simultaneous emission would be possible and could lead to a rearrangement resulting in the formation of a perfect thiocirculene, similar to the starting material but with a central 15-membered ring (pentadecathio[15]circulene). This could only occur following simultaneous C- and S-emission, as after emitting only one of the atoms the molecule quickly relaxes to a geometry where the thiocirculene formation is impossible.

Due to the large internal angle of a [15]circulene, its stable geometry is helical, and a planar structure similar to those of the nanoribbons that are formed would induce a huge amount of strain. It is however interesting to note that the original orientation of two adjacent sulflower molecules in the stack is ideal for this preferred helical structure, as well as the intermediate structure shown in Figure 3.15 - this entire process would not require any rearrangements of the molecular stack, but only very minor adjustments in position. Due to the nanotube confining the sulflower molecules in a coincidentally perfect sterical configuration required for the helical structure of large circulenes, at a higher accelerating voltage the electron beam could in principle drive the formation of arbitrarily large thiocirculenes from molecular stacks of sulflower molecules encapsulated inside carbon nanotubes. As there is no current chemical route towards heterocirculenes of this size despite interest in them,[87] the electron beam could prove to be a very useful tool for the synthesis of this kind of new and interesting one dimensional nanostructure.

3.5.3 Further molecular additions

Considering the structure of the end dimer product shown in Figure 3.17 with respect to further additions of sulflower molecules, there are only two possible structures for a trimer (assuming that the same mechanism occurs), as the presence of the nanotube limits any further reactions to occurring along the same axis of the molecule. One end of the dimer resembles the initial sulflower in the orientation that a carbon atom is emitted from (the left side in this figure), while the other end of the dimer is in the orientation that reacts with the impacted molecule (the right side). Hence, an electron impact emitting a carbon atom from the left of the dimer can react with a new sulflower molecule to form a '8-6-8' species, and the right side of the dimer can react following the emission of a carbon atom from a new molecule to the right of the dimer, to form a '7-8-7' species, shown in Figure 3.17. Repeating this process, the resulting infinite thiophene nanoribbon will have a '...-8-6-8-6-...' structure in the ideal case.

Although the experimental analysis of this reaction is still ongoing, the general observations made and shapes predicted in this computational study appear

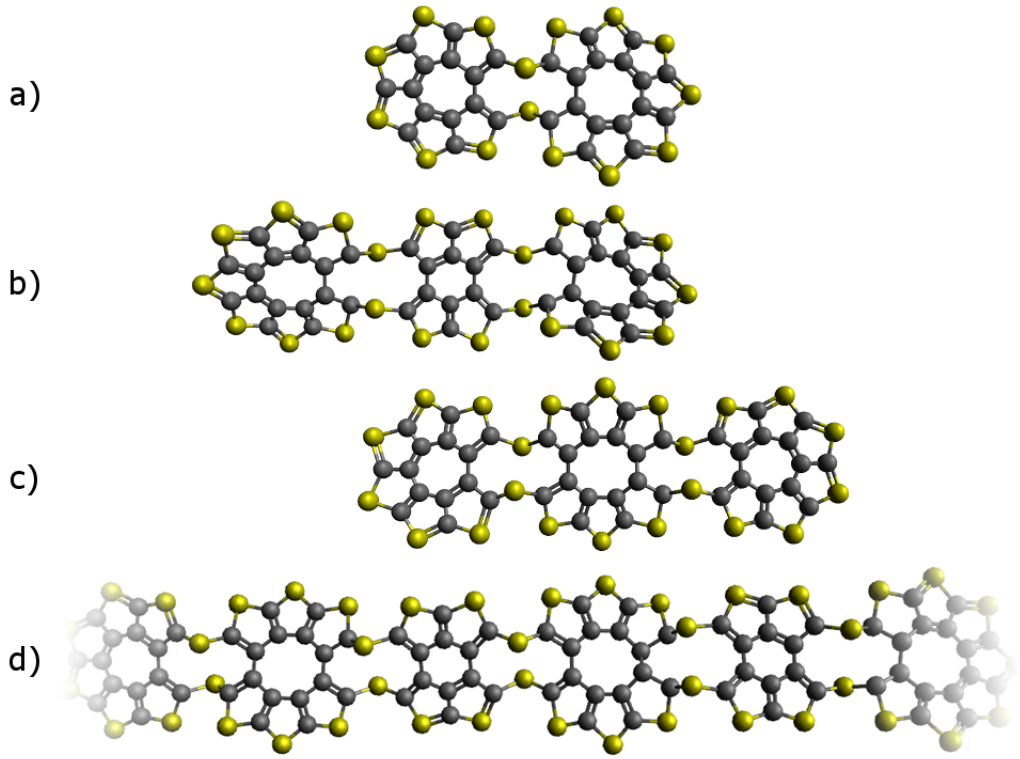


Figure 3.17: (a) The atomic structures of the '7-8' dimer, (b) the '8-6-8' trimer, (c) the '7-8-7' trimer, and (d) the infinite '...-8-6-8-6-...' nanoribbon.

to match the TEM images. In addition to the 'U'-shaped structures in Figure 3.15, there appear to be very few hexagons in the final product, generally unusual for nanoribbons but in agreement with the predicted structures. The ribbon also appears to be particularly twisted, which could be inherited from the 'trans' structure shown in Figure 3.16; if multiple sulflower additions are made before the carbon atom is emitted then the twists could effectively become locked into position.

In this and the previous section, the general mechanisms of two beam induced reactions have been described. However, it should be emphasised that these are only the main routes available, composed of the most probable beam-induced steps; under the electron beam large amounts of energy are transferred randomly to different atoms at different angles, resulting in very stochastic processes. A distribution of exact atomic structures will be formed along the ribbons. This is especially the case with the sulflower reactions described in this section, as in addition to the multiple initiating steps, the end structure will still be vulnerable to atom emission and bond reorganisations from the e-beam, unlike the perfect S- and Cl-terminated graphene nanoribbons. This structure is therefore the ideal case, simply the most probable structure formed immediately after polymerisation. It is likely that over time the structure would tend to reform towards the graphene nanoribbon after many impacts, so that at an infinite dose the same product would be formed as in Section 3.2.

Chapter 4

Graphene defect dynamics in TEM

TEM has become almost the *de facto* tool of use when studying two dimensional materials such as graphene. The easy (normally direct) interpretation of experimental images, coupled with graphene's high stability under irradiation and aberration corrected TEM's atomic resolution, has led to a huge number of TEM studies of graphene, with many devoted to characterising the structures formed as a result of electron irradiation.[9,10] As a consequence of the relative simplicity of these processes and the wider interest in graphene in general, the behaviour under the beam is known in much more detail for graphene than for the kind of nanotube-encapsulated organic molecules examined in Chapter 3. The exact sequence of events under electron irradiation is always different as damage from the beam is a stochastic process, but the same general structures and processes can be reliably observed. The next section will analyse an experimental atomic resolution 80 kV TEM time-series of graphene step by step, in order to provide context for the discussion of the individual atomic processes and structures, and to give an example of the general trends seen in the formation, growth and dynamics of defect structures under the electron beam. Some of the novel structures observed in this sequence of images will be discussed in more detail in Section 4.2.

4.1 Graphene under electron irradiation

At room temperature, all of the defect dynamics seen under the electron beam and discussed in this section are thermally inaccessible, as the lowest activation energies of these processes are typically several eV. As it can therefore be assumed that the atomic rearrangements observed are induced by the electron beam, the parameters for thermally induced reactions (such as activation and formation energies) are omitted from this discussion, but were included in a review article (reference 26), together with a more in-depth look at irradiation-induced processes in graphene.

Figures in this section are displayed with the original TEM image on the left and a filtered version of the image with colours indicating ring size on the right. Rings are coloured according to their size: 5, yellow; 6, white; 7, blue; 8, purple; 9, green; 10, red. Images are filtered by replacing the value of each pixel with the

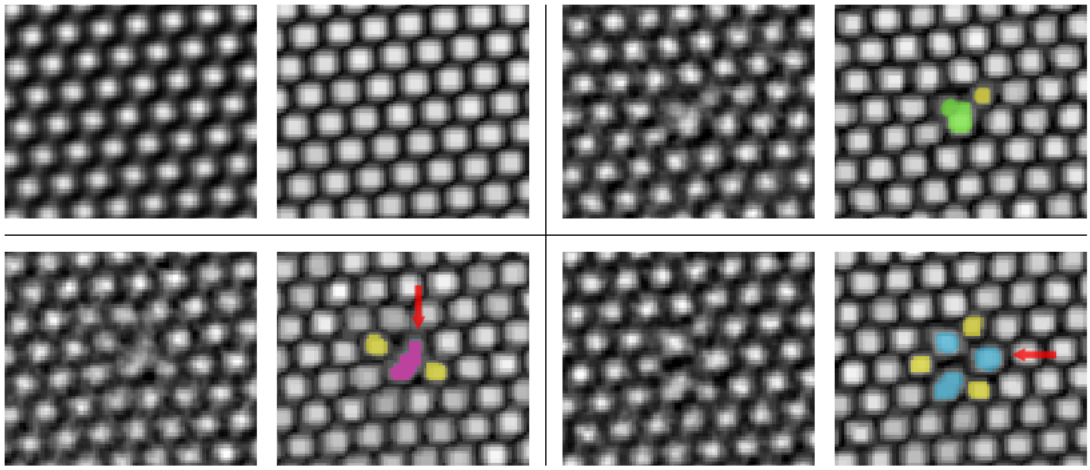


Figure 4.1: The small vacancy defects observed experimentally. Top left: pristine graphene. Top right: the reconstructed V_1(5-9) monovacancy. Bottom left: the reconstructed V_2(5-8-5) divacancy. Bottom right: the reconstructed V_2(555-777) divacancy. Original images are to the left and filtered images are to the right. Rings are coloured according to their size: 5, yellow; 6, white; 7, blue; 8, purple; 9, green. Red arrows indicate the bond rotations discussed in the text. Original experimental TEM images courtesy of Prof. Andrey Chuvilin, CIC NanoGUNE.

maximum value of a pixel in the 3x3 grid surrounding it, where black corresponds to a low value (and can be directly interpreted as electron density) and white to a high one.

4.1.1 Atom emission and recombination

The image series begins with an area of pristine graphene, which undergoes no transformations for a large electron dose before the emission of two carbon atoms leads to the formation of a divacancy (Figure 4.1). The emission of carbon atoms from pristine graphene in TEM has been extensively studied, both theoretically and experimentally. It has been observed that in order to eliminate atom emission and the creation of holes and defects, an accelerating voltage of 80 kV or lower must be used. Considering a static graphene lattice, this implies an emission threshold energy of approximately 15.8 eV, but including the thermal motion of the lattice increases this to 23.6 eV.[52,53] While graphene is therefore considered to be stable at 80 kV, emission is still possible (but rare) at this energy due to the probabilistic nature of the contribution of thermal motion to the emission cross-section. The cross-section never equals zero due to this contribution, but asymptotes towards zero at low accelerating voltages. Impurities in or on the graphene lattice can also lead to emission at this accelerating voltage.[17]

As discussed in Section 2.1.4, the experimental value of 23.6 eV gives a much better agreement with computationally calculated values, summarised in Table 4.1, but it is important to note that this is larger than every theoretical value,

Table 4.1: Threshold energies E_d (in eV) calculated for atom emission from pristine graphene.

Ref.	**System**	**Size of supercell**	**Method**	**E_d (eV)**
52,53	Exp.	-	-	23.6
30			DFTB	22.2
28	PBC	7x7 supercell	DFTB	23
51	PBC	4x6 supercell	DFT-PBE	22.03
88		120-200 atoms	DFTB	22.50
50	PBC	478 atoms	DFT-LDA	23
71	Graphene flake		DFTB	23.0
23	PBC	152 atoms	DFTB	21.34
89	PBC	160 atoms	DFT-PW91	22

by at least 0.6 eV and an average of 1.2 eV across all methods. A probable explanation for this can be found by comparing Figures 2.4 and 2.5, included in Section 2.1. The experimental threshold energy was calculated by fitting measured cross-sections at various accelerating voltages to the McKinley-Feshbach approximation,[53] which showed an excellent self-consistency between the experimental values and the fitted curve. However, as the form of the McKinley-Feshbach approximation used (Equation 2.11) makes an isotropic approximation of the threshold energy, while the real cross-section function has an anisotropic threshold energy, an error will be introduced. By considering Figure 2.4 the magnitude of the error can be approximated, as it shows the difference between the cross-section functions using an isotropic and anisotropic threshold energy (the purple and blue lines respectively). As the isotropic approximation overestimates the cross-section, using this to fit to the true cross-sections will overestimate the threshold energy, albeit by a small amount. It is likely that this accounts for the discrepancy between the experimental and computational threshold energies; rather than the computational numbers underestimating this value, the correct experimental value must be lower than the one reported.

Following the emission of a single atom from pristine graphene, a symmetrical vacancy or reconstructed V_1(5-9) structure is formed, shown in Figure 4.1.[90] In any structure with an odd number of missing atoms, there will always be at least one under-coordinated atom bonded to fewer than three atoms. These atoms will be more easily lost *via* collisions with electrons from the e-beam due to a decreased emission threshold, calculated as 12 eV for the unreconstructed vacancy[50] and 14.7 eV in the case of the reconstructed monovacancy.[16] As this energy is easily accessible to even an 80 kV electron beam, correlated sputtering of two atoms from areas of pristine graphene is normally observed, as is the case here.

Although areas of pristine graphene are generally considered to be immune to irradiation damage at or below 80 kV, the use of very high electron dose rates ($>10^8$ $e^-/nm^2/s$) at 80 kV has been shown to create defects.[91] Similar defect creation is not witnessed under lower dose rates ($<10^6$ $e^-/nm^2/s$) and long irradiation times, where large total numbers of electrons are passed through the sample (10^{10} e^-/nm^2),[52,53] meaning that a flux dependent effect is either lowering the threshold

energy or increasing the energy that can be transferred by increasing the out-of-plane atomic vibrations. This lowered threshold energy was calculated to be 19.7 eV, and weakening of the bonds due to ionization or plasmon excitations was suggested as a possible cause. Alternatively, while beam-induced heating effects were shown to be not responsible, a flexural phonon mode induced by inelastic collisions could result in the required increase in out-of-plane vibrations. An alternative possible explanation for this observation is considered in Section 4.3.6, but is shown to be incompatible with the measured cross-sections of this process.

After forming a divacancy, the next image is of the monovacancy shown in Figure 4.1, a result of vacancy-adatom recombination. Carbon adatoms are known to exist on graphene, being easily produced from the irradiation of surrounding carbonaceous material, and can easily migrate around the surface with a barrier of under 0.5 eV.[26] Carbon adatoms can play an important catalytic role, discussed more in Section 4.3, and have been shown to repair holes and defects in graphene.[92] As discussed, monovacancies are especially susceptible to beam induced emission, and this monovacancy is correspondingly short lived, quickly forming a divacancy again.

4.1.2 Bond rotations

Compared to the easily damaged monovacancy, even-numbered vacancies are fully coordinated with three bonds to each atom and subsequently have larger threshold energies, although the value varies depending on the ring size and to a smaller extent on the specific local structure. For example, atoms in pentagons typically have threshold energies around 16.9 eV,[71] depending on the local atomic structure. This generally leads to the formation of separate divacancies on the graphene lattice, as once a divacancy is formed there is a much smaller preference as to which atom will be emitted next, and the typically low concentration of defect sites means that additional emissions are likely to occur on pristine graphene. The increased lifetime of the divacancy also means that it is seen to reconstruct and migrate, both results of Stone-Wales (SW) transformations (a simple bond rotation, discussed in much more detail in Section 4.3). Bond rotations are generally considered to be the only major e-beam induced process of atomic structure change in graphene other than atom emission.

The divacancy in our experimental series migrates across the lattice for several images before reconstructing to form the V_2(555-777) structure shown in Figure 4.1. This reconstruction can occur as a result of rotation of the bond indicated with an arrow, and rotating the bond indicated in this structure forms a third stable and commonly seen divacancy, the V_2(5555-7777) structure, which does not appear in this image series but is shown in Figure 4.2.[88] A comprehensive study[50] mapped the threshold energies required for single-impact structure changes at different space angles for each of the V_2(5-8-5), V_2(555-777), V_2(5555-7777) and V_2(55-77) divacancy structures. It showed that the amount of energy required for a SW rearrangement is highly dependent on the angles of transferred momentum, ranging from 14 to 22 eV, and that different structures can result from impacts on the same atom, depending on the direction of momentum transfer. Figure

4.2 shows a summary of these findings, giving the threshold energy for each SW rearrangement indicated by an arrow. It is worth noting the inclusion of the reconstructed V_2(55-77) divacancy, as typically only the previous three structures are discussed.[25] This structure can be achieved *via* the rotation of a different bond in the V_2(5-8-5) structure, however with a threshold energy of 21 eV compared to the 16 eV required for the V_2(5-8-5) to V_2(555-777) transformation. In addition, the reverse process of V_2(55-77) to V_2(5-8-5) has the lowest threshold energy of any divacancy rearrangement at 14 eV, and so while this structure should be able to form under irradiation, it would be expected to have a shorter lifetime compared to the other reconstructed divacancies. Indeed, while it is very rarely seen in TEM, an example of this structure forming from a V_2(5-8-5) vacancy, before quickly undergoing the reverse transformation, has been observed.[93] This structure also provides a low energy route to the formation of trivacancies, with only 14 eV required to remove an atom and form the V_3(5-10-5) structure.

Two consecutive SW rearrangements are proposed to be responsible for a migration of the V_2(5-8-5) vacancy by one lattice unit *via* the V_2(55-77) structure.[93] The theoretical study described above[50] provided confirmation of the possibility of this proposed two-step mechanism; it confirms the ability of SW rearrangements to convert between the two divacancy structures, and the low irradiation stability of the V_2(55-77) structure (with the lowest threshold energy calculated, 14 eV) provides an explanation for both rearrangements happening in quick succession. An additional two step mechanism was proposed[93] for the V_2(5-8-5) vacancy rotating 60° around a pentagon, *via* an intermediate V_2(555-777) structure. The calculated threshold energies of these two steps, 16 eV and 19 eV, suggest that while this mechanism will be less likely to occur than the migration *via* the V_2(55-77) structure, it will be possible given an electron beam of sufficient energy. During the mapping of the threshold energies of various divacancy structures,[50] a previously unpredicted single-impact mechanism of V_2(5-8-5) migration was discovered, not occurring as a result of direct bond rotation. The threshold energy of this process is 19 eV, and due to the requirement of only one electron impact it would be expected that this mechanism of migration would be especially prevalent at sufficiently high e-beam energies.

4.1.3 Fast migration

Following the migration of the divacancy and its reconstruction to the V_2(555-777) structure, a 'ghosting' effect appears in the graphene lattice for seven images, shown in Figure 4.3. In all images of this previously unreported 'ghost' structure it appears as though no atoms are missing from the graphene lattice, but that multiple atoms have a reduced contrast. This can be explained by a structure that is highly dynamic, changing structure and position many times over the time of one image exposure, and therefore appearing as a superposition of all of them, weighted by the amount of time spent in each one. In the majority of images in which it appears, the distortion to the graphene lattice is confined to only the six atoms of one hexagon, which makes it an especially localised defect but also very usefully places tight limitations on any explanatory structure. In addition to being

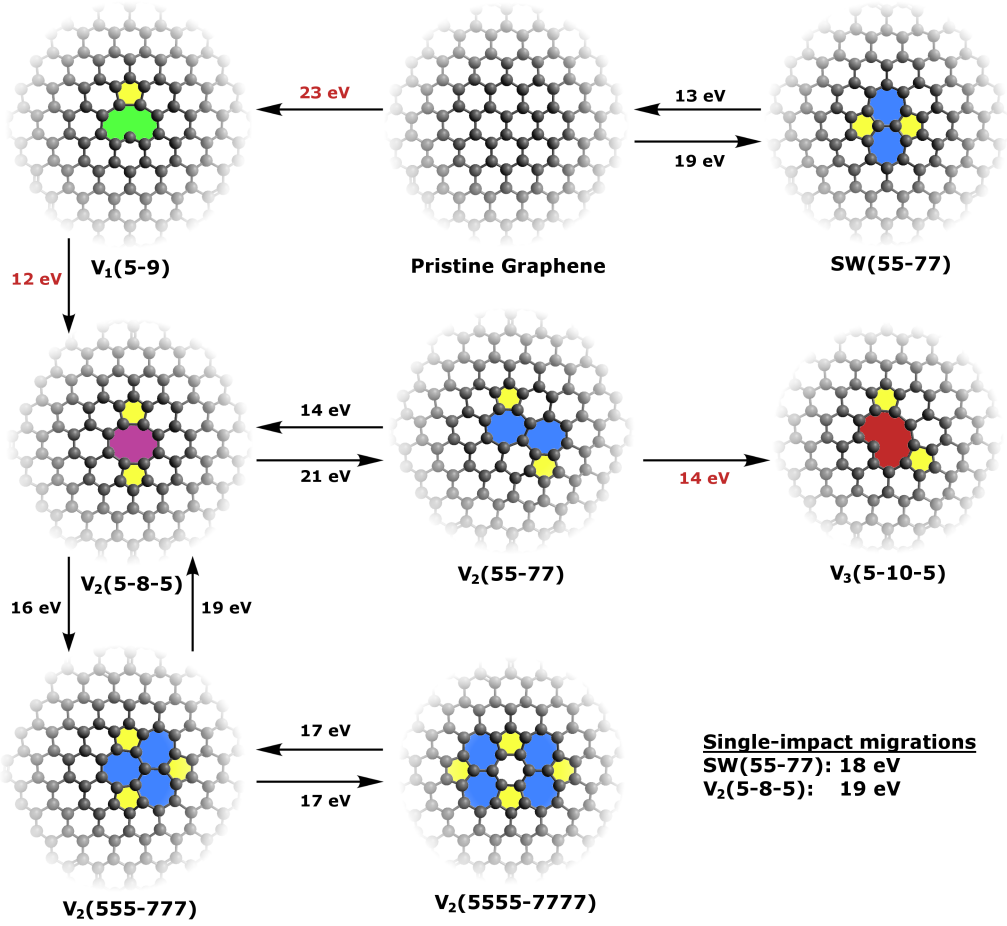


Figure 4.2: A summary of the threshold energies calculated for irradiation-induced processes in reference 50. Rings are coloured according to their size: 5, yellow; 6, white; 7, blue; 8, purple; 9, green; 10, red. Emission processes are labelled in red and bond rotations in black. Threshold energies are also given for the direct migration of structures across the graphene lattice due to a single impact from the e-beam, only witnessed for a small number of combinations of angle space and transferred energy.

dynamic within each image, this species migrates across the graphene lattice at a very quick rate, far faster than observed for vacancy structures *via* multiple SW transformations. This defect is considered in more detail in Section 4.2.

4.1.4 Larger vacancy structures

After the fast 'ghost' migration, a series of directly interpretable tetravacancy structures form. Unlike the three stable divacancy structures, there is a very large number of possible tetravacancies. The three most commonly observed are shown in Figure 4.4, and can be seen to share very similar features. As with the divacancy reconstructions, the tetravacancy structures are related to one another by sequences of bond rotations; although these normally result in relatively small changes between very similar structures (for example conversions between the linear and bent V_4 structures in Figure 4.4 are seen, due to the rotation of the indicated bonds), a small number of bond rotations can lead to very different structures. Figure 4.5 shows an especially striking example of this, where there are two bond rotations in two consecutive images, leading to a very large structure change from the linear structure to the rarely observed three-fold symmetrical 'Y' structure.

A subsequent comprehensive account of different V_4 structures observed in graphene was published in 2014,[15] confirming the general structures seen here. This study also noted the high occurrence of the linear structures, which was explained as being due to its low energy configuration; they state that different tetravacancy structures belong to one of several groups that are related *via* successive bond rotations, and once a defect enters a group it is locked into it, eventually leading to the lowest energy configuration for that group. The linear and offset structures are the lowest energy structures in their respective groups, and hence the most commonly formed.

However, as bond rotations in graphene defect structures are driven by the electron beam, while each individual structure is thermodynamically stable, it is unclear that the energy of the states would determine the frequency of their appearance and subsequent stability. In other words, the beam stochastically moves the tetravacancy between adjacent (connected by a single SW rotation) local energy minima, and the relative energies of those minima and the barrier between them are essentially irrelevant, as the cross-sections of the two transitions determine the frequency of them occurring. As previously discussed, formation energies are often not correlated with threshold energies, and so the difference between the two cross-sections connecting the adjacent states cannot be inferred from the difference in energy of the states. Hence, the beam can easily trigger bond rotations that drive the tetravacancy structure back up the energy landscape, as seen in Figure 4.5. Although the number of possible routes to a structure will heavily influence the rate of formation, the relative radiation stabilities of the structures plays a vital role rather than their energies.

Although the three vacancy structures shown in Figure 4.4 were the most commonly observed structures, they were not necessarily the most commonly formed - when they were formed they were especially stable, surviving for multiple images

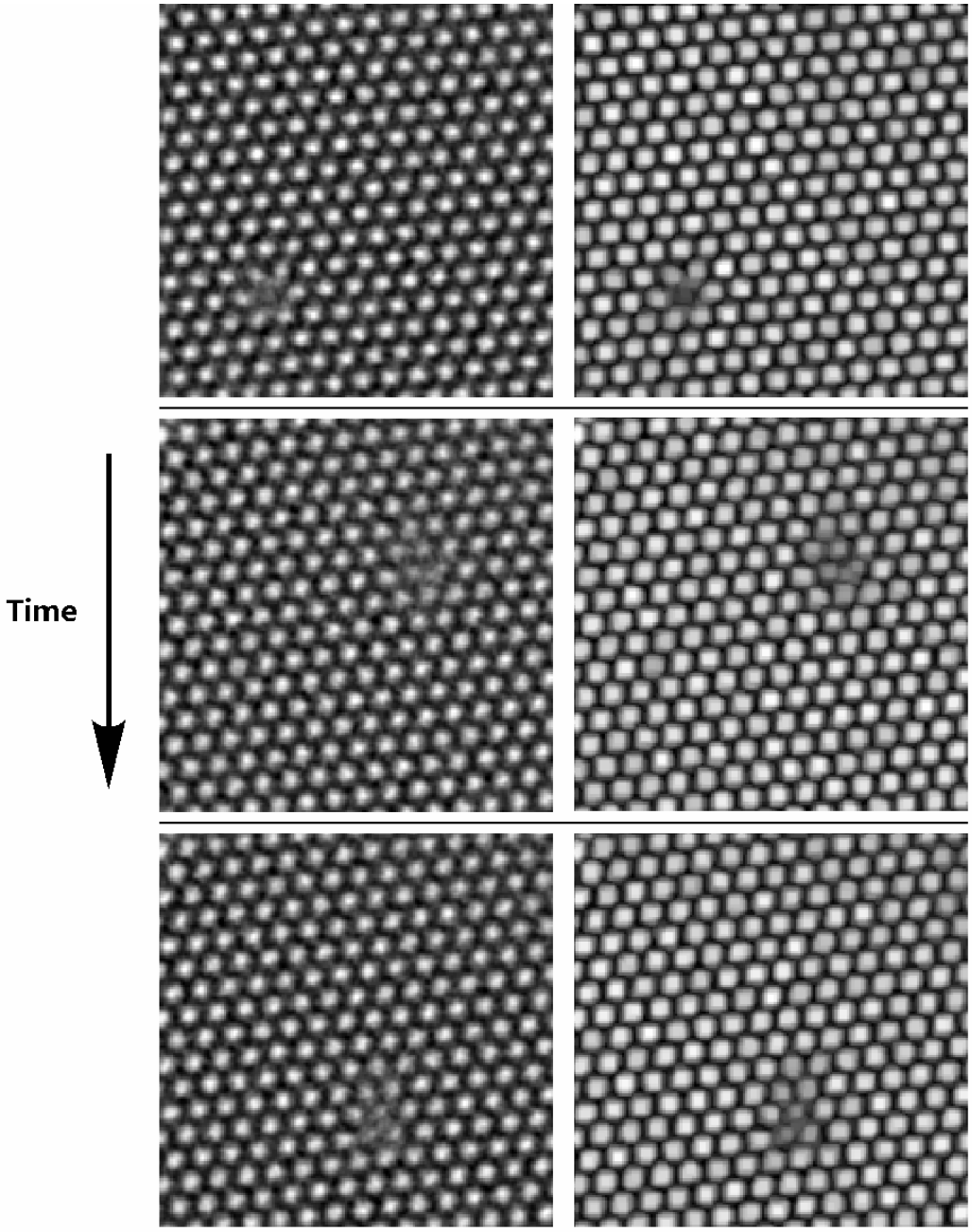


Figure 4.3: Three examples of the 'ghost' structures seen, demonstrating their fast movement across the graphene lattice. The most commonly observed structure is the top row, where the defect is fully localised around a single hexagon. Original images are to the left and filtered images are to the right. Experimental TEM images courtesy of Prof. Andrey Chuvilin, CIC NanoGUNE.

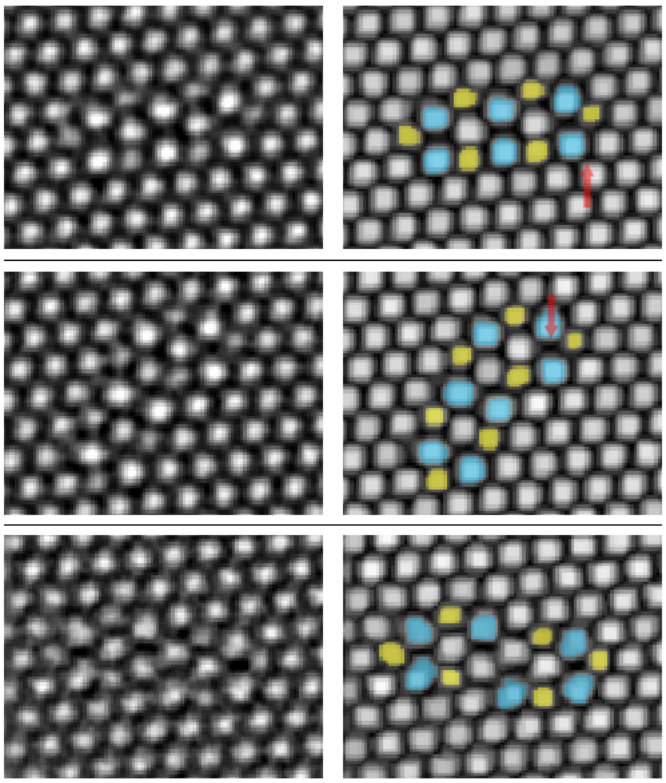


Figure 4.4: The three most commonly observed and stable tetravacancy structures, referred to here as linear (top row), bent (middle row), and offset (bottom row). Original images are to the left and filtered images are to the right. Rings are coloured according to their size: 5, yellow; 6, white; 7, blue. Experimental TEM images courtesy of Prof. Andrey Chuvilin, CIC NanoGUNE.

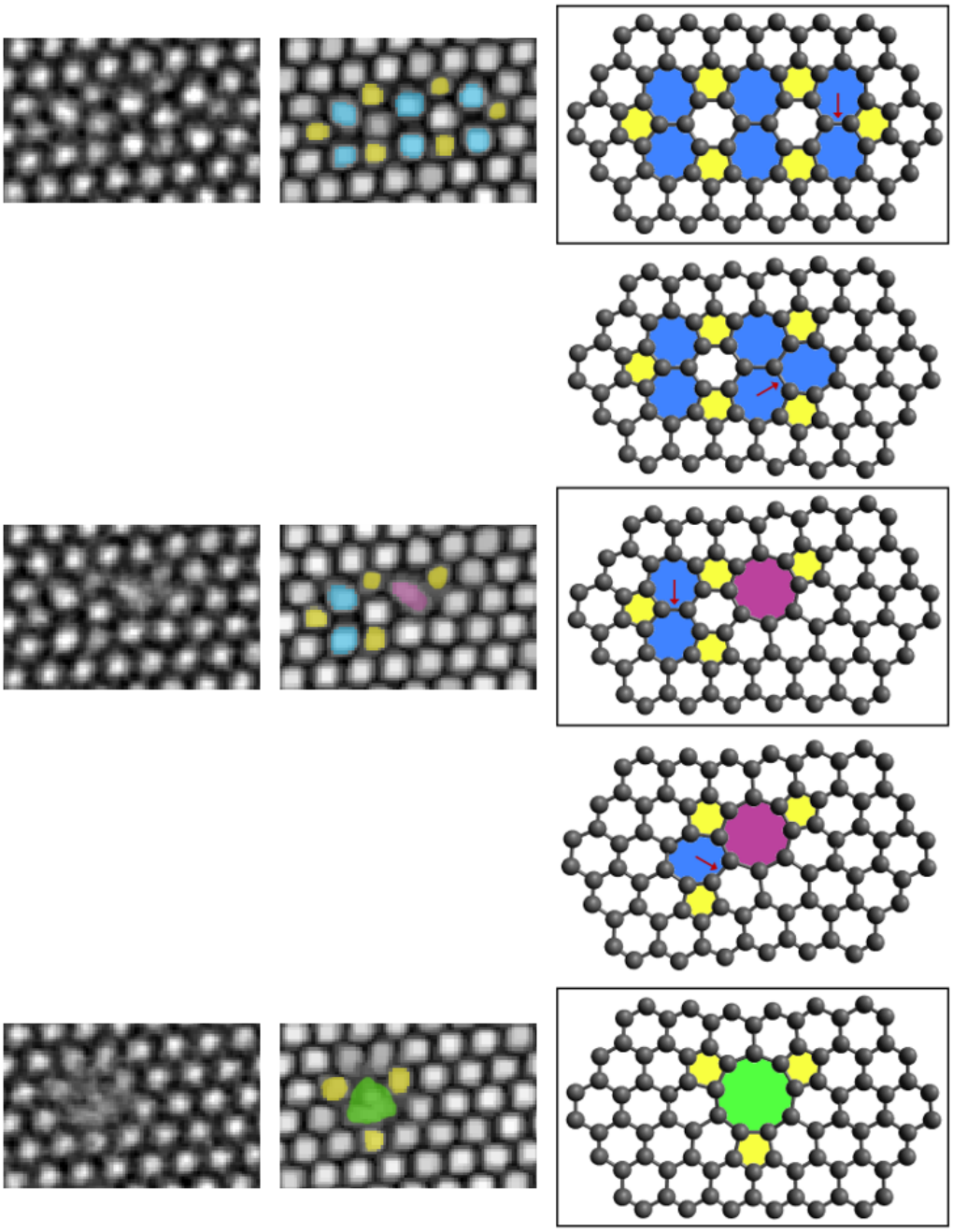


Figure 4.5: Three consecutive TEM images showing large structural changes of the tetravacancy, converting it from the linear to the 3-fold 'Y' structure. Original images are to the left and filtered images are in the middle column. These observations can be explained by two SW rotations occurring between each successive image, indicated by red arrows on the atomic structure models in the right column. Rings are coloured according to their size: 5, yellow; 6, white; 7, blue; 8, purple; 9, green. Experimental TEM images courtesy of Prof. Andrey Chuvilin, CIC NanoGUNE.

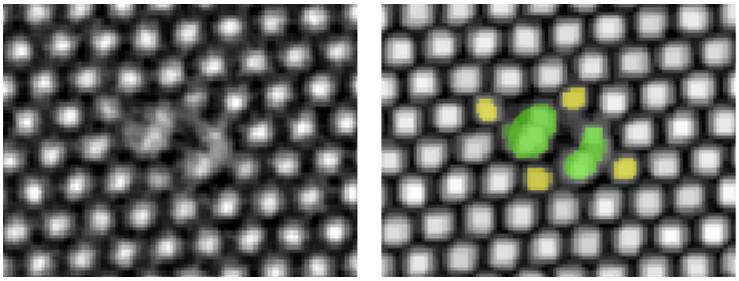


Figure 4.6: The highly symmetrical V_5(99-5555) vacancy, with a central stabilising bridging bond. Original image is on the left and the filtered image is on the right. Rings are coloured according to their size: 5, yellow; 6, white; 9, green. Experimental TEM images courtesy of Prof. Andrey Chuvilin, CIC NanoGUNE.

where all other structures in the series only lasted for one image. This implies that these structures are particularly stable against electron irradiation, which can be understood when comparing them to the third reconstructed divacancy, V_2(5555-6-7777), shown in Figure 4.2. The atomic structure of this divacancy is very similar to the linear tetravacancy, which can be considered as two divacancy units.[i] This divacancy structure has been shown to have an extremely high irradiation stability, with displacement thresholds for the central atoms being even higher than that of pristine graphene.[88]

The remainder of the image series is composed of well-defined tetravacancy structures interspersed with brief sequences of very fast migration of the entire defect site across the lattice (typically across five to ten hexagons in a single image), courtesy of the ill-defined ghost structure. A final notable structure is that of a highly symmetrical V_5 structure, shown in Figure 4.6. Although previously unreported, it fits the general category of the under-coordinated atom in odd-numbered vacancies being stabilised by acting as a 'bridging' carbon atom,[95] and in fact could be considered the 'ideal' prototypical example for the V_5 family. Consistent with the findings in the referenced study, the bridging atom moves considerably during the exposure time of the image. Odd numbered vacancies will be considered in more detail in Section 4.2.

4.2 Dynamic behaviour of trivacancies in graphene

Generally speaking the e-beam is considered to induce only two basic steps of atomic structure change in graphene: emission and bond rotation (ignoring effects that require interactions with other species adsorbed onto the graphene surface, such as chemical etching[96]). Here a third is proposed, which is relevant only to small under-coordinated vacancies but provides a mechanism of very fast vacancy structure migration under the beam.

[i] Extended infinite lines of defects of this kind have previously been studied theoretically, and are predicted to act as 1D metallic wires embedded in graphene.[94]

4.2.1 Structure

As described in Section 4.1.3, a ghosting effect appears within the graphene lattice during the dynamic sequence of vacancy defect migrations and rearrangements, which can be understood as a superposition of different stable structures that exist during the exposure time of the image. Although these images can not therefore be directly interpreted, clues to the form of the contributing structures lie in the context in which the species forms, the shape and size of the disruption to pristine graphene, and the contrast produced by it. In the image series, the periods in which the 'ghost' exists is exclusively bookended by either divacancy or tetravacancy structures; the structures both immediately preceding and following the ghosts are one of these defects in a 1:3 ratio, respectively. The most common structure seen is that of the top image in Figure 4.3, in which the disruption to the graphene lattice is localised on a single hexagonal ring. This structure accounts for over 60 % of the observed configurations, and corresponds to the area enclosed by a hexagon being filled with a relatively even dark contrast, measured to be 40 to 60% of a single atom in pristine graphene. In the remaining structures, the disruption to the graphene lattice is more widespread (most commonly affecting two to three hexagons but occasionally up to five or six), and the difference in contrast between these structures and pristine graphene becomes correspondingly smaller with increasing size, implying that a constant number of atoms is missing.

As the area affected in the most common structure is that of the V_6 hole[97] (discussed later), this area being filled with half the contrast of a carbon atom suggests a total of three missing atoms, consistent with the observed formation from and relaxation to di- and tetravacancies. Similarly, the highly localised nature of this structure puts the maximum number of missing atoms at six, while imposing tight constraints on possible structures. Finally, the even contrast seen means that the atoms spend an equal time in all positions on the ring, implying that multiple switches between the different configurations occur between each image and that these configurations are equivalent, or at least equally stable.

All of this evidence points decisively towards a trivacancy structure being responsible for the observed images. Trivacancies (as with all odd-numbered vacancies) are generally considered relatively unstable in TEM due to the presence of the under-coordinated atom, vulnerable to beam induced emission. Although trivacancy structures have been observed, stabilised with a bridging bond,[95] in the case of the ghost this instability could be the reason behind the fast dynamic behaviour witnessed. Several possibilities for the trivacancy structure are considered, shown in Figure 4.7. The reported bridging structure is much larger than the limit imposed by the highly localised ghost, and there is no clear way for the required dynamics to occur without invoking an infeasible number of bond rotations. However a hole structure, in which three adjacent atoms are simply removed from pristine graphene, is sufficiently small, corresponding to the V_6 hole filled with three carbon atoms in adjacent positions. Early theoretical calculations[98–100] predicted the reconstruction of this structure, but this has not been observed experimentally. A third structure is one in which three atoms are again added to the V_6 hole, but this time symmetrically in a three-fold configuration.

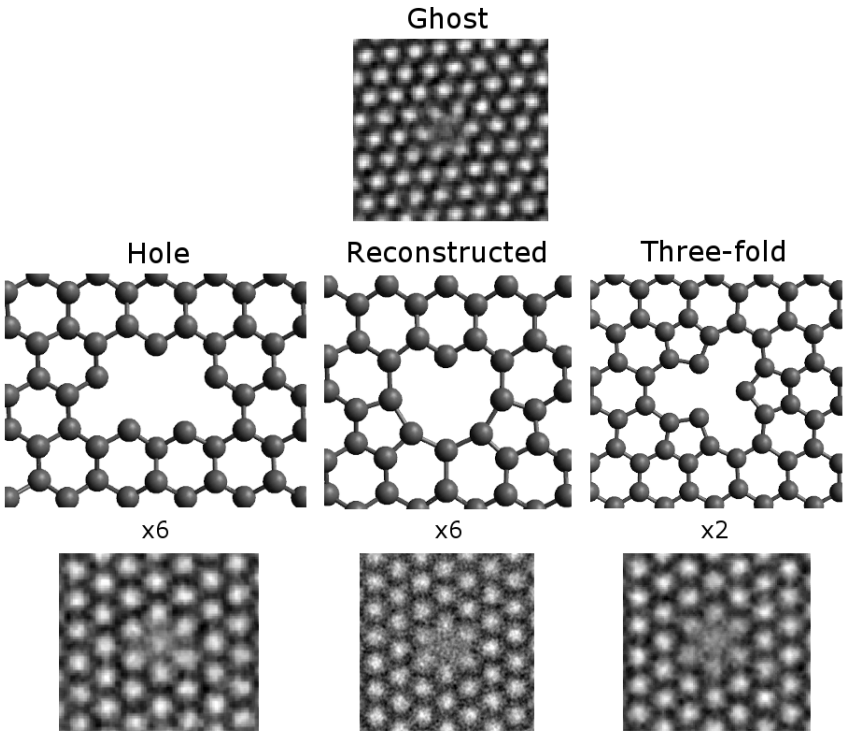


Figure 4.7: The three considered trivacancies: the hole, reconstructed, and three-fold structures. Multislice simulations show excellent agreement between the experimental ghost structure (top, courtesy of Prof. Andrey Chuvilin, CIC NanoGUNE) and equal mixes of the six (for the former two structures) and two (for the three-fold structure) possible configurations. Multislice simulations were produced matching the experimental setup: 80 kV; 10^6 e^-/nm^2, C_c = 0.1 nm, Scherzer defocus (-7.9 nm).

The threefold structure shown has two equivalent configurations, and can be considered as a V_2(555-777) structure with a central atom emitted. Notably, the first appearance of the ghost structure immediately followed this divacancy. A multislice image simulation of a superposition of both configurations with equal weight provides an excellent agreement to the experimental image, shown in Figure 4.7. This is very similar to an experimentally observed defect in STEM[101] in which three silicon atoms in a V_6 hole demonstrated fast dynamic motion, switching between the two equivalent configurations as proposed here. This Si-dopant defect has also been observed in TEM,[ii] where the switching produces images very similar to the observed ghost structure, although the doubled contrast of silicon compared to carbon results in the Si-ghost structure appearing with a very similar contrast to carbon, and the resulting structure resembles a hexagon in graphene being simply replaced with a smooth circle.

Considering the hole structure, the three central atoms have six equivalent possible positions. A superposition of these also matches experiment, albeit with a more well defined central structure than observed. The reconstructed structure also has six possible orientations, and while the conversion between these structures will be more difficult than for the hole, the simulated image combining the configurations provides a good match to the ghost. In principle, any of these three closely related structures can produce the experimental result. On the other hand, the bridging structure cannot explain the observed images: in addition to the lack of a clear mechanism for the required dynamics, the disruption to the graphene lattice extends well beyond a single hexagon, and it lacks the high degree of rotational symmetry that would allow such a superposition of different configurations to be produced.

A series of high temperature MD simulations on a large graphene sheet using the reactive empirical bond order (REBO) potential[102] were performed by Dr. Harriet Åhlgren in order to investigate these possible structures and rearrangement processes. At 2000 K, the initial three-fold structure (which in principle can be formed directly *via* atom emission from the V_2(555-777) vacancy) is unstable with respect to the lower energy hole structure, which interestingly does not undergo the previously theoretically predicted reconstruction.[98–100] A possible reason for the discrepancy is the much larger supercell used in these simulations (approximately 50 x 50 Ångstroms in size) compared to the previous calculations; the vacancy will be able to have a larger effect on the smaller graphene sheet. The reconstruction, which consists of the two pairs of under-coordinated atoms on the lower left and right of the defect in Figure 4.7 bonding to form two pentagons, requires either the considerable weakening and lengthening of several existing C-C bonds (inducing strain), or significant compression of the graphene sheet. Alternatively, the high temperature used could be preventing the reconstruction. In either case, the completely unreconstructed and reconstructed trivacancies can be taken as the two limiting cases for the structure.

While the hole structure was stable for 511 ns, after this a rotation step was observed, converting it to one of the other five possible configurations. Using the

[ii]Prof. Andrey Chuvilin, personal communication.

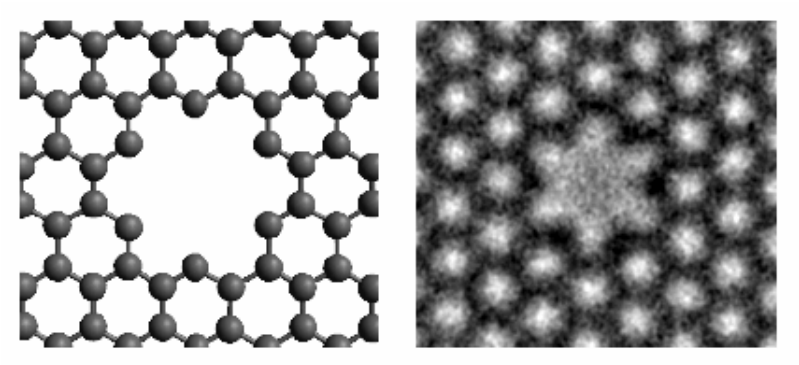


Figure 4.8: The structure of the V_6 hole, left, and multislice image simulation, right.

Arrhenius equation 4.2 (ignoring the temperature dependence of the prefactor) this characteristic time and temperature predicts an activation energy of approximately 2.54 eV, which is inaccessible at room temperature. Given this, and especially considering the multiple rotation steps required per second, if this is the correct process it must be induced by the electron beam. At 80 kV a direct knock-on collision with a carbon atom is easily capable of transferring the required energy for this step, and in fact a limiting factor in the likelihood of this beam induced step is that for a range of scattering angles the beam will be able to transfer more than the required energy and enough to fully emit an under-coordinated atom, as previous discussed in Section 4.1. This is consistent with the relatively short lifetime of the ghost seen experimentally; the average lifetime is five images, after which it forms a tetravacancy in 75% of cases or a divacancy in 25% of cases. It is interesting to compare the high temperature of 2000 K used computationally to the virtual temperature of 3000 K induced by the e-beam discussed previously.[13] Although it must be stressed that these are in no way directly comparable, it does give an indication of the temperatures that would be required in order for electron beam induced processes to be thermally accessible on the same time-scale. Further comparison can be made to the temperatures of 2000 - 4000 K required to simulate e-beam processes in Monte-Carlo simulations,[103] and to the general discussion in a recent study on this kind of virtual temperature.[14]

It is worth briefly returning to the V_6 hole structure, as experimental images of it look very similar to the ghosts discussed and shown here.[97] Although the structure of the V_6 vacancy is exactly the same as the ghost - the missing atoms in the former are localised on a single hexagonal ring, as is the disruption to the graphene lattice in the latter - the contrast in the central region is very different, as shown in Figure 4.8. In the V_6 there are no atoms in the centre and the contrast is consequently the same as the background signal, while there is an increased contrast on the six under-coordinated edge atoms. This structure is also extremely unlikely to cause the ghost when considering the numbers of missing atoms in the surrounding images, as discussed above.

4.2.2 Migration

Experimental images in which the ghost is not localised on a single hexagon can provide a useful insight into the mechanism behind the fast migration across the graphene lattice, by assuming that this captures the migration process. In several of the images, it is spread across exactly two hexagons, implying a step-by-step hexagon-by-hexagon migration. Considering the structure of the hole trivacancy, this can be explained as a result of an under-coordinated atom on one side of the hole being knocked towards the opposite side, as indicated in Figure 4.9. As with the rotation mechanism, this should be accessible to an 80 kV electron beam, provided that the energy is transferred at the correct angle.

4.3 Reaction kinetics of Stone-Wales rearrangements

The majority of defect structure dynamics under the electron beam, with the exception of the structure examined in the previous section, is driven by SW transformations. One very common e-beam induced process in graphene that was not observed in the experimental study in the previous section is the formation of an isolated SW defect in otherwise pristine graphene, and its subsequent healing. The rotation of a single carbon bond by 90° in otherwise pristine graphene converts four hexagons into a pair of pentagons and a pair of heptagons, shown in the top-right of Figure 4.2. The SW defect and transformation, being one of the two basic units of structure change in graphitic materials under irradiation (together with atom emission), has been extensively studied, but there are very few studies of the irradiation induced reaction and no quantitative estimates of its cross-section. In this section the existing literature is first briefly reviewed with regards to the thermal and irradiation induced barriers for SW transformations, before these are calculated from the kinetic consideration of experimental observations in TEM.

4.3.1 Literature review

The thermal barriers for SW transformations in graphene are well known, and the DFT-calculated values are given in Table 4.2.[iii] While both thermally activated formation and healing mechanisms have high enough activation energies to be infeasible at room temperature (typically 9 - 11 eV and 3 - 6 eV, respectively), and catalytic routes to formation[104] do not change this, it has been suggested that highly mobile carbon adatoms trapped on the graphene surface can provide an additional pathway for catalytic healing of SW defects.[105] This proposed route reduces the activation energy of healing a SW defect to only 0.87 eV, which is in principle thermally accessible. Although carbon adatoms are not directly visible in AC-HRTEM due to their high mobility, they are routinely produced by the irradiation of carbonaceous material and hence are readily available on the

[iii] The barriers calculated with semiempirical potentials can be substantially underestimated and are omitted from this table, but remain above 6 eV for SW formation.[26]

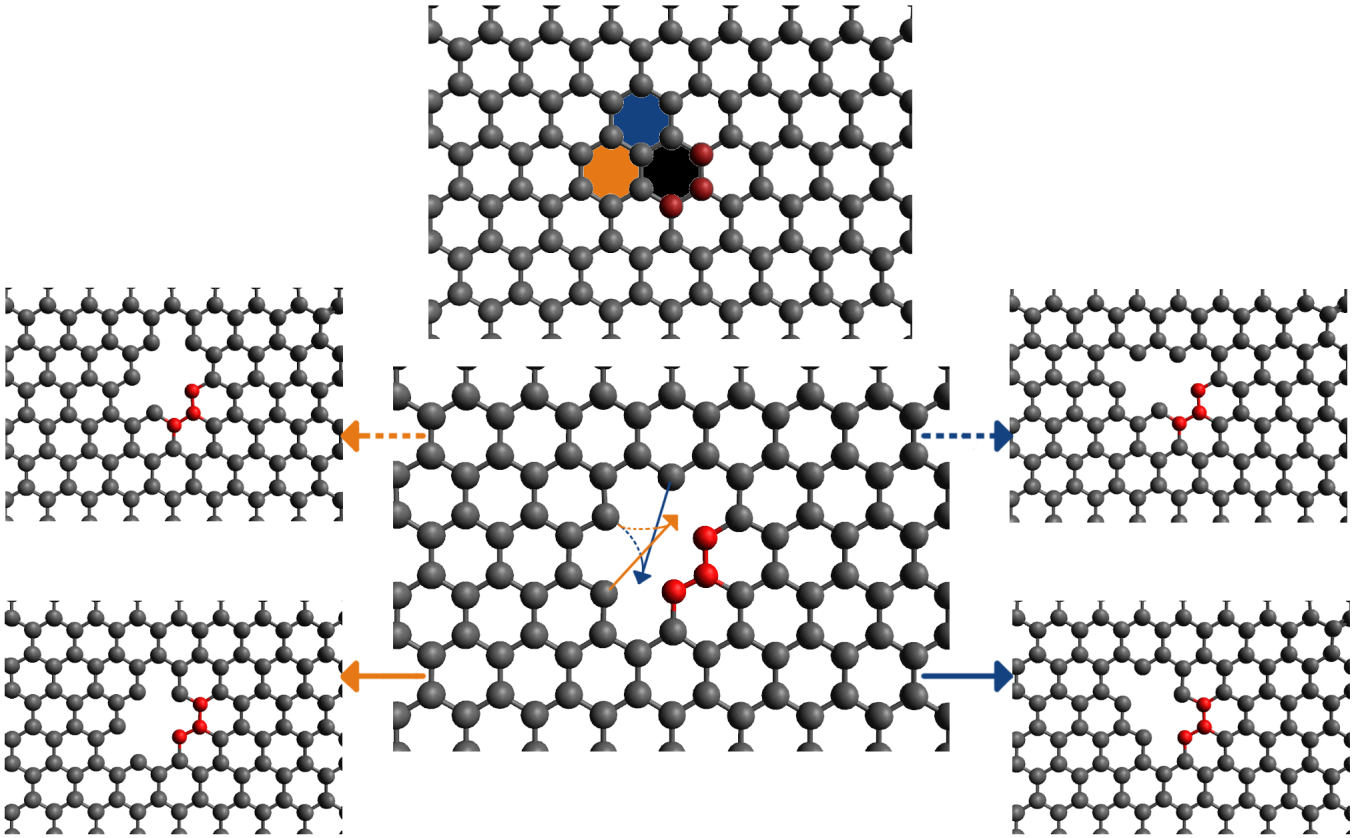


Figure 4.9: Possible migration steps for a given initial configuration of a hole trivacancy structure, central. Knocking any of the three indicated atoms results in the formation of an identical structure displaced by one hexagon, indicated with the orange and blue solid and dashed lines. Depending on the atom knocked by the beam, the migration of the original ghost (black hexagon, top) can be in one of two possible directions (orange and blue hexagons, top).

graphene layer. By taking the frequency factor computed from the harmonic vibrational frequencies of a SW defect in graphene,[106] 2×10^{12} s^{-1}, the average time required for this thermal process can be estimated from the Arrhenius equation 4.2. The calculated activation energy predicts an average lifetime of 260 seconds for a SW defect with an adsorbed adatom. This indicates that although the adatom-catalysed mechanism significantly lowers the barrier to healing and makes it accessible at room temperature, the timescales required for this mechanism are too long in typical AC-HRTEM conditions as the defects are healed much faster *via* other mechanisms.

However, it is important to note that the accuracy of this prediction is heavily dependent upon the choice of the pre-exponential factor and accuracy of the calculated activation energy. For example, an earlier computational study[104] found an activation energy of 0.7 eV for a similar mechanism on a SW defect on a graphene flake; this predicts a lifetime of only 0.35 seconds. On the other hand, a recently used[114] value of $P = 8.5\times10^{15}$ s^{-1} together with the 0.87 eV barrier results in an expected lifetime of 0.06 seconds, short enough that SW defects would be mostly invisible to TEM (barring an excessively high formation rate). Alternatively, using elevated temperatures would increase the significance of this pathway and increase the rate of healing, reducing the lifetime of SW defects. In order to increase the rate of this mechanism to be comparable to imaging timescales in TEM (1 s), a temperature of 356 K would be required. It should be stressed that these are characteristic healing times of the SW defect-adatom system; the actual observed lifetime of SW defects would therefore also be dependent on the availability and concentration of adatoms on the graphene surface. While these are known to exist, the surface coverage of carbon adatoms is unknown and may also depend on the temperature.[115]

Turning to irradiation induced routes, theoretical calculations confirmed the creation of the SW defect *via* direct knock-on impacts with electrons from the e-beam, revealing two mechanisms of formation.[88] SW formation was observed to occur in these simulations after the transfer of typically 1 eV lower than the emission threshold energy (calculated as 22.5 eV), with 2 eV below this resulting in SW formation at certain space angles of transferred momentum. The threshold energies for the formation and healing of a SW defect were calculated in a different study[77] as being 22.5 eV and 14 eV respectively, confirming the highly reversible nature of the defect seen experimentally. Other simulations[50] (using a much larger, converged supercell) gave comparable numbers, although slightly lower values of 19 eV and 13 eV for formation and healing. These latter two papers[50,77] provide the only estimates of the threshold energies of SW transformations in pristine graphene, and while one of these and the former paper[50,88] detailed the investigation into the angles at which energy must be transferred from the beam to trigger the transformations, no theoretical estimation of the cross-sections have yet been made. It is easy to understand why - in addition to the strongly anisotropic threshold energy required for the bond rotation to take place, each direction of momentum transfer will also have at least one **upper** threshold energy, above which the SW rotation will not occur and in the extreme case atom emission takes place.

Table 4.2: Activation energies E_a^{SW} for the formation and healing of the SW defect in graphene, including reactions catalysed by adatoms. # atoms indicates the number of atoms used in the computational supercell.

Ref.	**System**	**# atoms**	**Method**	$\mathbf{E_a^{SW}}$ **(eV)**
Formation				
107	PBC		DFT	9.91
108	PBC		DFT-PBE	10.4
109	PBC	50	DFT-PW91	9.2
109			DFT-LDA	9.4
110	PBC		DFT-LDA	9.9
111	PBC	128	DFT-LDA/DZ	11.0, 10.3
112	PBC	48	DFT-PBE	9.3
113	Flake $C_{248}H_{42}$		DFT-PBE/3-21G	10.0
104	Flake $C_{62}H_{20}$		DFT-LDA	9.0
Catalysed:				
104	Flake $C_{62}H_{20}$		DFT-LDA	2.3
Healing				
105	Flake, $C_{42}H_{16}$		DFT -B3LYP/6-31G(d)	6.2
104	Flake $C_{62}H_{20}$		DFT-LDA	5.6
114	PBC	160	DFTB	3.92
Catalysed:				
111	PBC	128	DFT-LDA/DZ	3.9
104	Flake $C_{62}H_{20}$		DFT-LDA	0.7
105	Flake, $C_{42}H_{16}$		DFT -B3LYP/6-31G(d)	0.87

In principle it should be possible to extract the cross-sections from the statistical treatment of experimental observations in TEM. Estimations of the cross-sections in this manner are however hampered by the easy reversibility of the defect formation; it is not sufficient to simply count the number of SW defects that have formed as a function of electron dose, as was the case with atom emission.[52] At the first approximation, this could be achieved by keeping track of the number of defects formed, irrespective of their subsequent healing, however complications soon arise when considering that due to the reversibility, some of the SW defects that form can heal so quickly that they contribute little contrast to the TEM image, and are thus invisible to TEM. Indeed, this is likely to be the case, as the lifetime of SW defects in TEM is comparable to the electron dose per image used (10^7 e^-/nm^2).[88] For all we know then, TEM observations could be missing the majority of SW defects formed, and so a cross-section calculated without taking this into consideration would be useless! An additional complication lies in the theoretically proposed catalytic routes to thermal defect formation and healing. Although the formation of defects has far too large a barrier to be thermally feasible at room temperature even when considering catalysis, the catalytic barriers to healing put this mechanism exactly on the edge of relevance, as discussed. Any attempt to derive a cross-section from experiment must therefore also be sure to to separate thermal and irradiation induced healing processes.

In the next sections, these cross-sections will be obtained from the statistics of a large number of defects forming and healing, using principles of chemical kinetics, and explicitly accounting for both thermally and beam induced processes for both forward (formation) and reverse (healing) reactions. Before that, it is important to briefly mention several recent studies published during the course of this work that have also employed kinetic principles to study reactions under the e-beam, and discuss the key ways in which the current work differs. The formation of divacancies in bilayer graphene at low accelerating voltages was shown to be due to a catalytic effect, by considering the relative concentrations of different species and the rate constants for conversion between them.[78] In addition to the lack of thermal processes, an analysis based on equilibrium concentrations is poorly suited to the SW defect. As discussed below, the concentration of SW defects is extremely low in typical conditions, and basing the analysis on this results in very large errors compared to the approach used here. The migration of a silicon dopant atom[116] in graphene was analysed kinetically by treating the migration events as a Poisson process. By measuring the dose required for each event, the cross-section could be calculated. In a similar fashion, the migration of a divacancy[13] was studied *via* the statistical treatment of the distribution of jump distances observed by 60 kV STEM. In both of these cases, although they are very conceptually similar to the current work, there is a large practical difference between the migrations of a single defect and the net behaviour of many defects forming and healing; the statistics of the latter can not be considered as a Poisson process. And again, the questions of thermal processes and invisibility due to quick reversibility do not apply in these examples.

4.3.2 Kinetics of reversible beam induced processes

In the framework of chemical kinetics the rate of a unimolecular reaction, in which species A simply rearranges itself to produce one or more products, is generally given as

$$-\frac{d[A]}{dt} = k[A] \tag{4.1}$$

where k is the reaction rate constant. For a thermally induced reaction, the temperature dependence of the thermal reaction rate constant k^t is often given by the Arrhenius equation

$$k^t = P \exp\left(\frac{-E_a}{k_B T}\right) \tag{4.2}$$

P is the frequency factor (the rate of particle collisions in gas or liquid, or the rate of bond vibrations in a solid), while the exponent is the probability factor or the success rate of the considered process, namely the proportion of particles at temperature T with a greater energy than the activation energy E_a. The rate of an equivalent irradiation induced reaction can be expressed as

$$-\frac{d[A]}{dt} = j\sigma[A] \tag{4.3}$$

j is the irradiation flux (in $\mathrm{nm}^{-2}\ \mathrm{s}^{-1}$) and σ is the reaction cross-section, with a dimension of area. The macroscopic rate constant of the irradiation induced reaction k^i can be defined as

$$k^i = j\sigma \tag{4.4}$$

In relation to the Arrhenius equation 4.2, for an irradiation induced reaction the frequency factor is now expressed as the irradiation flux j, while the probability factor is simply the reaction cross-section σ. If the energy for the reaction is provided directly *via* an elastic collision, as is now generally assumed,[16,50,52,78,88,93] theoretical estimation of the collision cross-section is provided by the McKinley-Feshbach approximation as detailed in Section 2.1. It should be stressed however that the kinetic analysis in this section makes no assumptions regarding the mechanism of the beam induced reaction (or, indeed, of the nature of the beam) and so the cross-sections measured using this approach are similarly independent of any particular mechanism. Mechanistic insight can be obtained by comparing these cross-sections to theoretically calculated ones corresponding to a particular process, as shown later.

The direct relationship between the macroscopically defined reaction rate constant and the atomistic value of the reaction cross-section, shown in Equation 4.4, in principle allows for experimental techniques traditionally used to obtain one to be used to acquire the other. Many decades of progress in physical chemistry can be exploited to guide the transition of reaction kinetics techniques into the emerging field of nanoscience, in which the concept of cross-sections of key

processes is essential for understanding nanostructure transformations under external influences. The ability to observe single atoms taking part in a reaction potentially allows the calculation of reaction rate constants directly, in a bottom-up approach. Chemical kinetics studies based on the direct observation of atom rearrangements can provide invaluable insight into the elementary reaction steps and routes, which are inaccessible to macroscopic chemical methods. This concept is particularly well suited for studying the formation and transformations of atomic-scale defects in monolayer graphene.

As discussed, for irreversible e-beam induced processes such as atom ejection, the reaction rate constant of defect formation can be obtained simply from the accumulation of the product with time, directly from Equation 4.3. The reaction rate of a reversible reaction, e.g. the formation and healing of defect species D under the e-beam, is determined by the rate of both defect formation and defect healing, denoted by subscripts f and h

$$\frac{d[D]}{dt} = k_f([C]_0 - [D]) - k_h[D] \tag{4.5}$$

$[C]_0$ is the density of atoms in the pristine sample, which in the case of graphene is 32.8 nm^{-2}. Classical chemical kinetics observes the macroscopic outcome of both reactions, i.e. the change in the concentration of species D, while TEM enables the direct observation of each reaction individually. Equation 4.5 can be split into two independent equations, similar to 4.3, the left side of which denote the number of formation events n_f or healing events n_h, per unit time per unit area, rather than the change in concentration:

$$\frac{n_f}{\Delta t} = k_f^i([C]_0 - [D]) = j\sigma_f([C]_0 - [D]) \tag{4.6}$$

$$\frac{n_h}{\Delta t} = k_h^i[D] = j\sigma_h[D] \tag{4.7}$$

As the healing rate depends on the defect concentration $[D]$, which is very low and difficult to measure exactly, it is convenient to consider the healing of defects on an individual basis using the finite difference form of Equation 4.7 setting $[D]$ and n_h to 1 nm^{-2}.

$$\frac{1}{<\Delta t>} = k_h^i = j\sigma_h \tag{4.8}$$

Equation 4.8 reformulates the problem in terms of the average lifetime Δt of a single defect, rather than the aggregate reaction rate, thus removing the dependence on the defect concentration and allowing for the direct measurement of the healing rate from the experimental image series. The average lifedose (the dose of electrons required to heal the defect) is related to the average lifetime as

$$<X>=<\Delta t> j = \frac{1}{\sigma_h} \tag{4.9}$$

Note from Equation 4.9 that for an irradiation induced first order reaction the lifedose does not depend on the electron flux, which is important in the discussion of the results.

As discussed, in the case of reversible processes there is an additional complication related to the fact that the lifetime of a defect can be very short, so that its creation and subsequent elimination passes unnoticed by the image recording system. The inaccessibility of the short-lived defects leads to an overestimation of the average lifedose and consequently to an underestimation of the healing cross-section, σ_h, derived from Equation 4.9. A solution to this problem can be found if we note that the actual value of the lifedose is statistically distributed due to the stochastic nature of the process. Consider the process of electrons arriving on the sample as the statistical process of tossing a biased coin, for which the probability of obtaining heads for a single toss of the coin (the reaction occurring from an individual electron arriving on the sample) is σ_h.[iv] We are looking for the probability that heads will first occur after exactly X throws - this is physically equivalent to the reaction with cross-section σ_h happening after the deposition of exactly an electron dose of X. This probability distribution of the lifedose X is described by the geometric distribution (note that σ_h and X are dimensionless here[v]):

$$Q(X) = \frac{n_h(X)}{N} = (1 - \sigma_h)^{X-1}\sigma_h \tag{4.10}$$

where $n_h(X)$ is the experimentally observed number of healing events that have happened after deposition of dose X, and N is a total number of created defects including invisible short-lived ones. Although the lower part of this distribution is missed due to the limited temporal resolution, it can still be fitted to experimental data, with σ_h and N as free parameters. This provides an unbiased measure of σ_h independent of the one obtained from Equation 4.9. At the same time an unbiased value for σ_f accounting for the short-lived defects can be calculated using N and Equation 4.6. The practical considerations of accomplishing this will be discussed alongside the experimental results in Section 4.3.3.

While the above procedure corresponds to fitting the measured distribution of defect lifedoses to the probability mass function of the geometric distribution - the probability of a defect healing after **exactly** an electron dose of X - an alternative and perhaps more immediately intuitive procedure would be to fit the cumulative distribution function - the probability of a defect healing from **any** of the electrons in dose X. In this latter case, the the right hand side of Equation 4.10 would simply be equal to $(1-\sigma_h)^X$, but this approach has two slight disadvantages to the one used: 1) it doesn't illustrate the problem of invisible defects as well as shown in Figure 4.12 (this would manifest as a flattening of the distribution at low X rather than the distribution falling to zero at low X), and related to this 2) it would be less clear which of the bins shown in this figure (discussed later) to include in the fitting. Using the probability mass function, the bin in which defects become undetectable has a lower value (number of defects) than the adjacent bin

[iv] Alternatively, consider rolling a dice with $1/\sigma_h$ faces.

[v] While the cross-section σ has a dimension of area and dose X has a dimension of reciprocal area, what is actually assumed for σ and X here is $\sigma[\mathrm{nm}^2]/1\ \mathrm{nm}^2$ - the probability of the event for the dose of 1 electron per nm^2 - and $X[\mathrm{e}^-/\mathrm{nm}^2]$*1 nm^2 - the number of electrons landing in 1 nm^2 at the dose X.

at higher dose. In the method using the cumulative distribution function this bin has a smaller value than it should have, but one that is still larger than the adjacent bin at higher dose; in other words, it would be less obvious where the 'visible tail' of defects begins.

4.3.3 Experimental results

This section begins with an examination of SW defect formation, experimentally quantifying the rates of thermally and irradiation induced pathways, and then accounting for short-lived defects. This is followed by a similar treatment for the process of SW defect healing. These results are summarised in tables 4.3 and 4.4, with comparisons to theoretical expectations in the next section.

SW formation

SW defect transformations were induced and imaged using TEM, in areas of pristine graphene 100-200 nm^2 in size. Fourteen series of images at 60 kV and nine series of images at 80 kV were recorded at a variety of electron fluxes ranging from 6.8×10^5 to 2.1×10^7 $e^-/nm^2/s$. TEM images were recorded continuously at 10 frames per second, and over 10,000 frames were analysed. In each image series lasting 20-50 seconds, zero to twenty-four SW defects were observed, typically lasting from 0.1 to 1 s. In total, 114 SW defects were detected at 60 kV, and 68 SW defects were detected at 80 kV. In order to enhance SW defect visibility, the initial image series were Fourier filtered, removing graphene lattice reflections with a spot mask. This resulted in SW defects displaying a characteristic dumbbell pattern on a random background, distinguishable from other local and point defects; it is worth noting that SW defects comprised the vast majority of defects created on the otherwise pristine graphene, attributable to the low accelerating voltages used. The atomic structure of the discovered SW defects and their lifetimes were verified using the unfiltered images. Figure 4.10 shows a typical example of a single defect forming and subsequently healing

The cross-section of SW formation, σ_f, can be estimated from Equation 4.6 in two independent ways: in the integral form as a total number of observed formation events per total area per total dose, and as the slope of a linear plot showing the SW formation rate as a function of electron flux in Figure 4.11. The concentration of SW defects $[D]$ is assumed to be negligible compared to the area density of carbon atoms in graphene $[C]_0 = 38.2$ nm^{-2}. These two estimations give the respective values for σ_f of (0.059 ± 0.006) and (0.067 ± 0.017) barn at 60 kV, and (0.066 ± 0.008) and (0.060 ± 0.008) barn at 80 kV, with the uncertainties being the standard errors obtained from the fitting. It is important to note that, within the error bars, the values for σ_f obtained by two independent methods are intrinsically the same. As short-lived SW defects were not captured by TEM, these cross-sections can only be considered as reliable estimates for the lower limit.

An excellent agreement between the values measured by the integral approach and as a coefficient of linear regression not only demonstrates the consistency of the obtained data and interpretation, but also indicates that there is no significant

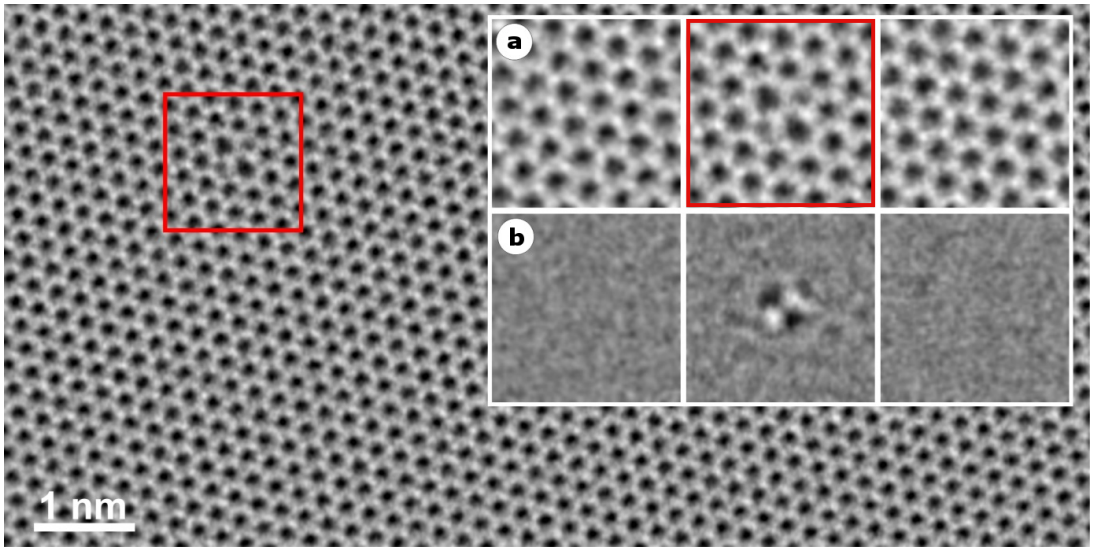


Figure 4.10: Example image of a SW defect in pristine graphene from an image series at 80 kV. Inset shows the area bordered in red: (a) example sequence of a SW defect forming and then healing to return to pristine graphene over 3 seconds (1 second per image); (b) the same images with the graphene lattice removed by Fourier filtering, showing the characteristic dumbbell signal of a SW defect.

contribution from non-irradiative, i.e. thermal, reaction pathways. In particular, this is evident from the y-intercept of fitted straight lines in Figure 4.11 being statistically consistent with zero for both beam energies. In the presence of a thermal pathway and assuming $[D] \ll [C]_0$ Equation 4.6 becomes

$$\frac{n_f}{\Delta t} = (j\sigma_f + k_f^t)[C]_0 \tag{4.11}$$

where k_f^t is the thermal reaction rate constant of SW formation. Assuming that the thermally induced formation rate does not depend on the e-beam energy, from the two intercepts the average estimate of $k_f^t = (0.3{\times}10^{-6} \pm 1.1{\times}10^{-5})$ s^{-1}. Taking the upper limit for k_f^t defined by the error bar as $1.41{\times}10^{-5}$ s^{-1}, assuming the frequency pre-factor P in Equation 4.2 of the order of 10^{12} s^{-1} (computed for the SW defect in graphene[106]) and the temperature of the sample as 300 K, a lower estimate for the activation energy of thermally induced formation of SW defects is $E_f = 1.0$ eV (or 23 kcal/mol).

In order to account for short-lived and thus undetected defects, the lifedose of each of the 182 observed SW defects was measured, and their distribution fitted to the geometric distribution 4.10 as shown in Figure 4.12. The relative probabilities of a SW defect having a lifedose X in the tail end of the distribution were taken from the absolute numbers of SW defects surviving that lifedose in the images. The lifedose data were binned in the smallest intervals large enough to produce a smooth curve, given that SW lifedoses were only known as multiples of the dose per image for each series. The 60 kV lifedose data were binned in intervals of

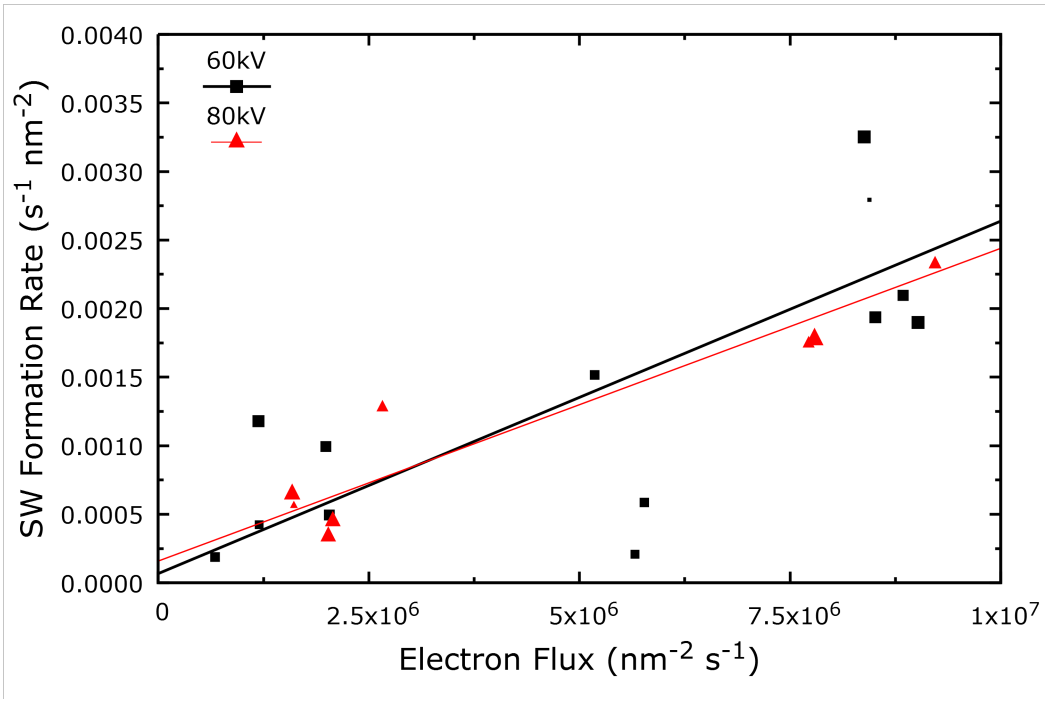


Figure 4.11: The formation rate of SW defects as a function of electron flux at 60 kV (black squares) and 80 kV (red triangles). Weighted least-square regressions are given by the black and thin red lines respectively. The size of each point is proportional to the product of the area and time for corresponding image series, which was used for the weighting of the fitting. Values of the intercept with the y-axis were calculated to be $(6.73\times10^{-5} \pm 3.94\times10^{-4})$ s^{-1} nm^{-2} for 60 kV and $(1.59\times10^{-4} \pm 1.60\times10^{-4})$ s^{-1} nm^{-2} for 80 kV, in both cases therefore statistically consistent with zero.

10^6 e^-/nm^2 while the 80 kV data were binned in intervals of 1.5×10^6 e^-/nm^2.[vi] The lowest bins, in which the probabilities started to decrease due to the lifedose being small enough that SW defects could no longer be reliably detected, were not included in the fitting (these can be seen in Figure 4.12). The tail end of the distribution was fitted iteratively to the geometric distribution, with a free pre-factor A to account for the scaling factor between the number of events and the probability:

$$Q(X) = A(1-\sigma_h)^{X-1}\sigma_h \tag{4.12}$$

Fitting using the Nelder-Mead Simplex algorithm with tolerance = 0.0001 resulted in a σ_h of (5238 ± 308) barn and (5030 ± 340) barn at 60 kV and 80 kV, with R^2 values of 0.99 and 0.98 respectively. The physical meaning (or lack thereof) of these numbers will be discussed in more detail shortly, for now they are simply used to calculate the total number of SW defects that formed (both visible and invisible to TEM). These geometric distributions were summed in the range of the long-lived visible 'tails', and from one to infinity electrons per nm^2, for each accelerating voltage. This gave the proportion of SW defects observed in each case compared to the total number expected to form given the shape of the distribution: 0.42 at 60 kV and 0.32 at 80 kV, corresponding to the formation of 186 and 169 SW defects respectively. The beam induced formation cross-section for each series can be calculated directly using Equation 4.6, resulting in corrected formation cross-sections of (0.0964 ± 0.0038) barn at 60 kV and (0.1644 ± 0.0126) barn at 80 kV with the standard errors associated with the geometric distribution fitting.

SW healing

Estimation of the thermal contribution in the case of healing with a method similar to that used for formation is problematic, as the healing rate is difficult to measure in terms of concentration; as discussed, $[D]$ is very low. The lifetime formalism is a more applicable alternative approach. In the presence of a thermally induced co-reaction, Equation 4.8 becomes

$$\frac{1}{<\Delta t>} = j\sigma_h + k_h^t \tag{4.13}$$

where k_h^t is the rate constant for thermally induced healing of SW defect. Plotting the data in $(\frac{1}{<\Delta t>}, j)$ coordinates (Figure 4.13), σ_h can be obtained as a slope of the best fit, and k_h^t as the y-intercept. The y-intercepts of the straight lines shown in Figure 4.13 are non-zero for both 60 and 80 kV, but could be equal within the error bars. The average value for k_h^t is estimated as (0.56 ± 0.53) s^{-1}. Making the same assumptions as for the SW formation process, the activation

[vi] Effectively, the lifedose data is already binned as it is acquired, as the maximum resolution of the lifedose data is the electron dose of each 0.1 second image. Introducing a mismatch between the binning in the data acquisition and the binning used here would therefore reduce the quality of the fitting, by introducing artefacts such as alternating bins in which there is and isn't any lifedose data.

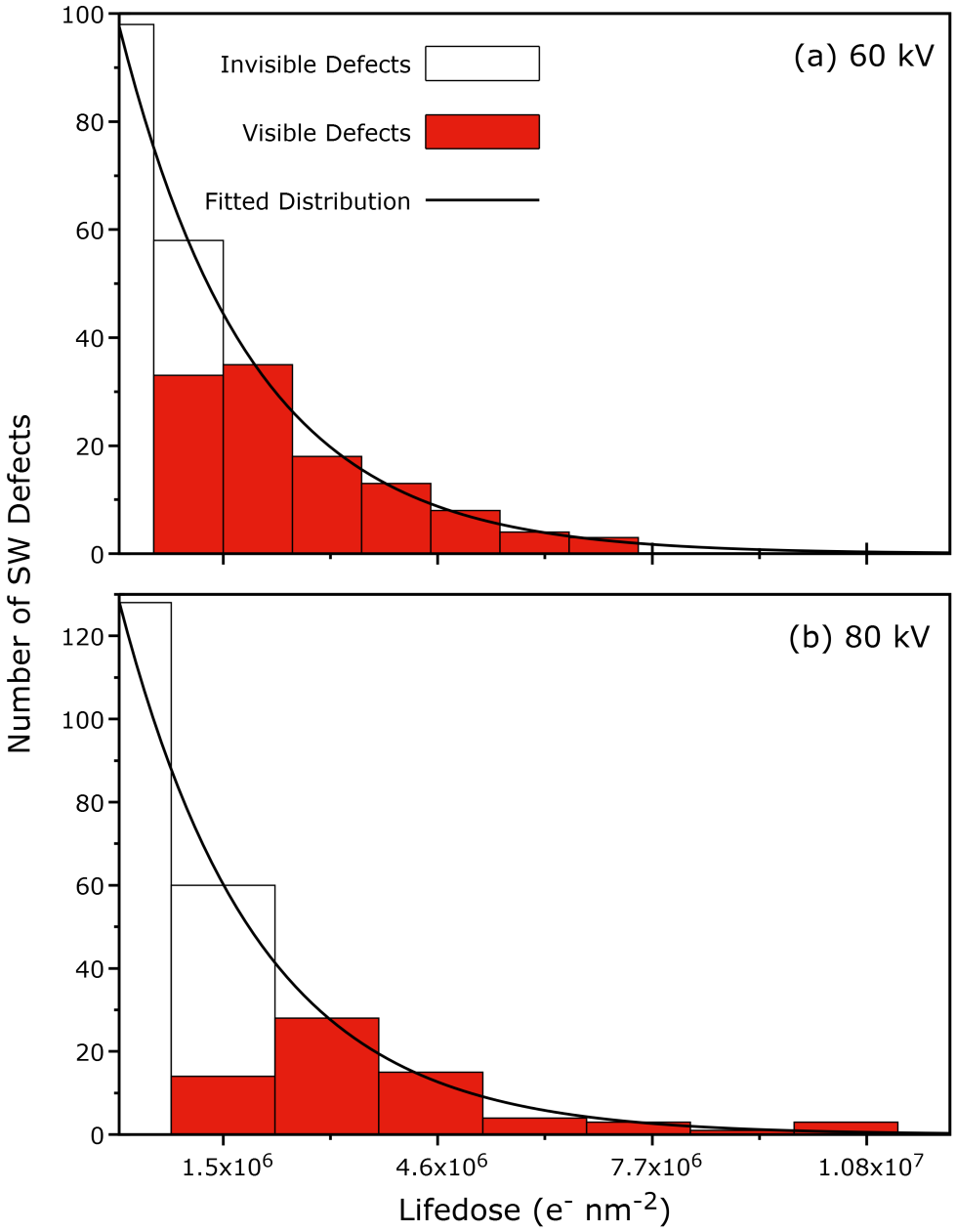


Figure 4.12: The number of SW defects healing with a lifedose falling in each bin (red bars) and the geometric distribution (Equation 4.10) fitted to the experimental data at (a) 60 kV and (b) 80 kV (black lines). The white bars at lower doses show the projected number of undetected SW defects obtained from the geometric distribution.

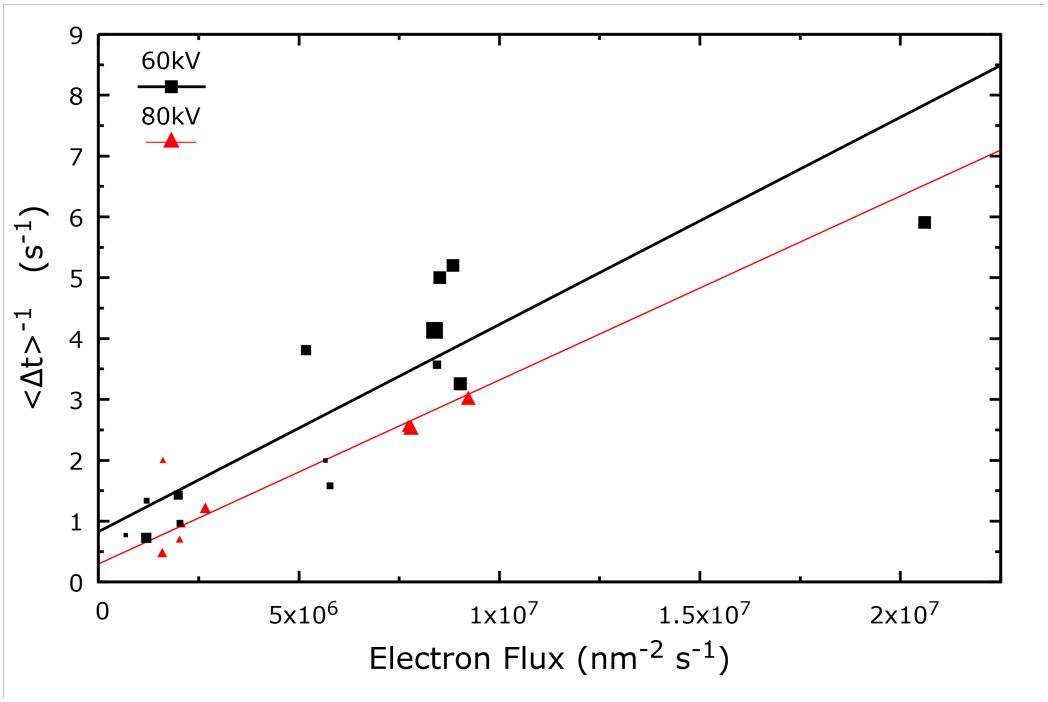


Figure 4.13: Inverse of the average healing time as a function of electron flux for each series of images at 60 kV (black squares) and 80 kV (red triangles). The weighted linear regression of the experimental data is shown by the black and thin red lines, respectively. The size of each point is proportional to the number of SW defects, used for the weighting of the fitting. The obtained slopes are 60 kV: $(3.4\times10^{-7} \pm 0.5\times10^{-7})$ nm^2 (3400 barn) and 80 kV: $(3.0\times10^{-7} \pm 0.2\times10^{-7})$ nm^2 (3000 barn), and the intercepts are 60 kV: (0.83 $\pm$ 0.51) s^{-1} and 80 kV (0.30 $\pm$ 0.13) s^{-1}.

energy for thermally induced healing is $E_h = 0.73^{+0.07}_{-0.02}$ eV (or $16.8^{+1.7}_{-0.4}$ kcal/mol). The cross-section for the irradiation induced reaction estimated from the slope is (3400 $\pm$ 500) barn at 60 kV and (3000 $\pm$ 200) barn at 80 kV. As in the case of SW formation, these cross-sections should be taken as reliable lower estimates due to the presence of unobserved short-lived defects. Better statistics have the potential for a substantial improvement of the reliability of these values; for this, the number of events required would need to be suitable for fitting distribution 4.10 at each electron flux.

At this point it is worth returning to the statistical fit shown in Figure 4.12, which did not account for the thermal contribution to the healing process. Although thermally induced events should follow the same statistics as irradiation induced ones, the number of thermally activated events should be sampled over the lifetime rather than the lifedose. Although the latter is not a direct function of the former (due to the different fluxes used in different experimental series) they are correlated: at any fixed flux there is a linear relation between the two. This implies that the shape of the distribution will not be dramatically affected and thus the total number of events can be estimated accurately. Of course, the

Table 4.3: Formation and healing cross-sections for the SW defect at 60 and 80 kV. Direct and corrected cross-sections for healing (*) do not take into account existing thermal routes and so cannot be directly interpreted as beam induced reaction cross-sections. The fitted and direct cross-sections do not take into account short-lived SW defects and so can be considered lower limits of the true cross-sections.

	Fitted (barn)	**Direct (barn)**	**Corrected (barn)**
σ_f, 60 kV	0.067 ± 0.017	0.059 ± 0.006	0.096 ± 0.004
σ_f, 80 kV	0.060 ± 0.008	0.066 ± 0.008	0.164 ± 0.013
σ_h, 60 kV	3400 ± 500	4700*	5200*
σ_h, 80 kV	3000 ± 200	3500*	5000*

meaning of σ_h determined from this distribution becomes obsolete; however the total number of defects that existed N remains accurate, as do the values for the formation cross-section, σ_f, derived from it.

Table 4.3 summarises the cross-sections for SW formation (given per atom) and for SW healing (given per defect), obtained *via* the linear fits and directly from Equations 4.6 and 4.7, and the corrected cross-sections accounting for short lived undetected defects. The direct cross-sections assume that the only process taking place is beam induced defect formation or healing, while the fitted cross-sections allow for the possibility of other, thermally induced processes of defect formation and healing. As shown, thermally induced pathways are significant for defect healing, and so the direct and corrected cross-sections have no clear physical meaning. However, they are included for the sake of completeness.

4.3.4 Direct knock-on and thermal spikes

Table 4.4 summarises the obtained values of cross-sections and activation energies in comparison to the theoretical predictions discussed in Section 4.3.1. Only a few values fit well to theoretical expectations: σ_f at 80 kV is slightly below the predicted upper limit; the lower limit of thermal activation energy for formation is indeed lower than any theoretical estimation; the thermal activation energy for healing is much lower than theoretical values for direct healing, however it corresponds very well to the predicted[104,105] adatom catalysed mechanism.[vii] The rest of the results are in striking disagreement to theoretical expectations. If the theoretical estimation for σ_f was correct for 60 kV, not a single SW defect would be observed at this accelerating voltage throughout the duration of all the experimental series, while they appeared at a similar rate as at 80 kV. The observed σ_f exceeds the theoretical value by three orders of magnitude.

Similarly, the experimentally measured cross-sections for healing at both beam energies are dramatically higher than expected. Theoretical values of σ_h (based on a mechanism of direct knock-on damage, with a threshold energy calculated as 13 eV[50]) imply that the lifetime of a SW defect should be of the order of 100 seconds in these conditions, which is very different to what is observed here and

[vii]The close match between theory and experiment suggests that at room temperature there is an effective excess of carbon adatoms on the graphene surface.

Table 4.4: Summary of the measured cross-sections of irradiation induced processes and activation energies of thermally induced processes (in bold), in comparison with theoretical estimations from the literature (in italics), discussed in Section 4.3.1. Cross-sections are given per atom for formation and per defect for healing. Theoretical upper limits for cross-sections[a] were calculated assuming processes of direct knock-on damage, using the McKinley-Feshbach approximation. Isotropic approximations of the threshold energies of 19 and 13 eV[50] for formation and healing provide upper limits of the true anisotropic cross-sections.

		60 kV	80 kV
SW formation	Irradiation induced, σ_f	**0.096** ± 0.004 barn *Upper limit: 0.0006 barn*[a]	**0.164** ± 0.013 barn *Upper limit: 0.302 barn*[a]
	Thermal, E_f	Lower limit: **1.0** eV *9-11 eV, adatom catalysis: 2.3 eV*	
SW healing	Irradiation induced, σ_h	Lower limit: **3400** ± 500 barn *Upper limit: 5.8 barn*[a]	Lower limit: **3000** ± 200 barn *Upper limit: 37.0 barn*[a]
	Thermal, E_h	$\mathbf{0.73}^{+0.07}_{-0.02}$ eV *3.4 - 6.2 eV, adatom catalysis: 0.7 - 0.87 eV*	

in previous studies.[88] Both σ_h values measured for 60 and 80 kV are consistent with a knock-on threshold energy of approximately 0.56 eV, as determined from the McKinley-Feshbach formula. This value is inconsistent in two ways: first, it is significantly (in the statistical sense) smaller than the measured E_h, which is physically impossible as discussed in Section 1; and secondly, if a reaction pathway with $E_h < 0.56$ eV existed, it would result in a characteristic thermal healing time of less than 0.01 seconds, in which case SW defects would be undetectable in these experiments. As the McKinley-Feshbach formula describes direct electron-nucleus collisions, the above contradictions unambiguously rule out, for the considered reactions, such collisions as the only mechanism of energy transfer from electron beam to atomic nuclei in graphene. This also includes any potential catalytic pathways allowing energy supply *via* multiple electron collisions, suggested earlier as an explanation for unexpectedly high reaction rates in bi-layer graphene.[78] If such a catalytic route existed, it would be more efficiently realised thermally rather than under irradiation.

One potential explanation for the high reaction rates could be heating induced by the electron beam. A local increase in the temperature directly caused by the e-beam has been previously investigated, and would be expected to be limited to around 1 K.[18,23] However, there is the possibility that electron collisions with or near the SW defect create very brief but hot 'thermal spikes', elevating the effective non-equilibrium temperature of the defect by a sufficient amount to result in a local increase of the rate of reactions *via* thermal pathways. This is an altogether different effect from the average beam induced temperature increase - any thermal spike would be expected to be quickly dissipated (and the time between subsequent electron impacts will be much longer than the lifetime of a thermal spike), but the increase in temperature immediately following the transfer of energy from the beam could be significant. As the size of such spots is substantially larger than the size of SW defect, the reaction might potentially be activated by electron-to-nucleus collisions in an extended area, thus efficiently increasing the cross-section. As this effect would be dependent on the electron flux j, it would be consistent with the very large apparent healing cross-sections measured.

In order to investigate the extent of this effect, a series of molecular dynamics calculations have been performed. Simulations of graphene were carried out by Dr. Matteo Baldoni using the large-scale atomic/molecular massively parallel simulator (LAMMPS) classical molecular dynamics code[117] and the AIREBO potential.[118] A square model of a graphene sheet was created with an edge length of approximately 100 nm, consisting of roughly 400,000 carbon atoms, with a SW defect in the centre and an 11 Å wide framework of frozen C atoms at the edges. Following equilibration, the initial velocity of the PKA was assigned T_{max} at 80 kV (15.8 eV), and the system was propagated in a NVE ensemble for 50 ps. The same simulations were replicated for both pristine graphene and graphene containing a SW defect. A non-equilibrium temperature was estimated for three different groups of atoms over the course of the simulations, shown in Figure 4.14.

The temperature following an electron impact is shown for pristine graphene and the SW defect, for each of the atom groups, in Figure 4.15. This shows that the energy from the beam is very quickly dissipated (in under 1 ps even for the

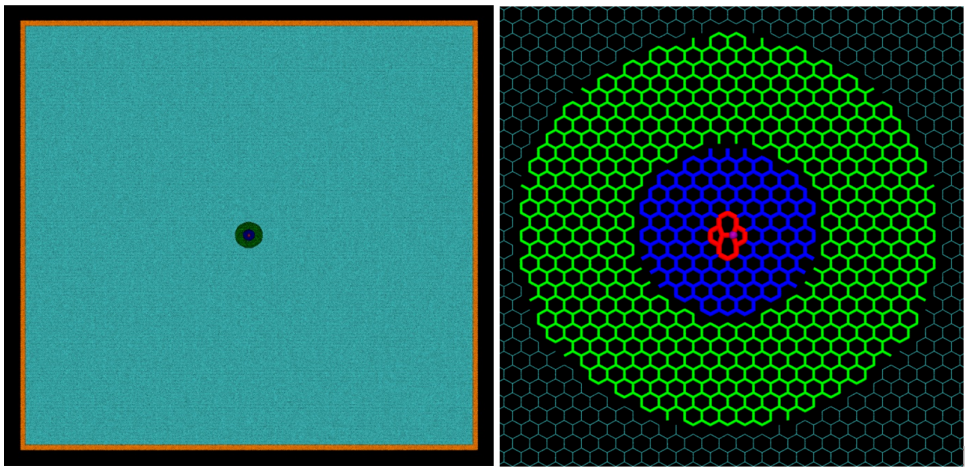


Figure 4.14: Left: the entire simulation cell; right: the central area surrounding the SW defect. The frozen edges are shown in orange. A relatively large group (green, blue and red) includes 1117 atoms arranged in a circle around the PKA (purple). The medium size group (blue and red) includes 211 C atoms, and the smallest group (red) includes only the 16 atoms in the non-hexagonal rings of the SW defect. Produced by Dr. Matteo Baldoni.

largest atom group), and that there are no substantial differences between an impact on pristine graphene and a SW defect.

By taking the Arrhenius equation 4.2, substituting the decay in defect temperature over time for the temperature T, and integrating over the time period for which a thermal spike exists, the effect of the electron impact on the healing reaction rate can be quantified. Only the time from 100 fs after the collision is considered, as the first 100 fs is the characteristic period for direct knock-on damage; during this, the bond rotation will take place or not depending on the specifics of the energy and angles transferred,[50,88] and the concept of temperature has no clear relevance. The activation energy is taken as the measured thermal barrier 0.71 eV, and the probability of one 15.8 eV impact on a SW defect healing it due to the increased temperature in the picosecond before the heat is effectively dissipated is thus calculated as 10^{-4}. A collision transferring at least 15.8 eV to one of the atoms of the SW defect will occur every $\sim$250 seconds at our mean electron flux. Although lower energies will be transferred more often, the resulting decreased elevation in temperature will compensate for this, and so the expected lifetime of a SW defect before healing from this process is therefore approximately 2.5×10^6 seconds. Comparing this to the experimentally observed lifetime of approximately 1 second conclusively eliminates thermal spikes as a possible route for the healing of SW defects. It should also be noted that at 60 kV the maximum transferable energy to a carbon atom is reduced from 15.8 eV to 11.6 eV, and so this effect would be even more minimal - if it was the primary mechanism of beam induced healing, a greater disparity would be seen between the two accelerating voltages.

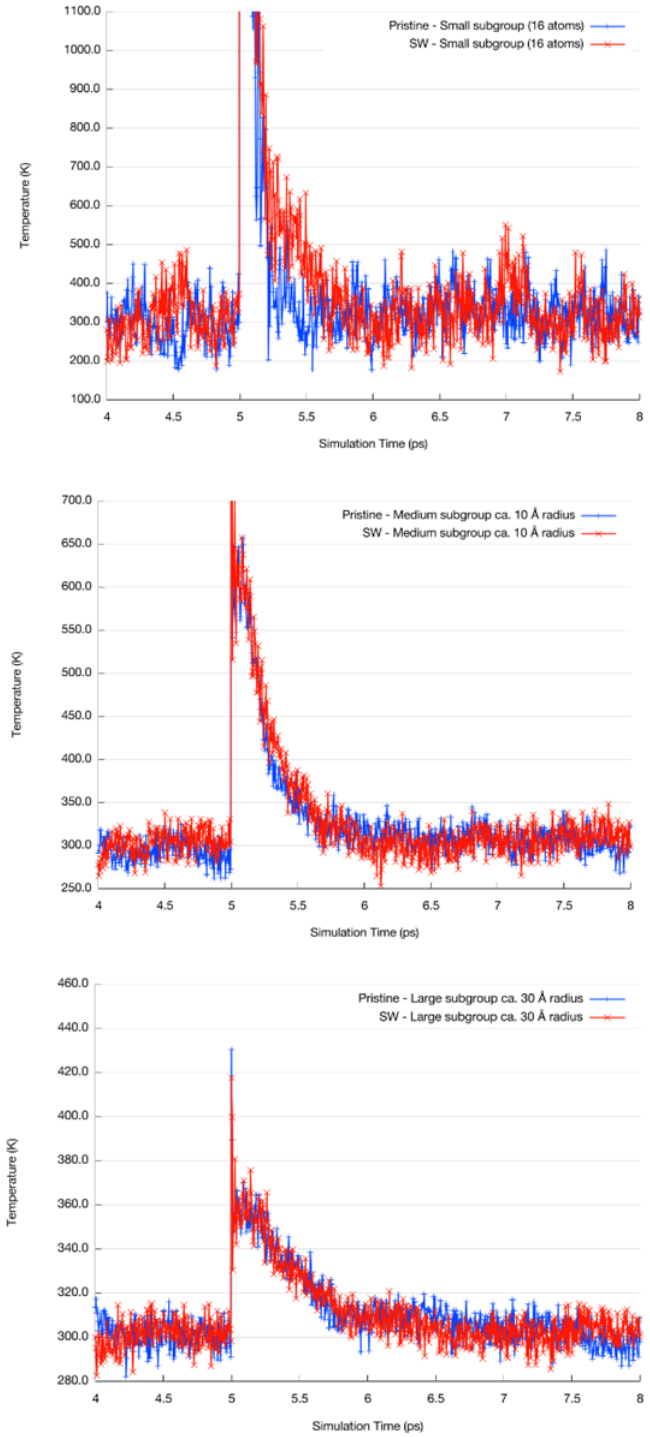


Figure 4.15: The typical temperature increase and subsequent decay following the electron impact, for each group of atoms shown in Figure 4.14. Produced by Dr. Matteo Baldoni.

4.3.5 Inelastic collisions

As electron-nucleus interactions have been eliminated as a possible mechanism leading to quick healing of the SW defect, routes of energy transfer *via* excitation of the electron system of graphene must now be considered. The typical cross-sections for emission of core electrons are of the order of thousands barn (as an example, Egerton[46] estimates the radiolysis cross-section of elemental carbon to be 2100 barn at 100 kV). The high conductivity of graphene precludes ionisation as a mechanism of structural changes - quenching by conduction electrons will occur on a much quicker timescale than bond rotation as discussed in Section 1.2. However, inter and intra band excitations of electrons in graphene have been determined to have anomalously long lifetimes in the order of 10 ps,[119–121] and a conical intersection was shown to provide a nonadiabatic pathway for the SW rotation in a pyrene model, reducing the activation energy when starting from an electronically excited state.[122] The authors of this study speculate that 'there should be nonnegligible effects of electronic excitation and nonadiabatic transitions (NATs) on the reaction mechanism of SWR induced by electron irradiation.'

A theoretical study of the response of the SW defect in graphene to ultrafast laser pulses[123] indicates that relaxation of excited electronic states occurs through the generation of strong localised transversal vibrations at the defect. The amplitude of the vibrations increases until a suitably high proportion of electrons are excited (6%, 1.3 eV absorbed per atom), above which the SW defect will spontaneously heal in only ∼420 fs. In TEM, the electron beam can take the place of the laser pulses, electronically exciting the defect. As the cross-sections of low energy electron excitations by the electron beam in TEM may be exceptionally high (about 2×10^7 barn for 4.5 eV plasmon excitation in monolayer graphene was measured in this experiment) these interactions may result in a sufficient average population of excited states in order to cause spontaneous healing of the SW defect. The healing occurs *via* bond breaking with an out-of-plane motion of the dimer, and consequent dimer rotation.[123] The localisation of coherent transversal phonon modes around lattice imperfections provides a possible explanation for the orders of magnitude faster backward bond rotation (SW healing) as compared to the direct rotation (SW formation). It should be stressed that this is a somewhat speculative proposal, but remains the most likely process considering the definite incompatibility of the experimental results with all other considered possibilities.

4.3.6 Atom emission at 80 kV

The kinetic parameters obtained from this experimental analysis can be used to calculate several useful observable parameters relating to the SW transformation in graphene, namely the expected formation time for a SW defect per unit area t_f, the expected lifetime of a defect Δt, and the equilibrium concentration of SW defects $[D]_{eq}$, all of which will depend on the accelerating voltage and dose rate used. Note that as the cross-sections for irradiation induced healing are lower limits, these average lifetimes and defect concentrations will be upper limits.

The expected lifetime for a SW defect in TEM can be calculated as the inverse

of Equation 4.13, i.e.

$$< \Delta t >= \frac{1}{j\sigma_h + k_h^t} \tag{4.14}$$

The expected time for a SW defect to form in a 100 nm^2 area of graphene under electron irradiation can simply be taken as the inverse of the formation rate given in Equation 4.6, as thermal contributions to this process are negligible. As discussed, the concentration of defects can also be considered negligible, resulting in

$$t_f = \frac{1}{j\sigma_f[C]_0 \times 100 \text{ nm}^2} \tag{4.15}$$

At equilibrium, the rate of formation and healing are the same. Setting these equal to one another and again taking $j\sigma_f \gg k_f^t$ and $[C]_0 \gg [SW]$, the concentration of defects is given by

$$[SW] = [C]_0 \left(\frac{\sigma_f}{\sigma_h} + j\frac{\sigma_f}{k_h^t} \right) \tag{4.16}$$

Using the experimental values found for σ_f, σ_h and k_h^t in this work, these parameters can therefore be estimated for any electron flux at 60 and 80 kV. However, as the equilibrium concentration of defects increases with increasing flux, at very high fluxes the approximation that $[C]_0 \gg [SW]$ will no longer be valid. When $j = 10^9$ e$^-$/nm^2/s, Equation 4.16 predicts a SW concentration $\frac{[SW]}{[C]_0} \approx 0.025$, which can be taken as a good limit for this equation's validity.

In Section 4.1, the observation of atom emission from pristine graphene at 80 kV and very high electron fluxes[91] was briefly discussed. As this is an effect that is 'switched on' at high fluxes but is not seen for low fluxes and high total electron dose, it indicates that the emission is probably the result of cumulative electron impacts: one electron activates a carbon atom or region, and a subsequent electron emits an atom from this region, most likely *via* a direct knock-on collision. There are several proposed explanations for the 'activated region' (plasmon excitation, ionisation, inelastically induced phonon modes), but these are all very short-lived phenomena in graphene and are therefore somewhat unlikely to be responsible, despite the high frequency of such activations relative to direct knock-on impacts. An alternative possibility is that the activated region is an atomic structural change that occurs with comparatively low frequency but has an inherently much longer lifetime: the initial electron induces a SW transformation, and then the second electron emits an atom from the SW defect due to a lowered emission threshold energy in this non-hexagonal, strained, out-of-plane structure. The presence of the thermal pathway for SW healing introduces a flux dependence on the SW equilibrium concentration, causing this effect to only become noticeable at high electron fluxes, while the high flux also means that SW defects would be completely invisible to TEM, thus appearing as though atoms were being emitted from pristine graphene.

The apparent cross-section of the emission was measured as 0.0135 barn.[91] As this was calculated assuming that the emission was from any of the carbon atoms in pristine graphene, this needs to be multiplied by $[C]_0/[SW]$ in order to

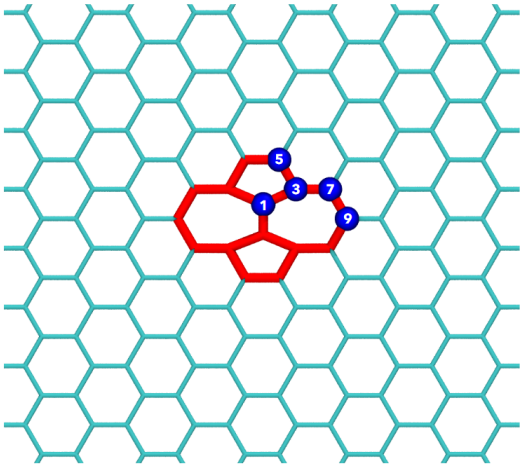


Figure 4.16: The SW defect in graphene, with the inequivalent atoms labelled. Produced by Dr. Matteo Baldoni.

obtain the experimental cross-section for emission from a SW defect, assuming this mechanism is taking place. Using the experimental kinetic parameters, at 80 kV and 10^8 $e^-/nm^2/s$ (the experimental settings at which this was measured[91]), $[SW] \approx 0.1$ nm^{-2}, resulting in an emission cross-section of **5.2 barn/defect**. The reported emission threshold energy from a SW defect is 18 eV.[78] It is unclear which atoms of the defect this is appropriate for, between two (only the central bond) and sixteen (the entire defect). Taking it to be applicable for the six atoms on pentagon/heptagon borders (atoms 1 and 3 in Figure 4.16) and using it to calculate the cross-section *via* Equation 2.11 results in a predicted emission cross-section of **4.8 barn/defect**, which is astonishingly close given the approximations involved in this comparison, suggesting that this is indeed likely to be the mechanism behind the observed low voltage atom emission.

However, a series of DFT-MD simulations calculating the threshold energies for emission from the SW defect (shown in Table 4.5) has shown that these values are much higher than reported, and at 80 kV would correspond to substantially less than 0.1 barn/defect. As the equilibrium concentration used is an upper limit of the true value, this means that there is a minimum of approximately two orders of magnitude between the expected emission rate from SW defects at 10^8 $e^-/nm^2/s$ and the observed omission rate from pristine graphene in these conditions.

It is worth considering possible reasons for the large discrepancy between these calculations and the previously reported result. An original set of simulations resulted in a much closer agreement to the reported value of 18 eV, when the supercell used in the calculation was optimised for pristine graphene. However, the threshold energies greatly increased when the supercell was correctly optimised for the graphene sheet containing the SW defect. Inspection of the MD trajectories showed that in the simulations with the incorrect supercell, unphysical stretches of C-C bonds occurred, and the situation can be considered as loosely corresponding to graphene under strain, which has previously been shown to lower emission

Table 4.5: Emission threshold energies calculated for the SW defect in graphene (±0.5 eV), with atom numbers corresponding to those in Figure 4.16. The PBE exchange correlation functional with the DZP basis set was used on a 680 carbon atom supercell, approximately 42x42 Ångstroms in size. Emission from pristine graphene with this method gave a threshold energy of 23.6 eV, exactly matching the experimental value. Simulations were performed by Dr. Matteo Baldoni.

Atom	**Threshold energy (eV)**	**'Strained graphene'**
1	22.0	17.0
3	>22.5	21.0
5	>23.0	23.0
7	>23.0	23.0
9	>24.0	24.0

threshold energies.[124,125] Alternatively, the difference in the size of the supercell (280 *vs.* 680 used here) may have an effect, as influence of the SW defect has been shown to extend up to 15 Å from the central bond.[106]

Chapter 5

Conclusions

> But then science is nothing but a series of questions that lead to more questions, which is just as well, or it wouldn't be much of a career path, would it?
>
> *The Long Earth*
> *Terry Pratchett & Stephen Baxter*

There is the temptation in TEM studies to believe that you are always seeing the full story - after all, you can watch your material in atomic resolution in real time! What more could you want? Unfortunately, 'in real time' is of course 'in real time, with human temporal resolution' rather than 'in real time, with atomic temporal resolution'; atomic processes occur vastly quicker than the 20^{th} of a second upper resolution of TEM, and can occur quickly enough that they are unseen by it. The 'ghost' structures in Section 4.2 demonstrate one aspect of this: multiple individual atomic configurations that are unstable on the imaging time-scale, thus appearing as a superposition of their dynamic motion. However, this is the case that is easy to account for. Although the exact structure cannot be *directly* inferred from the images, it is at least clear that there is a structure from which to infer! With the SW transformations studied in Section 4.3, the startling conclusion must be made that up to two thirds of the defects produced under the beam heal so quickly that they are completely invisible to the microscope, and that at high electron fluxes only a tiny minority of them will be visible, if any. An area of graphene could be imaged in TEM, and while appearing to be perfectly pristine, this would be disguising a whole roiling mass of atomic structure change. Another well known example of this concerns carbon adatoms. Although known to be on the graphene surface, they cannot be directly observed due to quick migration. Instead their presence must be inferred from their production mechanism, their activity in repairing holes and vacancy defects, and the reduction in the rates of certain processes at high temperature.[115] The measured rate for thermal SW healing also implies that there must be a ready availability of adatoms, excellently matching that of the proposed SW-adatom pair.

These considerations re-emphasise the importance of using theoretical investigations alongside experimental TEM studies. Whether this is similar to the work in Chapter 4.3, using principles of kinetics in order to gain a deeper quantitative understanding of experimental observations, or to that in Chapter 3, using quantum chemistry calculations in order to help explain the mechanisms of observed reactions under the beam, theory can provide a vital check against the assumptions made regarding the underlying processes of experimental observations.

Both of these essentially demonstrate two different approaches at answering the same question - what is the cross-section of the beam-induced reaction we are interested in? The former approach approach makes no assumptions about the underlying process, but requires a large number of high-resolution (spatial and temporal) images of the reaction in order to build up a sufficient statistical spread of data. The latter is purely theoretical, depending on accurate calculations of the threshold energy of the reaction, but is only feasible for certain reactions for which an isotropic approximation of the threshold energy is reasonable.

It is worth considering whether either of these approaches, each used for a very different kind of reaction in very different conditions, would be useful when considering the other system. The kinetics detailed in Section 4.3.2 are general to any process, in any material, and for any kind of beam. All that is assumed is that the reaction is induced by some kind of constant flux. Applying it to the nanotube-encapsulated systems of Chapter 3 introduces some simplifications (the reactions are not thermally driven or reversible), but also many complications (lack of atomic resolution imaging, steric factors govern when molecules can react, how do you define exactly when a molecule or stack has 'reacted' or is 'destroyed'?). These complications introduce necessary 'fudge factors' or empirical parameters. For example in the reactions of PCC, the molecules are only seen reacting at or near the edges of stacks, and so the number of molecules at an edge position is introduced as a parameter, which changes from image to image. Likewise with the density of molecules - this is not constant over the image series. Although difficult, progress can be made in this direction, and a comparison of the cross-sections estimated in this fashion to the fully characterised theoretical knock-on values will answer important questions, such as the degree to which the nanotube successfully protects encapsulated species from inelastic damage under the beam.

Going the other way, the computation of the cross-section for the SW transformation would require a very careful mapping of the anisotropy of the threshold energy; to put the computational effort this would require in perspective, 27,000 dynamical DFTB-MD simulations were required to investigate even a subset of the possible angle and energy space involved.[88] Fully mapping the anisotropy of the threshold energy (or energies) in order to predict a cross-section would take far more effort, and the results of the kinetic analysis suggest that this would have been of little use anyway. Although direct knock-on damage can undoubtedly form and heal SW defects in TEM, it is clearly not the main driving force behind these reactions, and thus fully and accurately characterising the cross-sections of this mechanism would not provide full quantitative understanding of the process. This also highlights the essential importance of using experimental TEM studies as a **quantitative** tool in addition to the qualitative tool it tends to be used as when

studying these kinds of reactions; assumptions that are eminently reasonable (or obvious, even) can turn out to be false, and we can not simply rely on theory to provide the cross-sections for reactions based on them.

At its heart, chemistry is the study of the movement of electrons; their movement to form more electronically stable structures drives chemical reactions and results in the formation of new chemicals. For the beam-induced reactions considered in this thesis, this is not the case. The direct transfer of large kinetic energies to atomic nuclei results in a primarily nucleus-driven chemistry. The nuclei themselves are pushed and prodded into position, and the electrons have to make do with whatever stable structures they can find along the way. The end products must adhere to core principles of chemistry (kinetic stability and so on), but the driving force is fundamentally the movement of nuclei, not electrons, and this opens up a wealth of interesting possibilities, allowing for reaction steps that would be infeasible using traditional chemical means.

The elementally specific nature of the transfer of energy allows for a useful degree of selectivity, while careful tuning of experimental TEM parameters (such as accelerating voltage and flux), informed by theory, can be used to induce certain reaction steps over others in order to achieve specific targeted structures. In order to accomplish this, the underlying reaction mechanisms must be well understood, but the slow nature of elastic collision driven reactions can also provide incredibly useful information in this regard. The long lifetimes of stable intermediate structures in beam driven reactions can allow the exact determination of difficult to predict reaction mechanisms, because of course the original purpose of TEM is still providing its benefit, at higher spatial and temporal resolutions than ever before: atomic resolution imaging of the reacting species, in real time and space.

Historically, beam-induced reactions of specimens in TEM have been considered unwanted 'damage', as is apt when using TEM simply as a tool to characterise materials; the aim then is to minimise the effect of the electron beam so as to obtain an idea of how the specimen exists or behaves in normal conditions without it. However, embracing the unique aspects of this damage in order to achieve otherwise difficult or impossible chemistry has the potential to be incredibly fruitful, enabling a chemistry that is in some ways highly brute force (the transferred energy can be huge, leading predominantly to radical chemistry) but in others inherently very selective (the dependence on element and beam direction, and control over the beam energy and flux). Taken together, they undoubtedly make it a chemistry with an exciting future ahead of it.

Bibliography

[1] K. S. Novoselov, A. K. Geim, S. V. Morozov, D. Jiang, Y. Zhang, S. V. Dubonos, I. V. Grigorieva and A. A. Firsov, *Science*, 2004, **306**, 666–669.

[2] D. Cohen-Tanugi and J. C. Grossman, *Nano Lett.*, 2012, **12**, 3602–3608.

[3] Y. M. Lin, A. Valdes-Garcia, S. J. Han, D. B. Farmer, I. Meric, Y. Sun, Y. Wu, C. Dimitrakopoulos, A. Grill, P. Avouris and K. A. Jenkins, *Science*, 2011, **332**, 1294–1297.

[4] H. Y. Mao, S. Laurent, W. Chen, O. Akhavan, M. Imani, A. A. Ashkarran and M. Mahmoudi, *Chem. Rev.*, 2013, **113**, 3407–3424.

[5] H. Kroto, J. R. Heath, S. C. O'Brien, C. R. F. and R. E. Smalley, *Nature*, 1985, **318**, 162–163.

[6] S. Iijima, *Nature*, 1991, **354**, 56–58.

[7] P. Miró, M. Audiffred and T. Heine, *Chem. Soc. Rev.*, 2014, **43**, 6537.

[8] K. S. Novoselov, V. I. Falko, L. Colombo, P. R. Gellert, M. G. Schwab and K. Kim, *Nature*, 2012, **490**, 192–200.

[9] A. W. Robertson and J. H. Warner, *Nanoscale*, 2013, **5**, 4079.

[10] A. Bachmatiuk, J. Zhao, S. M. Gorantla, I. G. G. Martinez, J. Wiedermann, C. Lee, J. Eckert and M. H. Rummeli, *Small*, 2015, **11**, 515–542.

[11] C. Hetherington, *Mater. Today*, 2004, **7**, 50–55.

[12] S. J. Pennycook, M. F. Chisholm, A. R. Lupini, M. Varela, A. Y. Borisevich, M. P. Oxley, W. D. Luo, K. van Benthem, S. H. Oh, D. L. Sales, S. I. Molina, J. Garcia-Barriocanal, C. Leon, J. Santamaria, S. N. Rashkeev and S. T. Pantelides, *Philos. Trans. R. Soc. A Math. Phys. Eng. Sci.*, 2009, **367**, 3709–3733.

[13] J. Kotakoski, C. Mangler and J. C. Meyer, *Nat. Commun.*, 2014, **5**, 3991.

[14] P. Börner, U. Kaiser and O. Lehtinen, *Phys. Rev. B*, 2016, **93**, 134104.

[15] A. W. Robertson, G.-D. Lee, K. He, E. Yoon, A. I. Kirkland and J. H. Warner, *Nano Lett.*, 2014, **14**, 1634–1642.

[16] J. Kotakoski, D. Santos-Cottin and A. V. Krasheninnikov, *ACS Nano*, 2012, **6**, 671–676.

[17] T. Susi, J. Kotakoski, R. Arenal, S. Kurasch, H. Jiang, V. Skakalova, O. Stephan, A. V. Krasheninnikov, E. I. Kauppinen, U. Kaiser and J. C. Meyer, *ACS Nano*, 2012, **6**, 8837–8846.

[18] R. Egerton, P. Li and M. Malac, *Micron*, 2004, **35**, 399–409.

[19] R. Egerton, R. McLeod, F. Wang and M. Malac, *Ultramicroscopy*, 2010, **110**, 991–997.

[20] R. Egerton, *Ultramicroscopy*, 2013, **127**, 100–108.

[21] F. Banhart, *Reports Prog. Phys.*, 1999, **62**, 1181–1221.

[22] A. V. Krasheninnikov and K. Nordlund, *J. Appl. Phys.*, 2010, **107**, 071301.

[23] O. Lehtinen, S. Kurasch, A. Krasheninnikov and U. Kaiser, *Nat. Commun.*, 2013, **4**, 2098.

[24] G. Algara-Siller, S. Kurasch, M. Sedighi, O. Lehtinen and U. Kaiser, *Appl. Phys. Lett.*, 2013, **103**, 203107.

[25] F. Banhart, J. Kotakoski and A. V. Krasheninnikov, *ACS Nano*, 2011, **5**, 26–41.

[26] S. T. Skowron, I. V. Lebedeva, A. M. Popov and E. Bichoutskaia, *Chem. Soc. Rev.*, 2015, **44**, 3143–3176.

[27] F. Banhart, *J. Mater. Sci.*, 2006, **41**, 4505–4511.

[28] A. Zobelli, A. Gloter, C. P. Ewels, G. Seifert and C. Colliex, *Phys. Rev. B*, 2007, **75**, 245402.

[29] F. Banhart, J. X. Li and A. V. Krasheninnikov, *Phys. Rev. B*, 2005, **71**, 241408.

[30] A. V. Krasheninnikov, F. Banhart, J. X. Li, A. S. Foster and R. M. Nieminen, *Phys. Rev. B*, 2005, **72**, 125428.

[31] B. W. Smith and D. E. Luzzi, *Chem. Phys. Lett.*, 2000, **321**, 169–174.

[32] D. A. Britz and A. N. Khlobystov, *Chem. Soc. Rev.*, 2006, **35**, 637.

[33] M. Koshino, T. Tanaka, N. Solin, K. Suenaga, H. Isobe and E. Nakamura, *Science*, 2007, **316**, 853–853.

[34] K. Harano, S. Takenaga, S. Okada, Y. Niimi, N. Yoshikai, H. Isobe, K. Suenaga, H. Kataura, M. Koshino and E. Nakamura, *J. Am. Chem. Soc.*, 2014, **136**, 466–473.

[35] A. Chuvilin, A. N. Khlobystov, D. Obergfell, M. Haluska, S. Yang, S. Roth and U. Kaiser, *Angew. Chemie Int. Ed.*, 2010, **49**, 193–196.

[36] Y. Sakane, K. Mouri and K. Shintani, *AIP Adv.*, 2015, **5**, 117113.

[37] T. W. Chamberlain, J. Biskupek, S. T. Skowron, P. A. Bayliss, E. Bichoutskaia, U. Kaiser and A. N. Khlobystov, *Small*, 2015, **11**, 622–629.

[38] N. F. Mott, *Proc. R. Soc. A Math. Phys. Eng. Sci.*, 1929, **124**, 425–442.

[39] N. F. Mott, *Proc. R. Soc. A Math. Phys. Eng. Sci.*, 1932, **135**, 429–458.

[40] T. Sexl, *Zeitschrift für Phys.*, 1933, **81**, 178.

[41] P. Urban, *Zeitschrift für Phys.*, 1942, **119**, 67.

[42] J. W. Motz, H. Olsen and H. W. Koch, *Rev. Mod. Phys.*, 1964, **36**, 881–928.

[43] R. H. Dalitz, *Proc. R. Soc. A Math. Phys. Eng. Sci.*, 1951, **206**, 509–520.

[44] H. Uberall and T. W. Donnelly, *Phys. Today*, 1972, **25**, 45.

[45] W. A. McKinley and H. Feshbach, *Phys. Rev.*, 1948, **74**, 1759–1763.

[46] R. Egerton, *Microsc. Res. Tech.*, 2012, **75**, 1550–1556.

[47] M. Boschini, C. Consolandi, M. Gervasi, S. Giani, D. Grandi, V. Ivanchenko, P. Nieminem, S. Pensotti, P. Rancoita and M. Tacconi, *Radiat. Phys. Chem.*, 2013, **90**, 39–66.

[48] F. Seitz and J. Koehler, in *Solid State Phys.*, ed. F. Seitz and D. Turnbull, Academic, New York, Vol. 2 edn., 1956, p. 307.

[49] A. Zobelli, V. Ivanovskaya, P. Wagner, I. Suarez-Martinez, A. Yaya and C. P. Ewels, *Phys. status solidi*, 2012, **249**, 276–282.

[50] Z. Wang, Y. Zhou, J. Bang, M. Prange, S. Zhang and F. Gao, *J. Phys. Chem. C*, 2012, **116**, 16070–16079.

[51] J. Kotakoski, C. H. Jin, O. Lehtinen, K. Suenaga and A. V. Krasheninnikov, *Phys. Rev. B*, 2010, **82**, 113404.

[52] J. C. Meyer, F. Eder, S. Kurasch, V. Skakalova, J. Kotakoski, H. J. Park, S. Roth, A. Chuvilin, S. Eyhusen, G. Benner, A. V. Krasheninnikov and U. Kaiser, *Phys. Rev. Lett.*, 2012, **108**, 196102.

[53] J. C. Meyer, F. Eder, S. Kurasch, V. Skakalova, J. Kotakoski, H. J. Park, S. Roth, A. Chuvilin, S. Eyhusen, G. Benner, A. V. Krasheninnikov and U. Kaiser, *Phys. Rev. Lett.*, 2013, **110**, 239902.

[54] Q. Yan, J. Wang, D. Chen, J. Gigax and L. Shao, *Nucl. Instruments Methods Phys. Res. Sect. B Beam Interact. with Mater. Atoms*, 2015, **350**, 20–25.

[55] P. Hohenberg and W. Kohn, *Phys. Rev.*, 1964, **136**, B864–B871.

[56] W. Kohn and L. J. Sham, *Phys. Rev.*, 1965, **140**, A1133–A1138.

[57] D. M. Ceperley and B. J. Alder, *Phys. Rev. Lett.*, 1980, **45**, 566–569.

[58] S. H. Vosko, L. Wilk and M. Nusair, *Can. J. Phys.*, 1980, **58**, 1200–1211.

[59] J. P. Perdew and Y. Wang, *Phys. Rev. B*, 1992, **45**, 13244–13249.

[60] A. D. Becke, *Phys. Rev. A*, 1988, **38**, 3098–3100.

[61] C. Lee, W. Yang and R. G. Parr, *Phys. Rev. B*, 1988, **37**, 785–789.

[62] J. P. Perdew, P. Ziesche and H. Eschrig, *Electronic structure of solids*, Akademie Verlag, Berlin, 1991, pp. 11–20.

[63] J. P. Perdew, *Phys. Rev. B*, 1986, **33**, 8822–8824.

[64] A. D. Becke, *J. Chem. Phys.*, 1993, **98**, 5648.

[65] J. M. Herbert and M. Head-Gordon, *Phys. Chem. Chem. Phys.*, 2005, **7**, 3269.

[66] Y. Shao, Z. Gan, E. Epifanovsky, A. T. Gilbert, M. Wormit, J. Kussmann, A. W. Lange, A. Behn, J. Deng, X. Feng, D. Ghosh, M. Goldey, P. R. Horn, L. D. Jacobson, I. Kaliman, R. Z. Khaliullin, T. Kuś, A. Landau, J. Liu, E. I. Proynov, Y. M. Rhee, R. M. Richard, M. A. Rohrdanz, R. P. Steele, E. J. Sundstrom, H. L. Woodcock, P. M. Zimmerman, D. Zuev, B. Albrecht, E. Alguire, B. Austin, G. J. O. Beran, Y. A. Bernard, E. Berquist, K. Brandhorst, K. B. Bravaya, S. T. Brown, D. Casanova, C.-M. Chang, Y. Chen, S. H. Chien, K. D. Closser, D. L. Crittenden, M. Diedenhofen, R. A. DiStasio, H. Do, A. D. Dutoi, R. G. Edgar, S. Fatehi, L. Fusti-Molnar, A. Ghysels, A. Golubeva-Zadorozhnaya, J. Gomes, M. W. Hanson-Heine, P. H. Harbach, A. W. Hauser, E. G. Hohenstein, Z. C. Holden, T.-C. Jagau, H. Ji, B. Kaduk, K. Khistyaev, J. Kim, J. Kim, R. A. King, P. Klunzinger, D. Kosenkov, T. Kowalczyk, C. M. Krauter, K. U. Lao, A. D. Laurent, K. V. Lawler, S. V. Levchenko, C. Y. Lin, F. Liu, E. Livshits, R. C. Lochan, A. Luenser, P. Manohar, S. F. Manzer, S.-P. Mao, N. Mardirossian, A. V. Marenich, S. A. Maurer, N. J. Mayhall, E. Neuscamman, C. M. Oana, R. Olivares-Amaya, D. P. O'Neill, J. A. Parkhill, T. M. Perrine, R. Peverati, A. Prociuk, D. R. Rehn, E. Rosta, N. J. Russ, S. M. Sharada, S. Sharma, D. W. Small, A. Sodt, T. Stein, D. Stück, Y.-C. Su, A. J. Thom, T. Tsuchimochi, V. Vanovschi, L. Vogt, O. Vydrov, T. Wang, M. A. Watson, J. Wenzel, A. White, C. F. Williams, J. Yang, S. Yeganeh, S. R. Yost, Z.-Q. You, I. Y. Zhang, X. Zhang, Y. Zhao, B. R. Brooks, G. K. Chan, D. M. Chipman, C. J. Cramer, W. A. Goddard, M. S. Gordon, W. J. Hehre, A. Klamt, H. F. Schaefer, M. W. Schmidt, C. D. Sherrill, D. G. Truhlar, A. Warshel, X. Xu, A. Aspuru-Guzik, R. Baer, A. T. Bell, N. A. Besley, J.-D. Chai, A. Dreuw, B. D. Dunietz, T. R. Furlani, S. R. Gwaltney, C.-P. Hsu, Y. Jung, J. Kong,

D. S. Lambrecht, W. Liang, C. Ochsenfeld, V. A. Rassolov, L. V. Slipchenko, J. E. Subotnik, T. Van Voorhis, J. M. Herbert, A. I. Krylov, P. M. Gill and M. Head-Gordon, *Mol. Phys.*, 2015, **113**, 184–215.

[67] K. Fujiwara, *J. Phys. Soc. Japan*, 1961, **16**, 2226–2238.

[68] J. M. Cowley and A. F. Moodie, *Acta Crystallogr.*, 1957, **10**, 609–619.

[69] C. Koch, *Ph.D. thesis*, Arizona State University, 2002.

[70] R. F. Loane, P. Xu and J. Silcox, *Acta Crystallogr. Sect. A Found. Crystallogr.*, 1991, **47**, 267–278.

[71] A. Santana, A. Zobelli, J. Kotakoski, A. Chuvilin and E. Bichoutskaia, *Phys. Rev. B*, 2013, **87**, 094110.

[72] A. Lubk, F. Röder, T. Niermann, C. Gatel, S. Joulie, F. Houdellier, C. Magén and M. J. Hÿtch, *Ultramicroscopy*, 2012, **115**, 78–87.

[73] S. T. Skowron, I. V. Lebedeva, A. M. Popov and E. Bichoutskaia, *Nanoscale*, 2013, **5**, 6677–6692.

[74] A. S. Sinitsa, I. V. Lebedeva, A. A. Knizhnik, A. M. Popov, S. T. Skowron and E. Bichoutskaia, *Dalt. Trans.*, 2014, **43**, 7499.

[75] J. H. Warner, Y. Ito, M. H. Rümmeli, T. Gemming, B. Büchner, H. Shinohara and G. A. D. Briggs, *Phys. Rev. Lett.*, 2009, **102**, 195504.

[76] A. V. Talyzin, I. V. Anoshkin, A. V. Krasheninnikov, R. M. Nieminen, A. G. Nasibulin, H. Jiang and E. I. Kauppinen, *Nano Lett.*, 2011, **11**, 4352–4356.

[77] K. Jin, H. Y. Xiao, Y. Zhang and W. J. Weber, *Appl. Phys. Lett.*, 2014, **104**, 203106.

[78] J. Zubeltzu, A. Chuvilin, F. Corsetti, A. Zurutuza and E. Artacho, *Phys. Rev. B*, 2013, **88**, 245407.

[79] A. Chuvilin, E. Bichoutskaia, M. C. Gimenez-Lopez, T. W. Chamberlain, G. A. Rance, N. Kuganathan, J. Biskupek, U. Kaiser and A. N. Khlobystov, *Nat. Mater.*, 2011, **10**, 687–692.

[80] T. W. Chamberlain, J. Biskupek, G. a. Rance, A. Chuvilin, T. J. Alexander, E. Bichoutskaia, U. Kaiser and A. N. Khlobystov, *ACS Nano*, 2012, **6**, 3943–3953.

[81] S. W. Han, W. S. Yun, J. D. Lee, Y. H. Hwang, J. Baik, H. J. Shin, W. G. Lee, Y. S. Park and K. S. Kim, *Phys. Rev. B*, 2015, **92**, 241303.

[82] B. Botka, M. E. Füstös, H. M. Tóháti, K. Németh, G. Klupp, Z. Szekrényes, D. Kocsis, M. Utczás, E. Székely, T. Váczi, G. Tarczay, R. Hackl, T. W. Chamberlain, A. N. Khlobystov and K. Kamarás, *Small*, 2014, **10**, 1369–1378.

[83] A. I. Chernov, P. V. Fedotov, A. V. Talyzin, I. Suarez Lopez, I. V. Anoshkin, A. G. Nasibulin, E. I. Kauppinen and E. D. Obraztsova, *ACS Nano*, 2013, **7**, 6346–6353.

[84] M. Fujihara, Y. Miyata, R. Kitaura, Y. Nishimura, C. Camacho, S. Irle, Y. Iizumi, T. Okazaki and H. Shinohara, *J. Phys. Chem. C*, 2012, **116**, 15141–15145.

[85] M. Koshino, H. Kurata and S. Isoda, *Ultramicroscopy*, 2010, **110**, 1465–1474.

[86] K. Y. Chernichenko, V. V. Sumerin, R. V. Shpanchenko, E. S. Balenkova and V. G. Nenajdenko, *Angew. Chemie Int. Ed.*, 2006, **45**, 7367–7370.

[87] T. Hensel, N. Andersen, M. Plesner and M. Pittelkow, *Synlett*, 2015, **27**, 498–525.

[88] J. Kotakoski, J. C. Meyer, S. Kurasch, D. Santos-Cottin, U. Kaiser and A. V. Krasheninnikov, *Phys. Rev. B*, 2011, **83**, 245420.

[89] L. Tsetseris, B. Wang and S. T. Pantelides, *Phys. Rev. B*, 2014, **89**, 035411.

[90] A. W. Robertson, B. Montanari, K. He, C. S. Allen, Y. A. Wu, N. M. Harrison, A. I. Kirkland and J. H. Warner, *ACS Nano*, 2013, **7**, 4495–4502.

[91] A. W. Robertson, C. S. Allen, Y. a. Wu, K. He, J. Olivier, J. Neethling, A. I. Kirkland and J. H. Warner, *Nat. Commun.*, 2012, **3**, 1144.

[92] R. Zan, Q. M. Ramasse, U. Bangert and K. S. Novoselov, *Nano Lett.*, 2012, **12**, 3936–3940.

[93] J. Kotakoski, A. V. Krasheninnikov, U. Kaiser and J. C. Meyer, *Phys. Rev. Lett.*, 2011, **106**, 105505.

[94] A. R. Botello-Méndez, X. Declerck, M. Terrones, H. Terrones and J.-C. Charlier, *Nanoscale*, 2011, **3**, 2868.

[95] A. W. Robertson, G.-D. Lee, K. He, E. Yoon, A. I. Kirkland and J. H. Warner, *Nano Lett.*, 2014, **14**, 3972–80.

[96] A. A. Martin, G. McCredie and M. Toth, *Appl. Phys. Lett.*, 2015, **107**, 041603.

[97] A. W. Robertson, G.-D. Lee, K. He, C. Gong, Q. Chen, E. Yoon, A. I. Kirkland and J. H. Warner, *ACS Nano*, 2015, **9**, 11599–11607.

[98] K. Yamashita, M. Saito and T. Oda, *Jpn. J. Appl. Phys.*, 2006, **45**, 6534–6536.

[99] M. Saito, K. Yamashita and T. Oda, *Jpn. J. Appl. Phys.*, 2007, **46**, L1185–L1187.

[100] M. Oubal, S. Picaud, M. T. Rayez and J. C. Rayez, *Comput. Theor. Chem.*, 2012, **990**, 159–166.

[101] Z. Yang, L. Yin, J. Lee, W. Ren, H.-M. Cheng, H. Ye, S. T. Pantelides, S. J. Pennycook and M. F. Chisholm, *Angew. Chemie Int. Ed.*, 2014, **53**, 8908–8912.

[102] D. W. Brenner, O. A. Shenderova, J. A. Harrison, S. J. Stuart, B. Ni and S. B. Sinnott, *J. Phys. Condens. Matter*, 2002, **14**, 783–802.

[103] S. Kurasch, J. Kotakoski, O. Lehtinen, V. Skákalová, J. Smet, C. E. Krill, A. V. Krasheninnikov and U. Kaiser, *Nano Lett.*, 2012, **12**, 3168–3173.

[104] C. Ewels, M. Heggie and P. Briddon, *Chem. Phys. Lett.*, 2002, **351**, 178–182.

[105] C. Wang and Y.-h. Ding, *J. Mater. Chem. A*, 2013, **1**, 1885–1891.

[106] J. Ma, D. Alfè, A. Michaelides and E. Wang, *Phys. Rev. B*, 2009, **80**, 033407.

[107] I. Lebedeva, A. Knizhnik, A. Bagatur'yants and B. Potapkin, *Phys. E Low-dimensional Syst. Nanostructures*, 2008, **40**, 2589–2595.

[108] L. Meng, J. Jiang, J. Wang and F. Ding, *J. Phys. Chem. C*, 2014, **118**, 720–724.

[109] L. Li, S. Reich and J. Robertson, *Phys. Rev. B*, 2005, **72**, 184109.

[110] Q. Zhao, M. B. Nardelli and J. Bernholc, *Phys. Rev. B*, 2002, **65**, 144105.

[111] P. Jensen, J. Gale and X. Blase, *Phys. Rev. B*, 2002, **66**, 193403.

[112] A. J. M. Nascimento and R. W. Nunes, *Nanotechnology*, 2013, **24**, 435707.

[113] T. Dumitrica and B. I. Yakobson, *Appl. Phys. Lett.*, 2004, **84**, 2775.

[114] A. Podlivaev and L. Openov, *Phys. Lett. A*, 2015, **379**, 1757–1761.

[115] K. He, A. W. Robertson, Y. Fan, C. S. Allen, Y.-c. Lin, K. Suenaga, A. I. Kirkland and J. H. Warner, *ACS Nano*, 2015, **9**, 4786–4795.

[116] T. Susi, J. Kotakoski, D. Kepaptsoglou, C. Mangler, T. C. Lovejoy, O. L. Krivanek, R. Zan, U. Bangert, P. Ayala, J. C. Meyer and Q. Ramasse, *Phys. Rev. Lett.*, 2014, **113**, 115501.

[117] S. Plimpton, *J. Comput. Phys.*, 1995, **117**, 1–19.

[118] S. J. Stuart, A. B. Tutein and J. A. Harrison, *J. Chem. Phys.*, 2000, **112**, 6472.

[119] S. Gilbertson, G. L. Dakovski, T. Durakiewicz, J.-X. Zhu, K. M. Dani, A. D. Mohite, A. Dattelbaum and G. Rodriguez, *J. Phys. Chem. Lett.*, 2012, **3**, 64–68.

[120] P. A. George, J. Strait, J. Dawlaty, S. Shivaraman, M. Chandrashekhar, F. Rana and M. G. Spencer, *Nano Lett.*, 2008, **8**, 17–20.

[121] J. H. Strait, H. Wang, S. Shivaraman, V. Shields, M. Spencer and F. Rana, *Nano Lett.*, 2011, **11**, 4902–4906.

[122] K. Yamazaki, N. Niitsu, K. Nakamura, M. Kanno and H. Kono, *J. Phys. Chem. A*, 2012, **116**, 11441–11450.

[123] F. Valencia, A. H. Romero, H. O. Jeschke and M. E. Garcia, *Phys. Rev. B*, 2006, **74**, 075409.

[124] E. Holmström, L. Toikka, a. V. Krasheninnikov and K. Nordlund, *Phys. Rev. B*, 2010, **82**, 045420.

[125] S. Kida, M. Yamamoto, K. Tada, H. Kawata, Y. Hirai and M. Yasuda, *J. Vac. Sci. Technol. A Vacuum, Surfaces, Film.*, 2015, **33**, 05E127.